




FACULTY OF SCIENCE AND TECHNOLOGY

MASTER'S THESIS

Study programme / specialisation: Marine and Offshore Technology	The spring semester, 2023 Open / Confidential
Author: Karan Sandipkumar Patel	 (signature author)
Supervisor at UiS: Professor Yihan Xing Co-supervisor: Ph.D. candidate Yucong Ma	
Thesis title: Bending moment and efficient fatigue assessment in a Subsea Shuttle Tanker under the effect of waves	
Credits (ECTS): 30	
Keywords: Submarine, seakeeping, multi-body dynamics, bending moment, fatigue damage, rainflow counting, stress concentration factor,	Pages: 97 + appendix: 52 Stavanger, 15/06/2023

Abstract

The subsea shuttle tanker (SST) is the next-generation autonomous submarine designed to transport liquid CO₂ from land/offshore facilities to the smaller fields for injection. Unlike normal shuttle tankers, which are highly weather dependent, the SST can carry out freight operations in all weather conditions because it travels underwater between 40 m and 70 m water depth.

The first part of the thesis proposes a fast, efficient and reliable multi-body approach to determine the bending moment response of the SST hull at 40 m and 70 m water depth. The chosen approach is based on the discrete-module-beam bending-based hydroelasticity principle. The flexible hull of the vessel is divided into several multi-body rigid modules. All the hydrodynamic and hydrostatic forces are applied to the center of gravity of each rigid module. The parametric models, like the state-space model system, are used to compute the free-surface memory effect more effectively. The multi-body equation of motion is solved to determine the bending moment response of an interconnected multi-body rigid module. The numerical model is prepared using Matlab Simulink to study the dynamics of the vessel. A convergence study is conducted to select the optimal number of bodies needed to perform this study. The result shows that the lower number of bodies (i.e., three and five bodies) does not have enough points to capture all the wave encounter frequencies, thus underestimating the bending moment. Therefore, seven-body SST is used to carry out a further assessment. The bending moment standard deviation is reduced by approximately 50 % when SST travels at 70 m water depth instead of 40 m.

The second part of the thesis presents the fatigue assessment of the SST hull, considering the stiffeners' local details. Two FE models (2D axisymmetric and 3D shell element models) representing the local detail of the flooded-mid body of the SST are prepared to determine the stress concentration factor (SCF). The resultant SCF can be given using the superposition concept by taking the product of the SCF for the individual models. The Rainflow counting method and Palmgren-Miner rule are used to calculate the accumulated fatigue damage and fatigue life. The numerical results show that the impact of long waves has contributed to the most damage to the vessel. The minimum fatigue life at the flooded-mid section is 13 and 19 years for the 40 m and 70 m water depths, respectively. The results also show that fatigue life due to the change in hydrostatic pressure during dive-in and dive-out is five years.

Acknowledgement

This thesis is the final work that concludes my master's degree in Marine and Offshore Technology at the University of Stavanger. This thesis's success and outcome needed a lot of advice and assistance from many people, and I am incredibly fortunate to have received this throughout my thesis.

First, I would like to admire and thank my supervisor, Professor Yihan Xing, for allowing me to work under his supervision on a wonderful topic. I am incredibly grateful to my supervisor for providing me with all the support, encouragement and inspiring guidance required to complete this thesis successfully. I would also like to thank my co-supervisor, Ph.D. candidate Yucong Ma and Post Doc. Chao Ren for their valuable collaboration, input, discussions, and comments throughout the thesis. I would also like to thank the Department of Mechanical and Structural Engineering and Material Science, University of Stavanger, for providing all the necessary resources throughout the thesis.

I am grateful and lucky to have received continuous encouragement, support and instruction from my entire Marine and Offshore Technology course teaching staff. Also, a very big and heartfelt thank to all my friends: Abhishek Mashruwala, Manan Engineer, Hassan Hasan Yousef, Arash Shahbazi Doust and Dennis Beier for all the discussions and for sharing their knowledge with me during the work. Finally, I would like to thank my mom and my whole family for their blessings and constant support throughout my master's degree.

Stavanger, 15th June 2023,

Karan Sandipkumar Patel

Publications

The following papers were written during the thesis:

Paper – 1

Patel, K. S., Ma, Y., Xing, Y., & Li, L. (2023). Modelling and analysis of the bending moment in a Subsea Shuttle Tanker under the effect of waves using a multi-body approach. Proceeding of the ASME 2023 42 nd International Conference on Ocean, Offshore and Arctic Engineering, Melbourne, Australia.

Paper – 2

Patel, K. S., Ma, Y., & Xing, Y. (2023). Lower bound buckling capacity prediction for the isotropic cylindrical shell under axial compression loading using a probabilistic approach. (Draft)

Table of Contents

Abstract.....	ii
Acknowledgement	iii
Publications.....	iv
List of Abbreviation.....	ix
List of Figures.....	xi
List of Tables	xiii
Chapter 1 – Introduction.....	1
1.1. Motivation and Background.....	1
1.2. Objectives of the thesis	4
1.3. Outline.....	4
Chapter 2 – Literature review and methodology	6
2.1. Previous work.....	6
2.2. Multibody concept.....	8
2.3. Wave theory	9
2.3.1. Linear wave theory	9
2.3.2. Ocean waves	12
2.4. Hydrodynamic forces	16
2.4.1. Excitation force.....	18
2.4.2. Radiation force.....	19
2.5. Preliminaries of fatigue analysis	21
2.5.1. S-N curve approach.....	21
2.5.2. Rain-flow counting method	22
2.5.3. Palmgren-miner rule	23
2.6. Fatigue assessment methods.....	24

2.6.1.	Deterministic method.....	24
2.6.2.	Spectra fatigue damage method.....	25
2.6.3.	Time domain method.....	27
2.6.4.	Fatigue assessment based on fracture mechanics.....	29
Chapter 3 – Approach.....		34
3.1.	Identification of the convolution integral using a parametric model.....	34
3.2.	Properties of the parametric model.....	35
3.2.1.	Low-frequency asymptotic value.....	36
3.2.2.	High-frequency asymptotic value.....	36
3.2.3.	Initial time value.....	36
3.2.4.	Final time value.....	37
3.2.5.	Passivity.....	37
3.3.	Different methods to identify parametric model.....	38
3.3.1.	Frequency-domain identification method.....	39
3.3.2.	FDI Toolbox.....	39
3.4.	Matrix assembly.....	41
Chapter 4 – Subsea Shuttle Tanker (SST) planar model design.....		44
4.1.	Design parameters of the SST.....	44
4.2.	General arrangements.....	45
4.2.1.	Compartments.....	45
4.2.2.	Weights and spaces distribution.....	46
4.3.	Seakeeping model.....	49
4.3.1.	Coordinate system.....	49
4.3.2.	Plant model.....	50
4.3.3.	Actuator model.....	50

4.4.	Simulink implementation	51
4.5.	Control system design – Proportional-Integral-Derivative Controller.....	53
Chapter 5 – Bending moment assessment using the multibody approach.....		55
5.1.	Design load cases	55
5.2.	Case studies	56
5.3.	PID controller tuning.....	57
5.4.	Convergence study	58
5.5.	Time-domain and power spectral density response	62
5.6.	Effect of water depth.....	64
Chapter 6 – Fatigue assessment of the Subsea Shuttle Tanker hull.....		66
6.1.	Fatigue analysis methodology.....	67
6.2.	Overview of local stress calculation.....	67
6.3.	FEA modelling of local detail	68
6.3.1.	Analysis model.....	69
6.3.2.	Material properties	71
6.3.3.	Mesh details	71
6.3.4.	Mesh convergence study.....	72
6.3.5.	Loads and boundary conditions	76
6.3.6.	FE analysis results: SCF.....	76
6.4.	Wave-induced fatigue	79
6.5.	Environmental conditions	81
6.6.	Fatigue assessment results – Hydrodynamics vs Hydrostatic.....	83
6.6.1.	Wave-induced fatigue	83
6.6.2.	Fatigue due to hydrostatic pressure.....	86
Chapter 7 – Conclusion and recommendations for future work.....		87

7.1. Conclusion.....	87
7.2. Recommendations for future work.....	88
References.....	89
Appendix A – The stiffness matrix K_{ij}	98
Appendix B – MATLAB code of frequency-domain identification of radiation model	99
Appendix C – MATLAB code to determine a state-space model to compute free-surface memory effect for seven body SST.....	100
Appendix D – Python code for Rainflow counting method	102
Appendix E – Python code for fatigue calculator	104
Appendix F – Illustration of FAT class with $FAT X$ number (DNV, 2015).....	107
Appendix G – Appended papers	108

List of Abbreviation

ABS – American Bureau of Shipping
AUV – Autonomous Underwater Vehicle
BBC – Bottom Boundary Condition
CCS – Carbon Capture and Storage
CoB – Center of Buoyancy
CoG – Center of Gravity
CP – Cathodic Protection
DBC – Dynamic Boundary Condition
DFF – Design Fatigue Factor
DNV – Det Norske Veritas
DOF – Degree of Freedom
FC – Free Corrosion
FDI – Frequency Domain Identification
FE – Finite element
FFT – Fast Fourier Transformation
FK – Froude Krilov
FPSO – Floating Production Storage and Offloading
FWD – Forward
GHG – Greenhouse Gas
HCF – High Cycle Fatigue
HOBEM – Higher-Order Boundary Element Method
IFFT – Inverse Fast Fourier Transformation
JONSWAP – Joint North Sea Wave Project
KBC – Kinematic Boundary Condition
LC – Load case
LQR – Linear Quadratic Regulator

LS – Least Square

MATLAB – Matrix Laboratory

MSS – Marine System Simulator

MT – Million Tons

NDT – Non-Destructive Testing

OWT – Offshore Wind Turbine

PID – Proportional Integral Derivative

PM – Pierson-Moskowitz

PSD – Power Spectral Density

RAO – Response Amplitude Operator

RP – Recommended Practice

SCF – Stress Concentration Factor

SLLR – Super Long-life Regime

SST – Subsea Shuttle Tanker

VLFS – Very Large Floating Structures

WADAM – Wave Analysis by Diffraction and Morison Theory

List of Figures

Figure 1.1: Subsea Shuttle Tanker (Ma et al., 2021)	2
Figure 1.2: Environmental loading on the external hull of the SST	3
Figure 2.1: Multibody SST	9
Figure 2.2: Example of regular waves (left) and irregular waves (right)	13
Figure 2.3: Comparison between PM and JONSWAP spectrum	16
Figure 2.4: Typical two-segment S-N curve (Du et al., 2015)	21
Figure 2.5: Rain-flow counting method (American Bureau of Shipping, 2003)	23
Figure 2.6: General approach of the Time-Domain method (American Bureau of Shipping, 2003)	29
Figure 2.7: Different crack models (American Bureau of Shipping, 2003)	31
Figure 3.1: Main hydro capabilities: Calculation of radiation force using state-space model....	35
Figure 4.1: General arrangements of compartments (A: flooded mid-body, B: free flooding bow compartment, C: free flooding aft compartment, and D: bulkhead-buoyancy tank connection (Ma et al., 2021)	46
Figure 4.2: Flounder diagram of the SST (Ma et al., 2021).....	49
Figure 4.3: SST coordinate SST	50
Figure 4.4: SST 2-D planar Simulink model (7 bodies)	52
Figure 4.5: SST's control system block	54
Figure 5.1: Bending moment convergence study (Regular waves: $H = 1$ m and $T = 10$ secs).....	59
Figure 5.2: Time series response of heave and pitch for different numbers of bodies (Regular waves: $H = 1$ m and $T = 10$ secs).....	60
Figure 5.3: Bending moment response at (a) 520 secs, (b) 525 secs and (c) 530 secs	61
Figure 5.4: Time series response (LC1 load case)	62
Figure 5.5: Power spectral density at different location for LC1, LC2 and LC3 load cases	64
Figure 6.1: Statistical behaviour of fatigue life (Xin, 2013).....	66
Figure 6.2: Definition of different stresses (DNV, 2010b).....	68
Figure 6.3: The 3-D model of the mid-body section	69
Figure 6.4: (a) Cross-section of the external hull stiffener (DNV, 2018); (b) Weld details.....	70

Figure 6.5: Mesh convergence study for 2D axisymmetry model - Mesh refinement model and corresponding max. equivalent stress at welds	73
Figure 6.6: Plot of mesh convergence study of 2D axisymmetric model.....	74
Figure 6.7: Plot of mesh convergence study of 3D model.....	75
Figure 6.8: 3D ANSYS model showing fine mesh.....	75
Figure 6.9: Load and boundary condition for 2D axisymmetric model (Left) and shell model (Right).....	76
Figure 6.10: Equivalent stress plot: 3D model loaded with bending moment (a) and 2D axisymmetry model loaded with external pressure (b).....	77
Figure 6.11: S-N curves in seawater with cathodic protection(CP) (DNV, 2015)	81
Figure 6.12: Fatigue damage at different longitudinal locations	84
Figure 6.13: Fatigue life (years) at different longitudinal locations	85

List of Tables

Table 2.1: Different spectral models for different regions (Chakrabarti, 2005).....	14
Table 2.2: Summary of hydrodynamic and hydrostatic forces	18
Table 4.1: SST’s design parameter (Ma et al., 2021)	45
Table 4.2: Dry weight and volume distribution of various components (Ma et al., 2021).....	47
Table 4.3: SST external hull dimensions (Ma et al., 2021)	48
Table 4.4: Internal tank properties of the SST (Ma et al., 2021)	48
Table 5.1: Load cases for simulation	56
Table 5.2: A case study for the bending moment assessment.....	57
Table 5.3:PID controller gains	58
Table 5.4: Statistical summary for bending moment for LC1, LC2 and LC3 load cases	63
Table 5.5: Statistical comparison for bending moment for LC1, LC2 and LC3 at 40 m and 70 m water depth.....	65
Table 6.1: Properties of stiffeners (Ma et al., 2021)	70
Table 6.2: Material properties of the SST section (Ma et al., 2021).....	71
Table 6.3: Summary of elements type	72
Table 6.4: SCF calculated using ANSYS for different models and different loadings	77
Table 6.5: Resultant SCF from combined external pressure and bending.....	79
Table 6.6: S-N curve parameters for C1	80
Table 6.7: Representative sea states and their probability of occurrence	82
Table 6.8: Summary of wave-induced fatigue at 40 m and 70 m water depth	85
Table 6.9: Summary of fatigue life due to hydrostatic pressure	86

Chapter 1 – Introduction

1.1. Motivation and Background

The global carbon dioxide (CO₂) emissions in the earth's atmosphere are one of the primary causes of global warming and climate change. Since the beginning of the twenty-first century, global CO₂ emissions have steadily climbed from 12,165 million tons (MT) in 1990 to 38,016 MT in 2019. Based on the Emission Database for Global Atmospheric Research (Crippa et al., 2020), this considerable increase in CO₂, around 70%, is caused by the combustion of fossil fuels and extensive deforestation. According to the experts and climate advisory, CO₂ emissions must be reduced by 2030; or the globe will ensure permanent losses. The world's most sensitive ecosystem would be in jeopardy (Allen et al., 2019; Masson-Delmotte et al., 2018).

Global warming and CO₂ emissions have emerged as a crucial topic of discussion in the Paris agreement (United Nation, 2015), which aims to limit global warming by 1.5 °C. According to the agreement, greenhouse gas (GHG) emissions (i.e., mainly CO₂) must be lowered by at least 55 percent by 2030 compared to 1990. Carbon capture and storage (CCS) technology is crucial in meeting this goal by capturing CO₂ emissions from various sources and transporting them to safe and secure sites, such as subsea wells. CO₂ emissions from different industrial processes may now be collected and stored in significant quantities (Carbon Capture and Storage Association, 2020). As a result, any strategy that increases overall global CCS storage capacity in an economically feasible way is crucial for limiting the growing trend in the earth's mean temperature rise.

Pipelines transfer most offshore oil and gas production from host facilities to onshore facilities for further processing (Fullenbaum et al., 2013). Since the first subsea pipeline was installed during World War II in the United Kingdom, pipeline installation techniques have improved significantly and are now considered mature technology (Palmer & King, 2008). Transporting hydrocarbon using pipelines comes with some economic and technical limitations. One key limitation is installation cost which might be prohibitively expensive for a remotely located small field. Furthermore, pipeline inspection, maintenance, and repair become very challenging and costly, especially for deep water remote marginal fields. This suggests that the pipeline favours big fields with small step-outs and high-profit margins (Wilson, 2008).

Shuttle tankers are frequently deployed as an alternative to pipelines due to their ability to operate flexibly on demand (Vestereng, 2019). Since the tanker ships are floating structures subjected to enormous dynamic load effects from winds and waves, their operations are very weather-dependent and cannot be carried out in rough and extreme sea states. Various autonomous vehicles such as subsea gliders and freight submarines (Xing, 2021), are being developed as an alternative solution to the abovementioned problems. As an innovative solution, the idea of a Subsea Shuttle Tanker (SST) was introduced by Equinor in two research disclosure in 2019. The SST is a 34000-tonne novel sizeable autonomous vessel used to transport liquid CO₂ from onshore-offshore facilities to subsea wells, see Figure 1.1. The primary design consideration for SST was investigated by Xing et al., (2020) to make it economically feasible. Later, the baseline design for SST is presented by Ma et al., (2021).

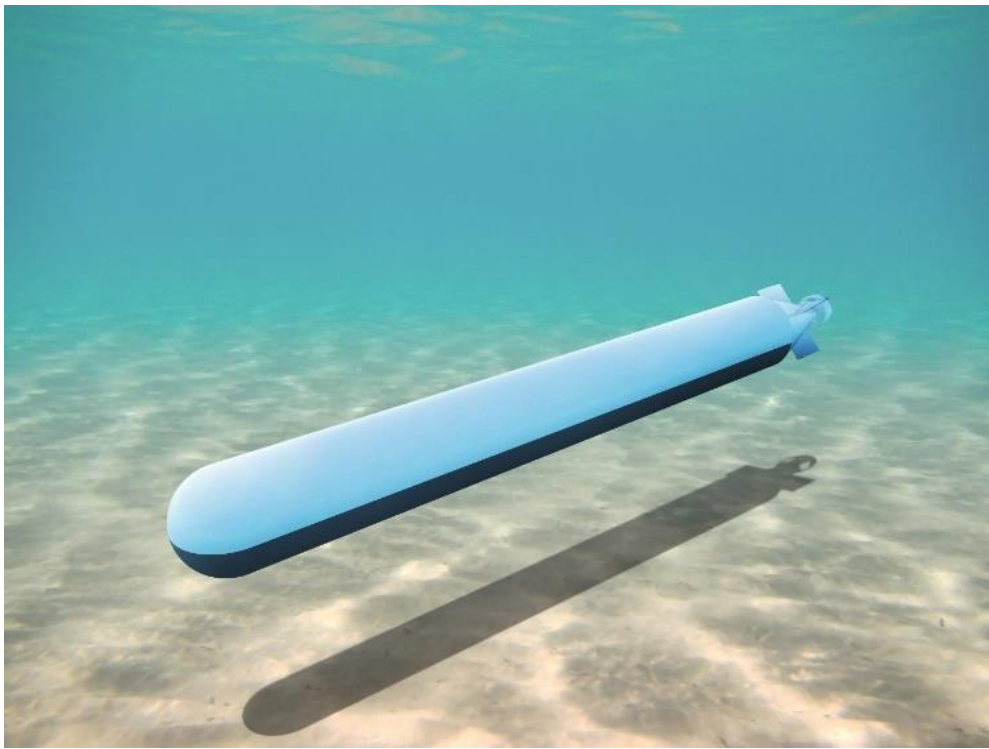


Figure 1.1: Subsea Shuttle Tanker (Ma et al., 2021)

During operation, the SST travels at the speed of 6 knots for best energy efficiency at the nominal diving depth of 70 m to reduce the wave impacts (Ma et al., 2021). At the stated water depth, the wave-induced loads on the external hull of the SST are decreased significantly. However, to

accurately estimate the structural performance of the SST hull, it is still necessary to explain and quantify this decrease in wave-induced loads in the given operating condition. These wave-induced loads, dynamic external pressure, and internal pressure loads (dynamic pressure from liquid cargo or ballast water) can potentially cause fatigue damage to the external pressure hull of the vessel. Furthermore, because the SST has a significant length-to-beam ratio, the external hull of the vessel can be deformed by a combination of wave loads and non-uniform buoyancy and weight distribution. The dynamic pressure variation with the water depth that has a positive value under the wave crest and a negative value under the wave trough is shown in Figure 1.2.

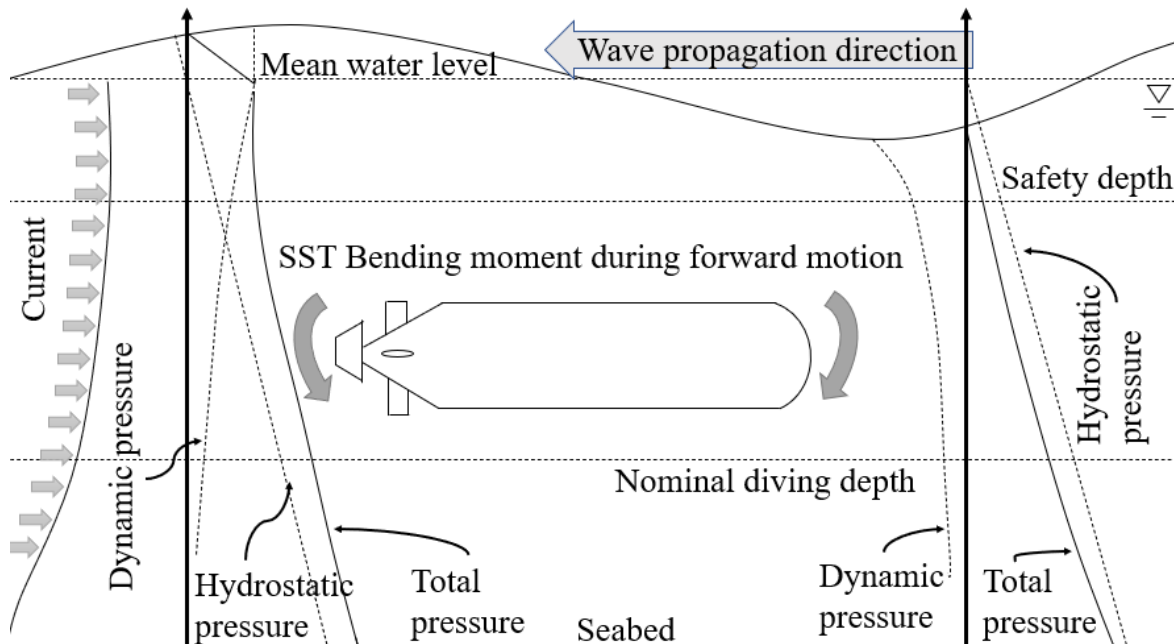


Figure 1.2: Environmental loading on the external hull of the SST

1.2. Objectives of the thesis

The thesis proposes a reliable and efficient multibody approach for a structural assessment of the SST external hull. The structural assessment is carried out in two different parts as mentioned below:

1. A multibody approach is used to model and analyze the bending moment in the SST under the effect of waves. The aim is to develop the multibody seakeeping planar model using Matlab Simulink. The bending moment responses are obtained under hydrodynamic loads, considering hydroelectricity and connection stiffness.
2. The objective of second half of the thesis is fatigue damage assessment of the SST external hull using the Rainflow counting approach and Palmgren-Miner rule considering local structural detail.

1.3. Outline

- Chapter 1: Introduction
Background of the Subsea Shuttle Tanker and its applicability, problem statement and the objective of the thesis.
- Chapter 2: Literature review and methodology
Discuss the past research related to the topic. A detailed explanation of the multi-body concept, multi-body equation of motion, potential flow theory, hydrodynamic and hydrostatic forces, and fatigue assessment methods.
- Chapter 3: Approach
Properties of the parametric model and different methods to identify the parametric model. Justification for selecting the FDI toolbox for this thesis.
- Chapter 4: Subsea Shuttle Tanker (SST) planar model design
A 2D planar Simulink model and an explanation for selecting the PID controller for the analysis are presented. Introduce the design input data used in the analysis.
- Chapter 5: Bending moment assessment using the multibody approach

Introduction to the bending moment assessment and analysis procedure. Carry out convergence study, time-domain and frequency-domain analysis and study the effect of water depth.

- Chapter 6: Fatigue assessment of the Subsea Shuttle Tanker hull

Introduction to fatigue assessment and analysis procedure. Finite element (FE) analysis to determine stress concentration factor (SCF). Discuss fatigue response due to waves and change in hydrostatic pressure due to dive-in and dive-out.

- Chapter 7: Conclusions and recommendations for future work

Discuss the main results of the thesis and propose future work.

Chapter 2 – Literature review and methodology

2.1. Previous work

Much research has already been done on Very Large Floating Structures (VLFSs) such as terminal airports, passenger and cargo ships, emergency bases, bridges, and so on (Lu et al., 2019). However, very little work has been done regarding reliable and efficient structural assessment on large autonomous submarines. In this thesis, the author has extended the previous works on VLFSs and suggested a reliable and efficient multibody approach to determine the bending moment responses and fatigue damage assessment using the frequency-time domain method under the influence of wave-induced loads.

Understanding the interaction between the external hull of SST and fluid fields is very important. The classical hydrodynamic approach assumes a rigid body assumption. It overlooks the influence of structural deformation and provides inaccurate hydrodynamic response estimation. The hydro-elastic theory accurately determines the large floating structures' response. It combines the hydrodynamic equations and structural dynamics, accounting for the interaction between inertia, hydrodynamic and elastic forces (Lu et al., 2019). These theories and multibody analysis methods are used to study several VLFSs. Hong, Kim, Cho, et al., (2003) numerically investigated global and local motion responses of multibody VLFSs such as side-by-side moored shuttle tanker and floating production storage and offloading (FPSO) systems. The latter results were compared with the model test results. Choi & Hong, (2002) studied the hydrodynamic interaction of a floating multibody system using the higher-order boundary element method (HOBEM). The findings are examined for two distinct unloading configurations, side-by-side and tandem. Yu et al., (2004) analyze the reactions and connection forces of a multibody movable offshore base system by numerically assuming bodies to be rigid. Several approaches have been used to analyze hydro-elastic responses of the offshore structures, including the mode superposition method (Hong et al., 2001; Humamoto & Fujita, 2002; Masashi, 1997), the direct method (Sim, 1998; Yasuzawa et al., 1997) and the eigenfunction expansion method (Hong, Kim, Shin, et al., 2003; Sim, 1998). Using the multibody equation of motion, Kim et al., (2007) analyze the shear forces, bending moment, and stresses at the VLFS connections. Adding all hydrodynamic responses at each node determines the total structural motions. However, because of the non-uniform shape or stiffness, achieving

these responses in each mode is difficult. As a result, the direct technique is utilized to investigate structures whose modes are very challenging to determine.

Fatigue damage is one of the most common causes of damage to most fixed and floating offshore structures. Cumulative fatigue damage is the most commonly used approach, which was first proposed by Palmgren and later modified and refined by Miner. The latter approach is not yet fully resolved and comes with uncertainties (Wirsching et al., 2006; Wirsching & Light, 1980). The most commonly used fatigue assessment methods in practice are the deterministic method, the spectral method, and the time-domain analysis method (Ariduru, 2004) based on the Rainflow counting approach (Matsuishi & Endo, 1968; Rychlik, 1987). This chapter's later section briefly describes the fatigue assessment methods.

Low & Cheung, (2012) proposed a new tailored approach based on a multi-peaked third-order asymptotic approximation. Zhao, (2012) suggested a practicable approach with intermediate accuracy for predicting fatigue life, including Super Long Life Regime (SLLR) and fatigue reliability. For the fatigue damage analysis of the offshore wind turbine (OWT), a novel statistical simplified technique based on a multivariate linear statistical approach is suggested (Zwick & Muskulus, 2016). The maximum error of the last-mentioned approach was only around 6.4% compared to the time-domain fatigue analysis. Robles et al., (2000) proposed a method to determine the fatigue damage of the submarine pressure hull using linear elastic fracture mechanics and the Paris equation. The geometry functions would be very beneficial for approximating the fatigue crack growth rate in the fracture mechanics technique (Haselbozchaloe et al., 2022). However, most fatigue assessment methods are associated with complex expressions. These limit their implementation in the actual design and can only be used to certain scenarios (Du et al., 2015). Furthermore, several of these new approaches are associated with uncertainties. The uncertainties associated with wave-induced fatigue loads and how they affect the crack growth of various offshore structures are studied by (Dong et al., 2022).

2.2. Multibody concept

The SST's continuous flexible hull is divided into multibody rigid modules with no deformation, see Figure 2.1. Each subsequent neighboring body is connected using a flexible spring. Each body has six-degree of freedom (DOF) motion. The motion of each body is influenced by the hydrodynamic interaction with its neighboring body. For bending moment analysis and fatigue damage assessment, linear wave theory assumptions are used to address the hydrodynamic characteristics i.e., incompressible, non-viscous, irrotational flow and small wave steepness waves. Then, based on the potential flow theory, hydrodynamic coefficients (added mass, damping, response amplitude operators RAOs etc.) are obtained for the multibody SST. The potential flow theory divides the structural load into the radiation and wave excitation effects. Finally, bending moment responses of the multibody SST are obtained by solving the multibody equation of motion in the presence of waves. The bending stiffness of the spring is considered only in pitch direction. It is because the work is limited to the 2-D planar model of the SST. Eq. (2.1). provides the bending stiffness of the spring in the pitch direction.

$$K_{\theta} = \frac{4EI}{L} \quad (2.1)$$

where, K_{θ} is the bending stiffness in pitch direction, I is the moment of inertia around y-axis, E is Young's modulus, and L is the length of each rigid module.

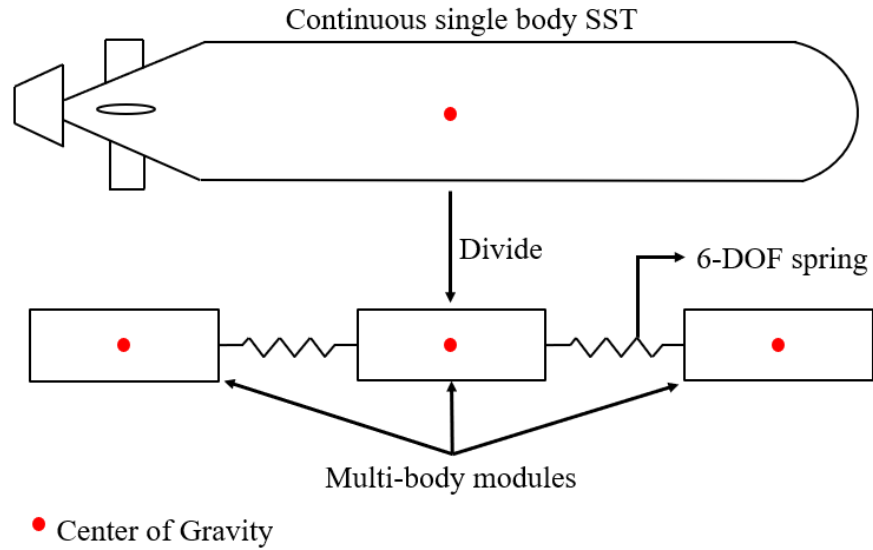


Figure 2.1: Multibody SST

2.3. Wave theory

It is essential to understand the ocean waves and their interactions with the SST hull during its motion. The theory of ocean waves and how they interact with a moving SST are discussed in this section.

When the wind blows over the ocean, it generates ocean waves by forcing the water's surface to move. Other origins of the ocean waves include earthquakes and Coriolis force. The SST is subjected to both regular and irregular waves in this thesis. Regular waves are sinusoidal and are generated when the constant wind blows for a long duration. On the other hand, irregular waves are composed of the superposition of many regular waves with different frequencies or periods.

2.3.1. Linear wave theory

In this section, the fluid particle's equation of motion and pressure is derived using Linear wave theory, also called Airy wave theory (Falnes & Kurniawan, 2002). Wave motion is described as a velocity potential using a few assumptions and approximations. This theory assumes fluid to be incompressible (constant density), non-viscous, and irrotational.

We start by looking at the two fundamental fluid dynamic equations: the Continuity and the Navier-Stokes equation (Kundu et al., 2015). The continuity equation for an incompressible flow is given as follows

$$\nabla \cdot V = 0 \quad (2.2)$$

where V is the velocity vector (x, y, z).

The simplified Navier-Stokes equation, also known as the Euler equation (Kundu et al., 2015), is given by

$$\rho \frac{DV}{Dt} = \rho \left(\frac{\partial V}{\partial t} + (V \cdot \nabla)V \right) = -\nabla p + f \quad (2.3)$$

where $\frac{DV}{Dt}$ is the material derivative of the velocity, p is the fluid's total pressure, and f is any external force acting on the fluid (for example, gravitational restoring force).

Velocity potential

The ocean water is assumed inviscid, irrotational, and incompressible. The velocity vector $V(x, y, z, t) = (u, v, w)$ can be described with a velocity potential ϕ (Faltinsen, 1993)

$$V = \nabla \phi = i \frac{\partial \phi}{\partial x} + j \frac{\partial \phi}{\partial y} + k \frac{\partial \phi}{\partial z} \quad (2.4)$$

where, i, j and k are unit vectors along the $x, y,$ and z axes in the cartesian coordinate system, respectively. There is no physical meaning of a velocity potential, but it is often used to analyze irrotational fluid motion. When the vorticity vector ($\omega = \nabla \times V$) is zero, the fluid is said to be irrotational. Also, it is assumed that water is incompressible (i.e., $\nabla \cdot V = 0$), then the velocity potential ϕ must satisfy the Laplace equation (Faltinsen, 1993)

$$\frac{\partial^2 \phi}{\partial x^2} + \frac{\partial^2 \phi}{\partial y^2} + \frac{\partial^2 \phi}{\partial z^2} = 0 \quad (2.5)$$

The solution of the Laplace equation with appropriate boundary conditions on the fluid is used to determine the velocity potential of incompressible and irrotational fluid motion. The boundary conditions are covered in the later part of the section.

The pressure p is given using Bernoulli's equation. If we assume the z -axis to be vertical and positive upwards (Faltinsen, 1993), we can write

$$p + \rho g z + \rho \frac{\partial \phi}{\partial t} + \frac{\rho}{2} V \cdot V = C \quad (2.6)$$

where C is a constant. Eq. (2.6) assumes only gravity as an external force field and is valid for inviscid, unsteady and irrotational fluid motion.

Boundary conditions

Bottom boundary condition (BBC): The fluid velocity at the sea bottom ($z = -h$) is zero. We are considering a flat bottom, where h is the water depth (Faltinsen, 1993).

$$\dot{z} = \frac{\partial \phi}{\partial z} = 0, \quad \text{when } z = -h \quad (2.7)$$

Kinematic free surface boundary condition (KBC): The vertical velocity of the fluid particle at the free surface must be the same as the vertical velocity of the free surface in the same direction (Faltinsen, 1993).

$$\frac{\partial \phi}{\partial z} = \frac{\partial \eta}{\partial t} + \frac{\partial \eta}{\partial x} \cdot \frac{\partial \phi}{\partial x} \quad (2.8)$$

where $\eta(x, t)$ is the free surface of the water.

Dynamic free surface boundary condition (DBC): Fluid pressure along the free surface must be constant and equal to the atmospheric pressure (Faltinsen, 1993). Using Eq. (2.6) at the surface, we have $p = p_0$ and $z = \eta$ which gives

$$g\eta + \frac{\partial \phi}{\partial t} + \frac{1}{2} \cdot \left(\frac{\partial \phi^2}{\partial x} + \frac{\partial \phi^2}{\partial z} \right) = 0 \quad (2.9)$$

It is challenging to obtain the analytical solution to the problem because boundary conditions at the free surface $\eta(x, t)$ are nonlinear and the governing equation of the free surface is missing. Mathematical simplification is needed. The following boundary conditions can be linearized (disregard the square terms) by assuming small wave steepness and thus η can be neglected from the equations (apply KBC and DBC at $z = 0$ instead of $z = \eta$) (Faltinsen, 1993). The approximated and simplified KBC and DBC are given as

$$\text{KBC} \quad \frac{\partial \phi}{\partial z} = \frac{\partial \eta}{\partial t}, \quad \text{at } z = 0 \quad (2.10)$$

$$\text{DBC} \quad \frac{\partial^2 \phi}{\partial x^2} + g \cdot \frac{\partial \eta}{\partial t} = 0, \quad \text{at } z = 0 \quad (2.11)$$

No flow is permitted through the outer hull of the SST. Therefore, velocity of the fluid particles perpendicular to the SST surface is equal to the normal component of the SST velocity v_n (Falnes & Kurniawan, 2002)

$$\frac{\partial \phi}{\partial n} = v_n \quad (2.12)$$

2.3.2. Ocean waves

Ocean waves are typically irregular waves and composed of the superposition of many regular waves with different amplitudes and frequencies. The surface elevation of the ocean waves as a function of time for regular and irregular waves is illustrated in Figure 2.2.

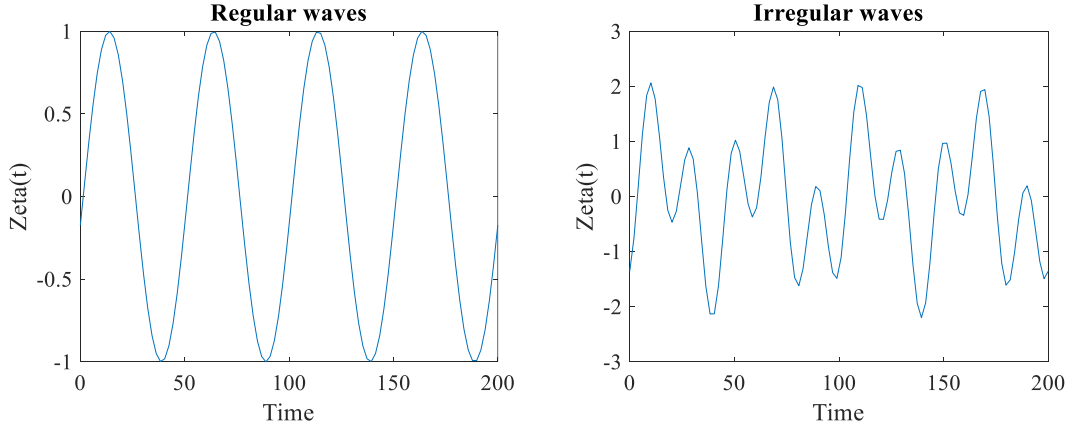


Figure 2.2: Example of regular waves (left) and irregular waves (right)

Regular waves

Regular waves are sinusoidal and are generated when the constant wind blows for a long duration in deep water condition. A sinusoidal function can be used to describe the surface elevation of the regular waves propagating in the x direction at the given time instance t (Faltinsen, 1993).

$$\eta(x, t) = \frac{H}{2} \cos(\omega t - kx) \quad (2.13)$$

where $H/2$ is the amplitude of the regular waves (m), ω is the wave frequency (rad/sec), k is the wave number which is defined as $k = 2\pi/\lambda$ and λ is the wavelength (m).

Irregular waves

The significant wave height H_s and spectral peak period T_p are the most important characteristics of irregular waves. H_s is defined as the average value of the one-third highest wave height of the incoming waves. T_p is defined as the wave period where we have the maximum value of the frequency spectrum.

The surface elevation of irregular waves is given as a superposition of many individual regular waves components.

$$\eta(x, t) = \sum_{n=1}^M A_n \cos(\omega_n t - k_n x + \theta_n) \quad (2.14)$$

where A_n , ω_n , k_n , and θ_n is the amplitude, frequency, wave number, and phase shift of the n^{th} wave, respectively. The phase shift is generated randomly between $[0, 2\pi]$.

Sea spectrum model

Sea spectrum models are empirical. They are built using real-time ocean wave measurements data, measured over long periods. The most often used spectrums are the Pierson-Moskowitz (PM), ISSC, and Joint North Sea Wave Project (JONSWAP) models. These models show the amount of energy transported in the waves over the frequency range. These models are used to estimate the various critical responses of offshore structures. The energy density spectrum depends on the significant wave height H_s and spectral peak period T_p . The H_s and T_p values depend on the long-term sea states of a particular geographical location (Chakrabarti, 2005). Table 2.1 proposes which model to adopt in various regions throughout the world.

Table 2.1: Different spectral models for different regions (Chakrabarti, 2005)

Location	Operational	Survival
North Sea	JONSWAP	JONSWAP
Northern North Sea	JONSWAP	JONSWAP
Gulf of Mexico	PM	PM or JONSWAP
Offshore Brazil	PM	PM or JONSWAP
West Africa	PM	PM
Western Australia	PM	PM
Offshore Newfoundland	PM	PM or JONSWAP

Pierson-Moscowitz model

The Pierson-Moscowitz (PM) spectrum was developed using the measurements taken in the North Atlantic Ocean. The spectrum describes the wave elevation for a fully developed sea at infinite fetch. The following formula describes the PM spectrum (DNV, 2010c)

$$S_{PM}(\omega) = \frac{5}{16} H_s^2 \omega_p^4 \omega^{-5} \exp\left(-\frac{5}{4} \left(\frac{\omega}{\omega_p}\right)^{-4}\right) \quad (2.15)$$

where $\omega_p = 2\pi/T_p$ and ω is the frequency (rad/sec)

Joint North Sea Wave Project (JONSWAP) models

JONSWAP spectrum was developed using the measurements done in the Southern North Sea. Under specific wind conditions, this spectrum represents sea states that have not fully developed. The JONSWAP model is an updated version of the PM model with a peak enhancement factor controlled by a peak shape parameter γ (DNV, 2010c). JONSWAP spectrum is given as follows

$$S_j(\omega) = A_\gamma S_{PM}(\omega) \gamma^{\exp\left(-0.5\left(\frac{\omega-\omega_p}{\sigma\omega_p}\right)^2\right)} \quad (2.16)$$

where γ is a peak shape parameter, σ is a spectral width parameter ($\sigma = \sigma_a$ for $\omega \leq \omega_p$ and $\sigma = \sigma_b$ for $\omega \geq \omega_p$), and $A_\gamma = 1 - 0.287\ln(\gamma)$ is a normalizing factor. Figure 2.3 illustrates a comparison between the PM and the JONSWAP spectrum. The time series of the wave elevation can be generated from the energy spectrum using Fast Fourier Transformation (FFT). On the other hand, the wave elevation time series can be converted to the frequency domain using inverse Fourier Transformation.

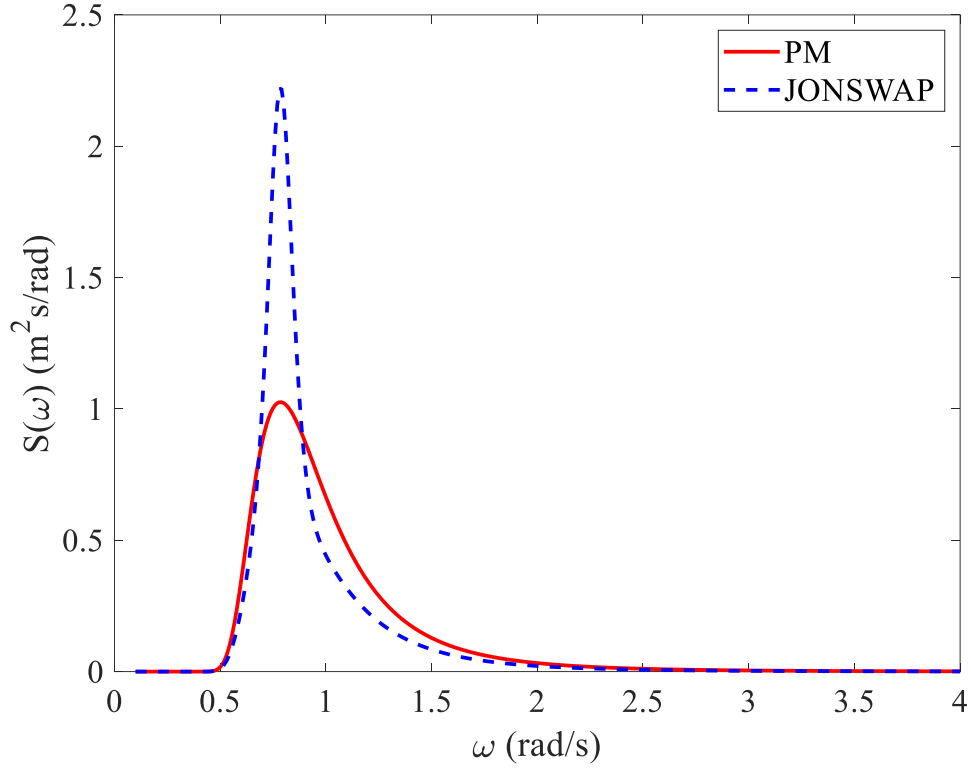


Figure 2.3: Comparison between PM and JONSWAP spectrum

This thesis uses the Joint North Sea Wave Project (JONSWAP) spectrum to model irregular waves.

2.4. Hydrodynamic forces

For any marine vessels and offshore structures, the equation of motion can be given as

$$M_{RB}\ddot{\xi} = \tau \quad (2.17)$$

where M_{RB} is the rigid body mass matrix, ξ is the displacement vector with respect to the global coordinate system and τ is force and moment vector in a body-fixed coordinate system.

$$\tau = \tau_{ext} + \tau_{res} + \tau_{visc} + \tau_{rad} \quad (2.18)$$

where τ_{ext} is the excitation force by incident waves (Froude Krilov (FK) force and Diffraction force), τ_{res} is the restoring force (gravity and buoyancy), τ_{visc} is the viscous force and τ_{rad} is the radiation force due to a change in momentum of the water particles.

We saw in section 2.3.1 that a velocity potential ϕ represents fluid motion. The velocity potential is divided into three different potentials (Faltinsen, 1993):

$$\phi = \phi_0 + \phi_d + \phi_{rad} \quad (2.19)$$

where ϕ_0 is the undisturbed wave potential, ϕ_d is the diffraction potential due to the presence of fixed structures in incoming waves and ϕ_{rad} is the radiation potential when the structure is forced to oscillate with an arbitrary amplitude in calm water. The different velocity potential allows us to calculate the individual forces acting on the structure (Faltinsen, 1993). The velocity potential ϕ for time-varying sinusoidal waves can be given as

$$\phi(x, t) = Re[\widehat{\phi}(r)e^{i\omega t}] \quad (2.20)$$

where $\widehat{\phi}(r)$ is the space-dependent complex amplitude, ω is the wave frequency and t is the time instant.

The forces on any marine and offshore structures are obtained from the pressure exerted by the fluid on the wetted surface S . Using Bernoulli equation (Eq. (2.6)) and velocity potentials (Eq. (2.19)), the pressure can be obtained (Faltinsen, 1993)

$$p = -\rho \frac{\partial \phi}{\partial t} - \rho g z = -\rho Re[i\omega(\widehat{\phi}_0 + \widehat{\phi}_d + \widehat{\phi}_{rad})] - \rho g z \quad (2.21)$$

Knowing the velocity potentials, calculating resulting forces (F) and moments (M) is straightforward just by integrating pressure over the surface S :

$$F = \iint_S (p \cdot \bar{n}) dS \quad (2.22)$$

$$M = \iint_S p(\bar{r} \times \bar{n}) dS \quad (2.23)$$

where n is the normal vector to the surface S and r is the location vector. Table 2.2 shows the summary of different hydrodynamic and hydrostatic forces acting on any marine and offshore structures.

Table 2.2: Summary of hydrodynamic and hydrostatic forces

Forces	Wave Excitation force	Restoring force	Viscous force	Radiation force
Abbreviation	τ_{ext}	τ_{res}	τ_{visc}	τ_{rad}
Origin	$\widehat{\Phi}_0, \widehat{\Phi}_d$	$-\rho g z$		$\widehat{\Phi}_{rad}$
Description	Forces on the structure when it is fixed in the incident waves	Hydrostatic restoring force	Forces due to the water friction (added externally to obtain the accurate structure response)	Forces on the body when it oscillates in water with no waves.

2.4.1. Excitation force

The excitation force on the marine and offshore structures can be calculated using undisturbed wave potential $\widehat{\Phi}_0$ and diffraction potential $\widehat{\Phi}_d$ (Faltinsen, 1993)

$$\tau_{ext} = -\rho \iint_S \bar{n} \operatorname{Re}[i\omega(\widehat{\Phi}_0 + \widehat{\Phi}_d)e^{i\omega t}] ds \quad (2.24)$$

2.4.2. Radiation force

Time-domain model

Cummin's equation is used to represent time-domain radiation force (Cummins et al., 1962)

$$\tau_{rad} = -A_{\infty}\ddot{\xi} - \int_0^t K(t-t')\dot{\xi}(t')dt' \quad (2.25)$$

where A_{∞} and K are the infinite frequency added mass and retardation function, respectively. The first term in Cummin's equation is the pressure force caused by the structure's acceleration. The following term in the equation represents energy transfer from the structure's motion to radiation waves. It shows the fluid memory model. The memory function's matrix is the kernel of the convolution term.

Using Eq. (2.17), (2.18) and (2.25), the equation of motion in time domain for any marine and offshore structures can be represented as (Cummins et al., 1962)

$$(M_{RB} + A_{\infty})\ddot{\xi} + \int_0^t K(t-t')\dot{\xi}(t')dt' + G\xi = \tau_{exc} \quad (2.26)$$

Frequency-domain model

The radiation force in the frequency domain is as follows (Faltinsen, 1993; Newman, 2018)

$$\tau_{rad}(j\omega) = -A(\omega)\ddot{\xi}(j\omega) - B(\omega)\dot{\xi}(j\omega) \quad (2.27)$$

where $A(\omega)$ and $B(\omega)$ are the frequency-dependent added mass and damping, respectively. The Eq. (2.26) can be rewritten in the frequency domain as

$$[-\omega^2[M + A(\omega)] + j\omega B(\omega) + G]\xi(j\omega) = \tau_{exc}(j\omega) \quad (2.28)$$

Ogilvie, (1964) uses the Fourier transform to demonstrate the link between added mass and damping coefficients in the time and frequency domains.

$$A(\omega) = A_\infty - \frac{1}{\omega} \int_0^\infty K(t) \sin(\omega t) dt \quad (2.29)$$

$$B(\omega) = \int_0^\infty K(t) \cos(\omega t) dt \quad (2.30)$$

Again, using Fourier transform, the frequency domain retardation function is as follows:

$$K(j\omega) = B(\omega) + j\omega[A(\omega) - A_\infty] \quad (2.31)$$

The hydrodynamic coefficients are found utilizing hydrodynamic codes (WADAM) for a finite set of frequencies. These codes are based on the potential flow theory.

To sum up, the equation of motion for the multibody SST in the frequency domain is presented as follows:

$$[-\omega^2[M_k + A_{kk}] + j\omega B_{kk} + G]\xi + \sum_{j=1, j \neq k}^n [-\omega^2 A_{kj} + j\omega B_{kj}]\xi = \tau_{exc}(j\omega) \quad (2.32)$$

where M_k is the rigid mass matrix of the SST, A_{kk} is the added mass matrix of the k^{th} body caused by the motion itself, B_{kk} is the damping matrix caused by the motion of the k^{th} body itself, G is restoring or hydrostatic force, ξ is the displacement vector, n is the number of rigid modules, A_{kj} and B_{kj} is the added mass matrix and damping matrix of the k^{th} body caused by the motion of the j^{th} body. The total number of equations equals the total number of bodies.

Identification of the Radiation-force model

A simulation model based on the Cummin equation (Cummins et al., 1962) can be built using a non-parametric fluid memory model. The latter approach requires knowing the previous time step's data to calculate the convolution integral. This can be very time consuming and extremely challenging to implement. Therefore, to overcome this problem, the linear time-invariant parametric model is used to solve the fluid memory model.

$$\mu_{ij} = \int_0^t K_{ij}(t - t') \dot{\xi}(t') dt' \quad \approx \quad \begin{aligned} \dot{x}_{ij} &= \hat{A}_{ij} x_{ij} + \hat{B}_{ij} \dot{\xi}_j \\ \hat{\mu} &= \hat{C}_{ij} x_{ij} \end{aligned} \quad (2.33)$$

where \hat{A} , \hat{B} and \hat{C} are the states of the system and x is the fluid memory effect or state vector.

Eq. (2.33) can be presented in the frequency domain as

$$K(j\omega) \approx \hat{K}(j\omega) = \hat{C}(j\omega I - \hat{A})^{-1}\hat{B} \quad (2.34)$$

where $\hat{K}(s)$ is the transfer function. Estimating the transfer function by canonical realization yields a state-space model Eq. (2.33).

2.5. Preliminaries of fatigue analysis

The preliminaries of fatigue analysis, including the S-N curve approach, the rain-flow counting approach and the Palmgren-Miner rule are explained briefly in this section.

2.5.1. S-N curve approach

The stress-cycles (S-N) curve approach is used to calculate nominal stress fatigue life (American Bureau of Shipping, 2003). These curves are obtained using the results of the experiments. A typical two-segment S-N curve is seen in Figure 2.4 (Du et al., 2015).

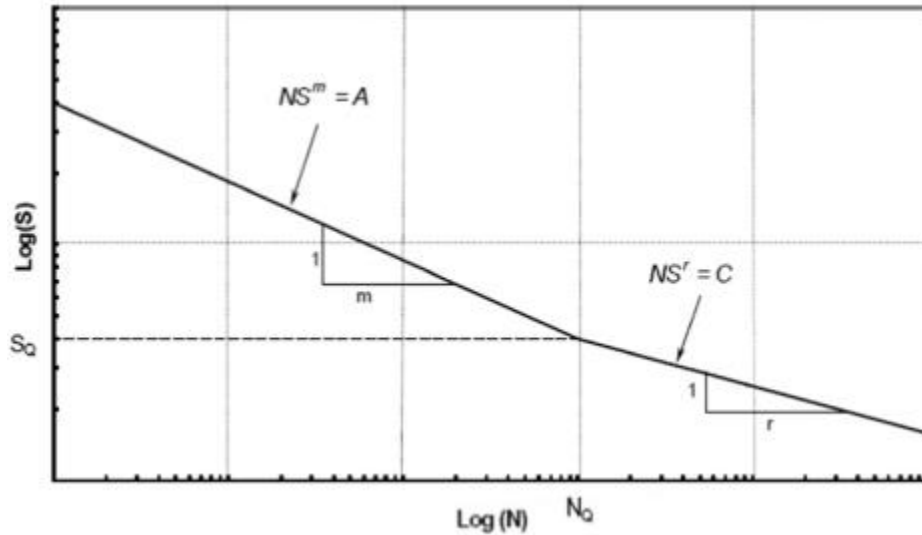


Figure 2.4: Typical two-segment S-N curve (Du et al., 2015)

$$N = AS^{-m} \quad (2.35)$$

where S is the stress range, N is the no. of cycles to failure for a constant stress range, m is the fatigue strength exponent, and A is the fatigue strength coefficient. m and A can be empirically determined from the fatigue experiments. Three types of S-N curves correspond to the different operating conditions for different structures: 'A' is for in air condition, 'FC' is for 'free corrosion,' and 'CP' is for cathodic protection (DNV, 2010a). Because corrosion protection measures are usually employed for marine and offshore structures, the S-N curves under the 'CP' condition are used in this thesis's fatigue study.

2.5.2. Rain-flow counting method

The cycle counting approach is used to describe irregular stress-time series by quantifying the number of cycles of varying sizes. The number of cycles can be provided using different methods, such as peak counting, level-crossing counting, range-pair counting, simple-range counting and rain-flow counting. Among all the cycle counting approaches which are mentioned earlier, (Matsuishi & Endo, 1968) introduced the Rainflow counting method, which is based on the notion of hysteresis owing to a random fluctuation of loadings and ignores the sequence of stress series. Furthermore, the stress cycles range related to low and high frequency, and wave frequency components are identified using the rain-flow counting approach. Many research studies show that the Rainflow counting approach produces reliable fatigue damage (Dowling, 1971).

Figure 2.5 (left) illustrates the stress time series and its 90° rotation on the right. The rules of this method are summarized below (American Bureau of Shipping, 2003):

- 1) Suppose there is a source of water for each trough illustrated in Figure 2.5 (right). The water moves downward along the path off the trough or “roof”.
- 2) When the water path reaches a more negative trough (e.g., point 5 in Figure 2.5 (right)) than the original starting point (e.g., point 1 in Figure 2.5 (right)), this defines a one stress range called S_1 , which includes the mean value of the stress cycle.

- 3) When the path starts from a certain point (e.g., point 3 in Figure 2.5 (right)), it comes to an end when it hits another path. This results in another stress range S_2 .
- 4) The same procedure is followed for the entire stress time series.
- 5) The procedure mentioned above can also be performed by considering the crest of water source. The obtained stress cycles must match the cycles of the trough generated process.

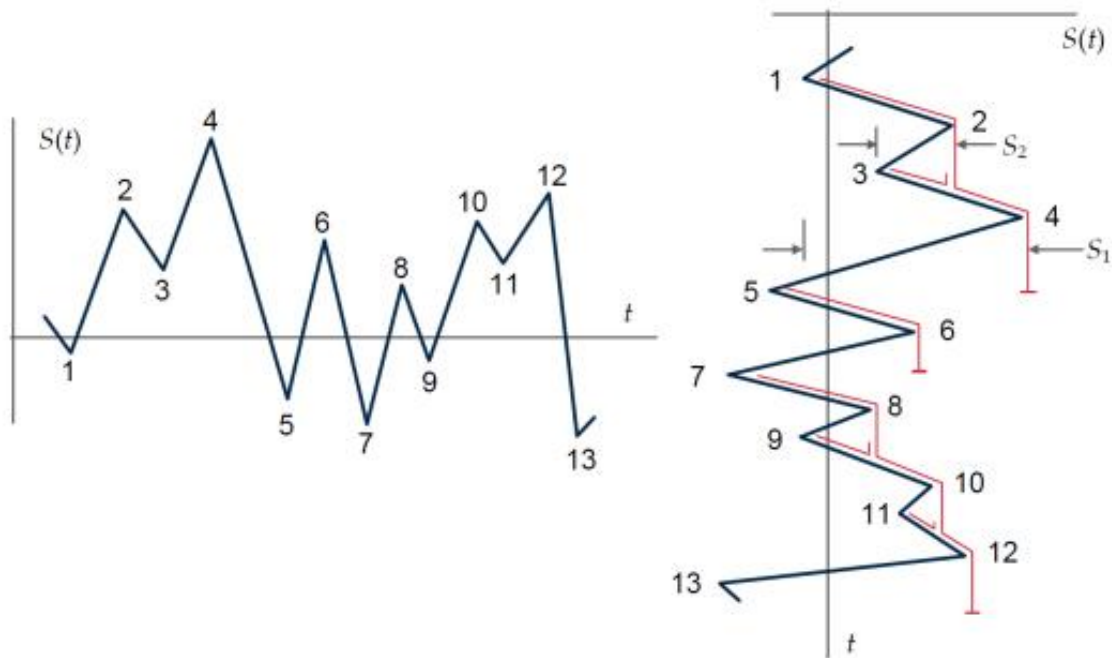


Figure 2.5: Rain-flow counting method (American Bureau of Shipping, 2003)

2.5.3. Palmgren-miner rule

The fatigue damage caused by the structural stress can be calculated as a ratio of the actual number of cycles (n) of that stress range to the number of cycles (N) that will result in the fatigue damage at that stress range. The number of cycles to failure (N) is determined using the S-N curve. The Palmgren-Miner Rule (Miner, 2021) states that cumulative or total fatigue damage is the summation of the individual damage from all stress range intervals. The following formula can be used to calculate the annual fatigue damage acquired in a single state (American Bureau of Shipping, 2003)

$$D_i = \frac{365 \times 24 \times 3600 \times p_i}{d_i} \sum_j \frac{n_{ij}}{N_j} \quad (2.36)$$

where D_i is the accumulated or total fatigue damage in the i^{th} sea state, d_i is the duration of the dynamic simulation of the i^{th} sea state, p_i is the probability of the occurrence of the i^{th} sea state, n_{ij} is the actual number of cycles of that stress range j in the i^{th} sea state, N_j is the number of cycles that result in fatigue damage at the stress range j determined using the S-N curve.

2.6. Fatigue assessment methods

This section briefly describes the most widely used fatigue assessment methods.

2.6.1. Deterministic method

For many years, the deterministic method has proven to be reliable for dynamically insensitive structures. This method is more suitable where all fatigue waves have considerably longer wave periods to prevent peaks and valleys in the transfer function of the structure. The given method does not use transfer function or wave spectra to determine stress range values but performs a small number of discrete wave analyses (Rohith & Jayalekshmi, 2017).

An appropriate number of deterministic periodic waves with the specified wave height H_i and wave period T_i must be selected to define the relationship between stress range and wave height, where i represents the specific sea states in the wave scatter. The analysis procedure considers the number of occurrences of each wave and corresponding stress ranges to determine the annual fatigue damage is as follows (Du et al., 2015):

- 1) Determine the number of times the i^{th} sea state has occurred.

$$n_i = \frac{365 \times 24 \times 3600 \times p_i}{T_i} \quad (2.37)$$

where p_i is the probability of the occurrence of the i^{th} sea state.

- 2) Calculate the stress range y_i on the marine and offshore structures applied by the wave force of the i^{th} sea state.
- 3) Based on the S-N curve and Eq. (2.35), compute the number of cycles to failure N_i for the stress range y_i .
- 4) Finally, using Palmgren-Miner Rule, calculate the total or cumulative fatigue damage.

The main disadvantage of the deterministic method includes the inability to account for the actual distribution of energy across the entire wave frequency range. Furthermore, the actual relationship between the transfer function cannot be considered. This is because this method ignores the random nature of the irregular waves. As a result, the wave's stochastic characteristics are ignored. Also, it is quite sensitive to the choice of waves and their associated period (Rohith & Jayalekshmi, 2017).

2.6.2. Spectra fatigue damage method

The long-term sea state can be represented during the design of marine and offshore structures by a series of discrete short-term sea states that are regarded as stationary Gaussian stochastic processes. The sea states are usually described using the wave scatter diagram. It is assumed that wave-induced stress variation on any marine and offshore structures is a narrow-band Gaussian process in a particular sea state (American Bureau of Shipping, 2003). Therefore, for each short-term sea state, the peak value of stresses (y) would follow the Rayleigh distribution.

$$f(y) = \frac{y}{\sigma_y^2} \exp\left(-\frac{y^2}{2\sigma_y^2}\right) \quad (2.38)$$

$$f(S) = \frac{S}{\sigma_y^2} \exp\left(-\frac{S^2}{8\sigma_y^2}\right) \quad (2.39)$$

where y , S and σ_y are the stress amplitude, range (double amplitude, $S = 2y$) and standard deviation of stress, respectively. The spectral density function of the stress response is the square of the stress RAOs times the wave spectrum.

$$G_y(\omega|H_S, T_Z, \theta) = |H_\sigma(\omega|\theta)|^2 \times G_{\eta\eta}(\omega|H_S, T_Z) \quad (2.40)$$

where $G_y(\omega|H_S, T_Z, \theta)$ is the spectral density function of the stress response, $|H_\sigma(\omega|\theta)|$ is the stress RAOs, $G_{\eta\eta}(\omega|H_S, T_Z)$ is the wave spectrum, H_S is the significant wave height, T_Z is the zero up-crossing period and θ is the wave angle of the incident waves. The stress RAOs are defined as the stress amplitude of the marine and offshore structures induced by the wave loads per unit wave amplitude.

Following the acquisition of the spectral density function of the stress response, its zeroth, second and fourth order moment (m_0, m_2, m_4) and standard deviation of the stress series range σ_y can be represented as

$$m_r = \int_0^{+\infty} \omega^r G_y(\omega|H_S, T_Z, \theta) d\omega \quad (r = 0, 2, 4) \quad (2.41)$$

$$\sigma_y = \sqrt{m_0} = \sqrt{\int_0^{\infty} G_y(\omega|H_S, T_Z, \theta) d\omega} \quad (2.42)$$

Using the above equations (Eq. (2.38) - (2.42)), the annual cumulative fatigue damage in the i^{th} sea state can be computed as follows (American Bureau of Shipping, 2003):

$$D_i = \frac{n_i}{N_i} = \int_0^{\infty} \frac{365 \times 24 \times 3600 p_i f_{0i} f_i(S)}{A/S^m} dS \quad (2.43)$$

where f_{0i} and f_i is the zero up-crossing frequency in Hz and probability density function of the stress range in the i^{th} sea state, respectively, where $f_0 = (1/2\pi)\sqrt{m_2/m_0}$.

The cumulative fatigue damage to the marine and offshore structures can be determined by summing up the short-term damage over all available sea states in the particular wave scatter diagram (American Bureau of Shipping, 2003).

$$D = \sum_i D_i = \sum_i \int_0^{\infty} \frac{365 \times 24 \times 3600 p_i f_{0i} f_i(S)}{A/S^m} dS \quad (2.44)$$

As mentioned earlier, this method uses the Rayleigh distribution assumption that only considers narrow band Gaussian process when the bandwidth parameter is less than 0.5 (Gao & Moan, 2008). However, in real life, the stress response of any marine and offshore structures under the combination of wind, waves, and ocean currents is considered a wide-banded process (Hu et al., 2009). Wirsching & Light, (1980) propose a cycle counting correction factor to overcome this limitation. The ABS (American Bureau of Shipping, 2003) codes recommend this approach because it is simpler and more efficient than other factors (Benasciutti & Tovo, 2006). The cycle counting correction factor is given as

$$\lambda(m, \varepsilon_i) = a(m) + [1 - a(m)][1 - \varepsilon_i]^{b(m)} \quad (2.45)$$

$$a(m) = 0.926 - 0.033m \quad \text{and} \quad b(m) = 1.587m - 2.323 \quad (2.46)$$

where $\lambda(m, \varepsilon_i)$, m and ε_i are the cycle counting factor, fatigue strength exponent and spectral bandwidth, respectively. The spectral bandwidth ε_i can be defined as

$$\varepsilon = \sqrt{1 - \frac{m_2^2}{m_0 m_4}} \quad (2.47)$$

The corrected formula for the cumulative fatigue damage after considering the cycle counting correction factor can be expressed as

$$D = \sum_i D_i = \sum_i \int_0^\infty \frac{365 \times 24 \times 3600 p_i f_{oi} f_i(S)}{A/S^m} dS \lambda(m, \varepsilon_i) \quad (2.48)$$

2.6.3. Time domain method

As previously stated, both the deterministic and spectra fatigue damage methods have limitations. The former method does not account for the random nature of the irregular waves, while the latter method calculates the accumulated fatigue damage using the Rayleigh distribution assumption. On the other hand, the time-domain method uses coupled dynamic analysis and the Rainflow counting

method to calculate the accumulated fatigue damage of any marine and offshore structures (American Bureau of Shipping, 2003).

The time-domain method uses a time series of wave kinematics for over a short duration obtained from a specific wave spectrum. Hydrodynamic forces, which might incorporate nonlinear effects, are estimated and applied to the offshore structural model. As a result, in marine engineering simulations, one response history curve will always last for 3-hours. Stress responses are estimated using a time-domain approach. After obtaining a stress history, the Rainflow counting method is used to estimate the number of stress cycles n_s corresponding to the stress range s and generate a stress histogram. If the probability of the occurrence p_i of the i^{th} sea state is known then using Palmgren-Miner Rule fatigue damage caused by the the i^{th} sea state is expressed as (Du et al., 2015)

$$D_i = \sum_s \left(\frac{365 \times 24 \times p_i n_s}{3 N_s} \right) \quad (2.49)$$

where D_i is the fatigue damage caused by the the i^{th} sea state, n_s is the number of cycles obtained using the rain-flow counting method at the stress range s , N_s is the number of the cycle to fail at the stress range s . The annual accumulated fatigue damage can be calculated in the same way as the spectral damage method (Du et al., 2015)

$$D = \sum_i D_i = \sum_i \sum_s \left(\frac{365 \times 24 \times p_i n_s}{3 N_s} \right) \quad (2.50)$$

Because the given method directly evaluates the full time history, time-domain simulation is always regarded as a benchmark (Low, 2011). Like the other methods discussed earlier, the time-domain method also comes with some limitations. The calculation process is highly sophisticated because it is used for both load and corresponding structural analyses. Due to this, complicated structures sometimes require a very long computation time (Du et al., 2015).

The standard procedure of the time-domain approach for any marine structures is illustrated in Figure 2.6.

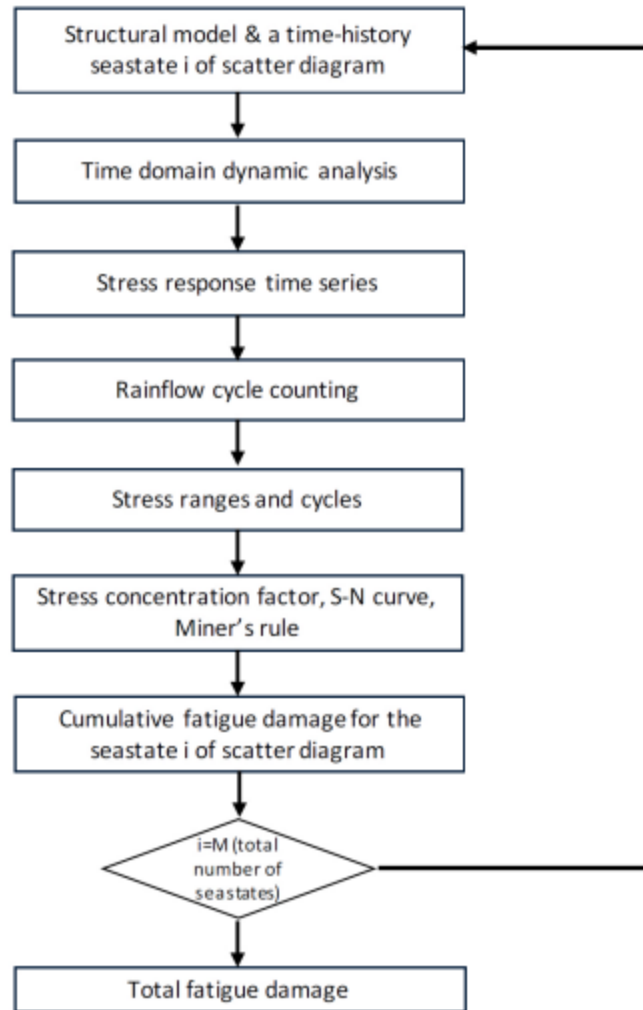


Figure 2.6: General approach of the Time-Domain method (American Bureau of Shipping, 2003)

2.6.4. Fatigue assessment based on fracture mechanics

Most of the time, S-N fatigue strength characterizations are typically used to calculate and evaluate the cumulative fatigue damage. But in some cases, the above methods become ineffective when the flaw is discovered. The fracture mechanics approach is used to determine the remaining life of the structure once a fault or crack is discovered. This method is advantageous for assessing fatigue crack propagation and is further used to create and improve inspection programs (American Bureau of Shipping, 2003).

This method is very effective in the case where S-N approach is inadequate or has to be modified or verified, for example (American Bureau of Shipping, 2003):

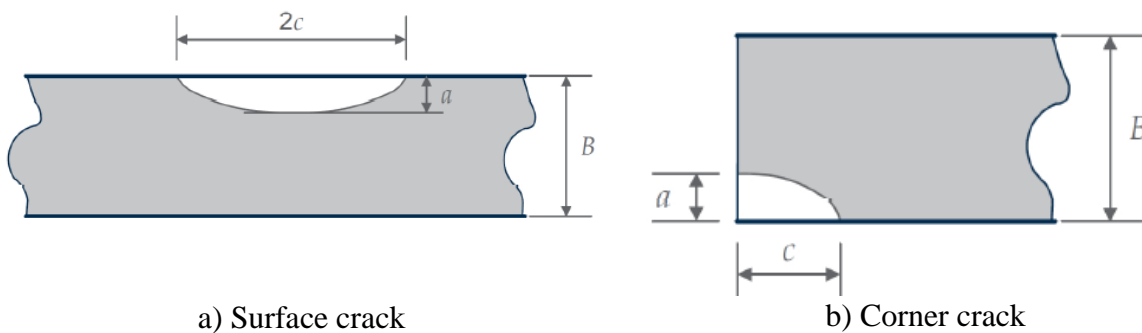
- 1) When determining the fitness for the purpose of joint/detail that is known to have defects, these defects are expensive and/or complex to repair, and 'repair/no repair choice must be taken.
- 2) When joint/detail is exceptional or exposed to various complicated stress concentrations, the standard S-N classification cannot fully describe it. ABS (American Bureau of Shipping, 2003) may necessitate extra fracture mechanics-based research in these exceptional circumstances.
- 3) When determining an aged structure's remaining fatigue life
- 4) When creating and revising in-service inspection planning strategies.

Comparison with the S-N technique may be used to base or calibrate the assumptions for the fracture mechanics analysis model. The crack growth rate da/dN and stress intensity factor range ΔK is used to characterize the Fatigue crack growth (American Bureau of Shipping, 2003).

Crack models

The length and depth of their enclosing rectangles are used to characterize the planar defects or cracks. The given method assumes that such defects or cracks are sharp-tipped cracks. Figure 2.7 illustrates the four different crack models (American Bureau of Shipping, 2003):

- A surface crack having a depth a and length $2c$
- A corner crack with length or depth a and c
- Through thickness crack with length $2a$
- Embedded crack with depth $2a$ and length $2c$



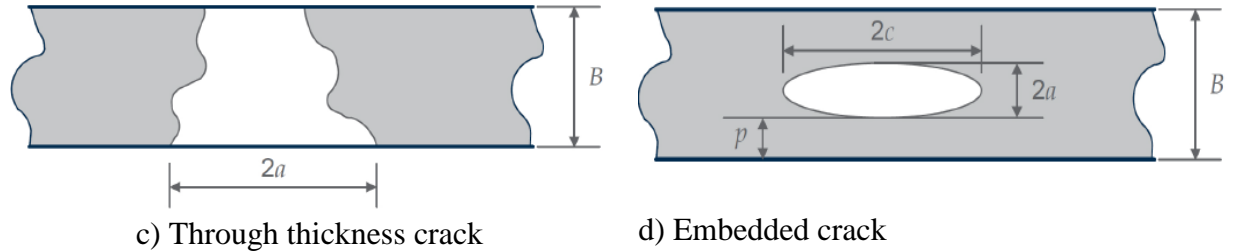


Figure 2.7: Different crack models (American Bureau of Shipping, 2003)

The Paris Law

The Paris Law gives the growth rate of the fatigue crack. The crack growth equation is expressed as (American Bureau of Shipping, 2003)

$$\frac{da}{dN} = C(\Delta K)^m \quad \text{for } \Delta K > \Delta K_{th} \quad (2.51)$$

$$\frac{da}{dN} = 0$$

where a is the crack size (length and/or depth), da/dN is the crack growth rate, ΔK is the stress intensity factor range, ΔK_{th} is the threshold value of stress intensity factor range, C and m are the Paris coefficient and Paris exponent.

The material and applied factors such as environment, stress ratio, waveform in the test and load frequency of the test, affect the Paris parameters C and m . The data applicable to the specific material under service circumstances should be utilized wherever feasible, and if there is any doubt about the influence of the environment, such data should also be gathered.

The crack propagation for two-parameter (a and c) elliptical or semi-elliptical cracks must be calculated for each size. The path of the fatigue crack growth is assumed to be perpendicular to the principal stress direction (American Bureau of Shipping, 2003).

Stress intensity factor range

The maximum principal stress should serve as a basis for the stress range. The stress intensity factor range ΔK depends on the crack shape and size (see Figure 2.7), stress range, and structural geometry (American Bureau of Shipping, 2003). It can be calculated using following equation

$$\Delta K = YS\sqrt{\pi a} \quad (2.52)$$

where S is the stress range and Y is the stress intensity correction factor. YS typically depends on loading and geometry, which also takes into account the contributions of primary stresses and secondary stresses. It is calculated using BS 7910 (British Standard, 2019). The accepted solution from the other sources can also be used as an alternative.

At the critical position, the cumulative impact of residual stresses and other secondary stresses such as thermal stresses must be considered. Refer to BS 7910 (British Standard, 2019) for a more detailed calculation procedure.

Life prediction – Crack size and number of cycles

The main objective is to find the crack size associated with the given life of the structure or, alternatively the number of cycles until failure. This is based on the assumption that real cracks may be modeled as sharp-tipped cracks (American Bureau of Shipping, 2003).

From Eq. (2.53), it is possible to calculate the number of cycles N needed for a crack to grow from its initial size a_i to its final size a (American Bureau of Shipping, 2003).

$$NS^m = \frac{1}{C} \int_{a_i}^a \frac{1}{[Y(x)]^m (\pi x)^{m/2}} dx \quad (2.53)$$

The failure is assumed when $a = a_c$, the critical crack size.

Determination of initial flaw size

The given methodology is significantly dependent on the initial crack size a_i . Several non-destructive testing (NDT) inspection methods can estimate the initial crack size during manufacturing. The correctness of the crack size strongly depends on the accuracy of NDT techniques (American Bureau of Shipping, 2003).

It is essential to assume an initial crack size in the design context. The maximum crack size will be considered in the calculation, taking into consideration the defect size for different geometries, fabrication welds and inspection accuracy. Suppose in case no relevant data on crack depth are

available, in that case, a crack depth of 0.5 mm may be assumed for surface cracks beginning at the weld/base material transition (American Bureau of Shipping, 2003).

Chapter 3 – Approach

Developing a control system for a maritime system is extremely difficult without an appropriate mathematical model. The Marine Systems Simulator (MSS) (Perez et al., 2006) includes the most frequently used hydrodynamic codes. Using the geometrical parameter of the SST and its loading conditions, these codes calculate hydrodynamic and hydrostatic coefficients (added mass, damping and restoring coefficients), body motion and excitation force transfer function (motion-RAOs and force-RAOs), mean-drift forces and moments.

3.1. Identification of the convolution integral using a parametric model

Adopting a parametric model to approximate the convolution term in the Cummins equation (Eq.(2.25)) is a feasible way to compute the free-surface memory effect more effectively. This can be accomplished using a state-space model given by Eq. (2.33).

The given approach identifies the state-space system using the matrices \hat{A} , \hat{B} and \hat{C} . One of the benefits of the chosen approach is the Markovian property of the state-space model, which assures that every future state of the system relies solely on the current value of the system states. In other words, unlike the convolution approach, no previous information has to be kept because the whole memory effect is included in the state vector x (Duarte, 2012).

Several methods for performing this system identification have been proposed in the literature, including (Hjulstad et al., 2004; Jordán & Beltrán-Aguedo, 2004; Kristiansen et al., 2005; McCabe et al., 2005; Perez & Fossen, 2009).

Using a hydrodynamic code “WADAM”, the frequency-dependent added mass and damping matrices is computed to obtain the state-space system represented by Eq. (2.33). The frequency domain retardation function is easily computed using Eq. (2.31), and the frequency response can be used to find the corresponding linear state-space model. Frequency-domain identification is the term given to this. However, the impulse-response function of the retardation function can be found directly using the inverse Fourier Transform of the retardation function or Eq. (2.29) and Eq. (2.30). With this Time-domain identification, the state-space model with the corresponding impulse-response can be found (Duarte, 2012).

In this thesis, the frequency-domain retardation function is computed to determine the radiation force. Figure 3.1 illustrates the step-by-step procedure to implement radiation force, Froude-Krylov (FK), and diffraction force in the Simulink.

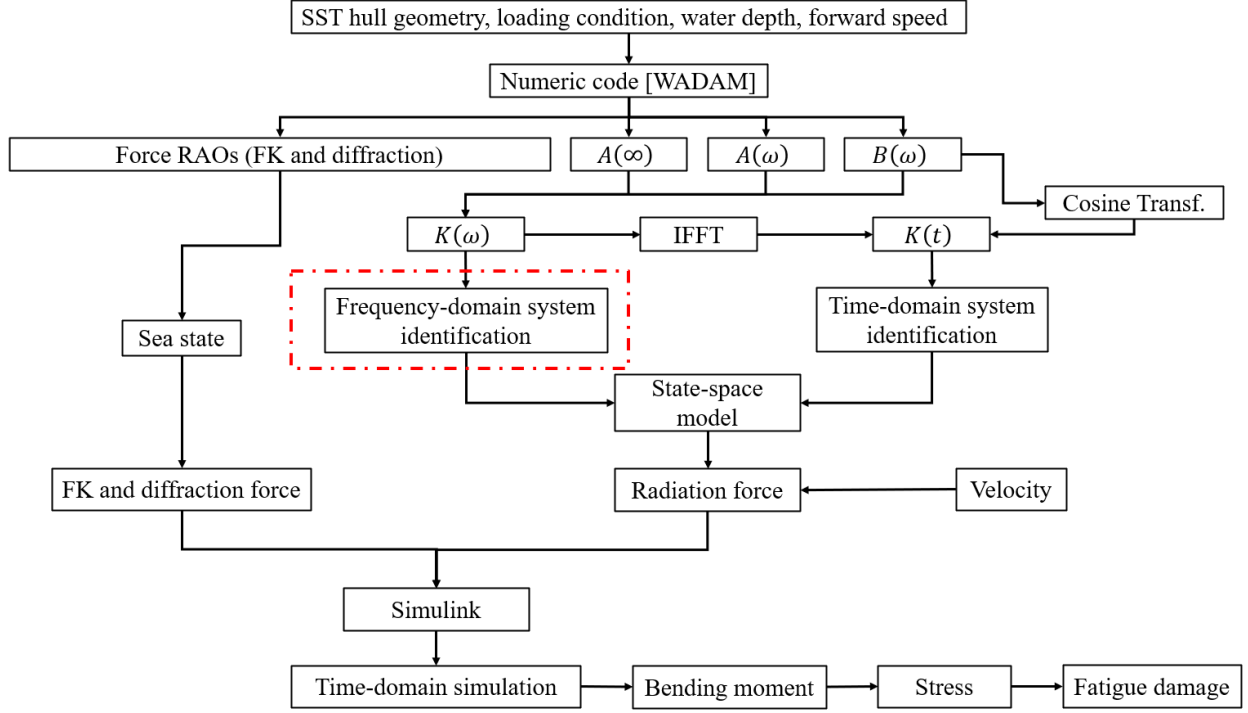


Figure 3.1: Main hydro capabilities: Calculation of radiation force using a state-space model

3.2. Properties of the parametric model

For each item of the retardation matrix, a parametric model or transfer function is fitted with the appropriate order (Duarte, 2012):

$$\tilde{K}_{ij}(s, \theta) = \frac{P(s, \theta)}{Q(s, \theta)} = \frac{p_m s^m + p_{m-1} s^{m-1} + \dots + p_0}{s^n + q_{n-1} s^{n-1} + \dots + q_0} \quad (3.1)$$

where $\theta = [p_m, \dots, p_0, q_{n-1}, \dots, q_0]$ is a vector containing the various parameters of the numerator and denominator, \tilde{K}_{ij} is the entry of the retardation matrix and $s = j\omega$. The parametric models or transfer functions should satisfy certain established properties. These properties were derived using radiation potential presented in (Perez & Fossen, 2009).

3.2.1. Low-frequency asymptotic value

The asymptotic value at low frequencies is given by (Duarte, 2012):

$$\lim_{\omega \rightarrow 0} K(\omega) = 0 \quad (3.2)$$

This assertion is founded on the notion that no structure can emit zero-frequency waves. If Eq. (2.30) is used to estimate the retardation function, then the function must have a zero at $\omega = 0$. This implies that p_0 must be zero (Duarte, 2012).

3.2.2. High-frequency asymptotic value

The high-frequency limit of the retardation function must be 0 (Duarte, 2012):

$$\lim_{\omega \rightarrow \infty} K(\omega) = 0 \quad (3.3)$$

Eq. (2.31) is used to demonstrate this. Because the structure cannot emit waves of infinite frequency, the damping limit must be zero and the $A_{ij}(\omega) - A_\infty$ will tend to zero when $\omega \rightarrow \infty$. For detailed information, see (Falnes & Kurniawan, 2002).

To ensure this property, $\deg\{Q(s, \theta)\} > \deg\{P(s, \theta)\}$. This shows that the denominator increases faster than the numerator with ω , and because of this, the function goes to zero when the frequency tends to be infinite (Duarte, 2012).

3.2.3. Initial time value

The time-domain retardation function must start with a value other than zero. This is demonstrated by Eq. (2.30) (Duarte, 2012):

$$\lim_{t \rightarrow 0} K_{ij}(t) = \lim_{t \rightarrow 0} \frac{2}{\pi} \int_0^\infty B(\omega) \cos(\omega t) d\omega = \frac{2}{\pi} \int_0^\infty B(\omega) d\omega \neq 0 \quad (3.4)$$

Using Laplace transformation to Eq. (3.4):

$$\lim_{t \rightarrow 0} K_{ij}(t) = \lim_{s \rightarrow \infty} sK_{ij}(s) = \lim_{s \rightarrow \infty} s \frac{P(s)}{Q(s)} = \frac{p_m s^{m+1}}{s^n} \quad (3.5)$$

Eq. (3.5) shows that the relative order of the denominator and numerator must be one ($n = m + 1$) to cause the limit to be finite and different from 0 (Duarte, 2012).

When this condition is combined with the requirements of the first property described, it is simple to deduce that the minimal order function is second order. This can be represented as (Duarte, 2012):

$$\tilde{K}_{ij}^{min}(s) = \frac{p_1 s}{s^2 + q_1 s + q_0} \quad (3.6)$$

3.2.4. Final time value

When the time approaches infinity, the response of a stable system tends to zero. The limit specified in this property ensures that the radiation system is stable for inputs and outputs that are within certain bounds (Duarte, 2012):

$$\lim_{t \rightarrow 0} K_{ij}(t) = \lim_{t \rightarrow 0} \frac{2}{\pi} \int_0^{\infty} B(\omega) \cos(\omega t) d\omega = 0 \quad (3.7)$$

As a result, the poles of the transfer function $K_{ij}(s)$, which are the zeros of the denominator must have a negative real part (Duarte, 2012).

3.2.5. Passivity

The characteristic of systems that can store and discharge energy but cannot produce it is described as passivity. The Cummins equation can be expressed for a floating body with no external force or incident waves as (Duarte, 2012):

$$M\ddot{\xi}_i + C_{ij}^{hydrostatic}\dot{\xi}_j = F_i^{radiation} \quad (3.8)$$

The change in energy of this system becomes:

$$E(T) - E(0) = \int_0^T F_i^{radiation} \dot{\xi}_i dt \quad (3.9)$$

As a result, the convolution term of the radiation force is passive. More detailed information can be given in (Perez & Fossen, 2009). Passivity can be assured for linear and time-invariant systems if the retardation matrix is real and positively defined in the frequency domain (Duarte, 2012):

$$\Re\{\tilde{K}_{ij}(s, \theta)\} = \Re\left\{\frac{P_{ii}(s, \theta)}{Q_{ii}(s, \theta)}\right\} > 0 \quad (3.10)$$

3.3. Different methods to identify parametric model

Four methods can be used to identify the parametric model. The methods are as follows (Duarte, 2012):

- Frequency-domain identification methods
 - 1) FREQ
 - 2) FDI toolbox
- Time-domain identification methods
 - 1) Least squares method
 - 2) Realization theory

Among all the methods given above, the FDI toolbox based on the frequency-domain identification method is used in this thesis to identify the parametric model. The following section will explain the FDI toolbox method in detail. A description of the other methods is not provided in this thesis. However, detailed information can be found in the ssfitting manual (Duarte, 2012).

3.3.1. Frequency-domain identification method

With the frequency-response of the convolution integral obtained using Eq. (2.31), a parametric model with the proper order for each element of the retardation matrix can be fitted (Duarte, 2012):

$$\tilde{K}_{ij}(s, \theta) = \frac{P(s, \theta)}{Q(s, \theta)} = \frac{p_m s^m + p_{m-1} s^{m-1} + \dots + p_0}{s^n + q_{n-1} s^{n-1} + \dots + q_0} \quad (3.11)$$

$$\theta = [p_m, \dots, p_0, q_{n-1}, \dots, q_0] \quad (3.12)$$

Using the Least Square (LS) method, there is an optimization problem involved in finding the approximate model $\tilde{K}_{ij}(s, \theta)$ and θ (Duarte, 2012):

$$\theta = \underset{\theta}{\operatorname{argmin}} \sum_l \left(K_{ij}(s) - \tilde{K}_{ij}(s, \theta) \right)^2 \quad (3.13)$$

This problem is solved using the FDI toolbox, with is presented in the following section.

3.3.2. FDI Toolbox

The Frequency Domain Identification (FDI) Toolbox is created by Perez and Fossen (Perez & Fossen, 2009). The Matlab function *invfreqs* is used to solve the Least Square (LS) method. The optimization problem (Eq. (3.13)) is made linear by the utilization of weight factors for the frequency range that is considered to be the most significant:

$$\theta = \underset{\theta}{\operatorname{argmin}} \sum_l w_l \left(K_{ij}(s) - \tilde{K}_{ij}(s, \theta) \right)^2 \quad (3.14)$$

where w_l is the weight factor ranging from 0 to 1 for each frequency. The approach is based on the Levy method (Levy, 1959) and is solved interactively (Sanathanan & Koerner, 1963). The optimization problem (Eq. (3.14)) can be solved using three different approaches (Duarte, 2012):

- 1) The first approach uses linearized LS minimization. This approach is similar to the **FREQ** method

- 2) The second approach solves an iterative linear LS problem using previous denominator values as a weight factor.
- 3) The third approach uses a Gauss-Newton algorithm to solve the non-linear LS problem.

All of the previous approaches make use of the function *invfreqs*. According to (Perez & Fossen, 2009), the iterative linear LS problem has the most optimal computing time/accuracy ratio. Therefore, the second approach is chosen for this thesis. To account for the properties of the retardation functions, the toolbox employs the following algorithm:

- 1) Configure the appropriate frequency range based on the user-defined weight variables.
- 2) Scale the data:

$$\tilde{K}'_{ij} = \alpha \tilde{K}_{ij}; \quad \alpha = \frac{1}{\max |K_{ij}|} \quad (3.15)$$

- 3) Choose the approximation order $n = \deg(\tilde{Q}_{ij}(s, \theta))$. The starting point of the order is 2.
- 4) The iterative LS method is used to estimate the parameter θ .

$$\theta_p = \arg \min \sum_l \left| \frac{K_{ij}(s)}{s} - \frac{\tilde{P}_{ij}(s, \theta)}{\tilde{Q}_{ij}(s, \theta)} \right| \quad (3.16)$$

- 5) Verify for stability by calculating the poles or roots of $\tilde{Q}_{ij}(s, \theta)$ and changing the real part of these poles or roots from positive to negative.
- 6) Scale the appropriate transfer function and include the s factor in the numerator

$$\tilde{K}'_{ij} = \alpha \frac{s \tilde{P}_{ij}(s, \theta)}{\tilde{Q}_{ij}(s, \theta)} \quad (3.17)$$

- 7) Determine the added mass and damping by utilizing the identified parametric approximation and compare it with $A(\omega)$ and $B(\omega)$ obtained by the 3D diffraction/radiation algorithm. If the fitting is unacceptable, increase the approximation order and repeat step 3.
- 8) If required, check for passivity $\Re\{\tilde{K}'_{ij}(s, \theta)\} > 0$

The method's fourth step guarantees that the parametric model's first property is satisfied. The second and third properties are also met by ensuring that the functions always have a relative order of one. Fifth step forces system stability, while the eighth step verifies passivity. By incorporating this prior knowledge into the fitted functions, this method guarantees that most of the properties of the parametric model are satisfied. This results in a lower-order transfer function that is more accurate. The state-space model can be easily derived from the transfer function (*tf2ss.m*) (Duarte, 2012). The Matlab code of frequency-domain identification of radiation model is provided in Appendix B

3.4. Matrix assembly

The collection of state-space systems is derived for each significant entry of the retardation matrix K using the method described in the previous section. Several state-space systems are obtained using Eq. (2.33).

$$\mu_{ij} = \int_0^t K_{ij}(t-t') \dot{\xi}(t') dt' \quad \approx \quad \begin{aligned} \dot{x}_{ij} &= \hat{A}_{ij} x_{ij} + \hat{B}_{ij} \dot{\xi}_j \\ \hat{\mu} &= \hat{C}_{ij} x_{ij} \end{aligned} \quad (2.33)$$

where i and j vary from 1 to m and m is the number of degrees of freedom of rigid-body. This and the following equations do not use Einstein notation. The size of the retardation matrix K is $m \times m$. Only the main diagonal values and a few off-diagonal values of the retardation matrix are non-negligible for most of the floating bodies. The size of each matrix is as follows: $\hat{A}_{ij} = [n_{ij} \times n_{ij}]$, $\hat{B}_{ij} = [n_{ij} \times 1]$, $\hat{C}_{ij} = [1 \times n_{ij}]$ and $x_{ij} = [n_{ij} \times 1]$, where n_{ij} is the number of states used to approximate the entry K_{ij} (Duarte, 2012).

Each of the matrices \hat{A}_{ij} , \hat{B}_{ij} and \hat{C}_{ij} must be assembled into a global state-space system to obtain the complete state-space system. The assembly can be done in following ways (Duarte, 2012):

$$\begin{aligned} \dot{x}_r &= A_r x_r + B_r \dot{\xi} \\ \mu &= C_r x_r \end{aligned} \quad (3.18)$$

$$x_r = [n \times 1] = \begin{bmatrix} x_{11} \\ \vdots \\ x_{1m} \\ x_{22} \\ x_{21} \\ \vdots \\ x_{2m} \\ x_{mm} \\ x_{m1} \\ \vdots \\ x_{mm-1} \end{bmatrix} \quad \dot{\xi} = [m \times 1] = \begin{bmatrix} \dot{\xi}_1 \\ \dot{\xi}_2 \\ \vdots \\ \dot{\xi}_m \end{bmatrix} \quad (3.22)$$

where n is the total number of radiation states and m is the total degree of freedom of the rigid body. The matrices are arranged by the first subscript and the diagonal term $[x_{ii}]$ comes first, followed by the remaining cross-term with the same index $[x_{ij}]$. The negative sign in front of C_r matrix represents the negative sign on the memory term in Eq. (2.25).

The Matlab code to determine a state-space model to compare free-surface memory effect is provided in Appendix C.

Chapter 4 – Subsea Shuttle Tanker (SST) planar model design

The Finite element (FE) technique is adopted to determine the structural performance of many marine and offshore structures in many practical cases. FE analysis on a huge structure like SST comes with high computation time and expenses. Therefore, this thesis presents a more efficient and reliable multibody approach. The proposed methodology is based on the discrete-module-beam bending-based hydroelasticity method.

This chapter describes the modelling and dynamics of the Subsea Shuttle Tanker (SST). First, the vessel's design parameters and dry weight and volume distribution are presented. Later, a planar seakeeping multibody model is prepared using Matlab Simulink (Simscape Multibody toolbox), which is an alternative to FEM analysis to determine the bending moment response of the SST hull. The SST is designed using several blocks (see, Figure 4.4) and simulated in Matlab, allowing the dynamics of the SST to be recorded and finally represented. Several studies on SST have been done in past using Matlab Simulink, including developing depth control modelling of SST (Ma et al., 2021), determining the safety envelope and trajectory envelope of a SST (Ma et al., 2022; Ma & Xing, 2022), and modelling of SST hovering in ocean currents (Xing et al., 2022). When designing an autonomous underwater vehicle like SST, it is essential to ensure that the vessel stays in its intended position. Several controllers, like Linear Quadratic Regulator (LQR) (Ma et al., 2022) and Proportional Integral Derivative (PID) controllers (Ma et al., 2021), can be used to maintain the position-keeping ability of the vessel in the waves.

4.1. Design parameters of the SST

The main parameters of the novel sizeable autonomous vehicle are given by (Ma et al., 2021), see Table 4.1. The SST is a 33,619-ton autonomous submarine vessel with length and beam measurements of 164 and 17 meters, respectively. Its cargo-carrying capacity is up to 16,362 m³ of CO₂ and has a range of approximately 400 km at a speed of 6 knots (Ma et al., 2021).

In this thesis, the author has not focused more on the individual aspect of the baseline design of the vessel. Detailed information can be found in (Ma et al., 2021).

Table 4.1: SST’s design parameter (Ma et al., 2021)

Parameter	Unit	Value
Length	m	164
Beam	m	17
Total mass (m)	kg	3.36×10^7
Pitch moment of inertia (I_{yy})	$\text{kg} \cdot \text{m}^2$	3.63×10^9
Centre of buoyancy [x_b, y_b, z_b]	m	[0, 0, -0.41]
Skeg position (x_s)	m	67
Skeg area (A_s)	m	40
Carbon dioxide capacity	kg	1.7×10^6

4.2. General arrangements

The following section briefly explains the various compartment arrangement, weight and space distribution inside the SST.

4.2.1. Compartments

Figure 4.1 illustrates the general arrangements of the various tanks in the SST. Two watertight bulkheads, as illustrated in Figure 4.1, separate the SST into three compartments (Ma et al., 2021):

- Free flooding bow compartment: It includes radio, sensors, forward trim and compensation tank, control station, sonar, and offloading pumps.
- Flooded mid-body: It is the longest compartment. It includes piping, buoyancy, and cargo tanks.
- Free flooding aft compartment: It includes several moisture-sensitive equipment such as rudder controls, motor, battery, gearbox, aft trim, and compensation tanks.

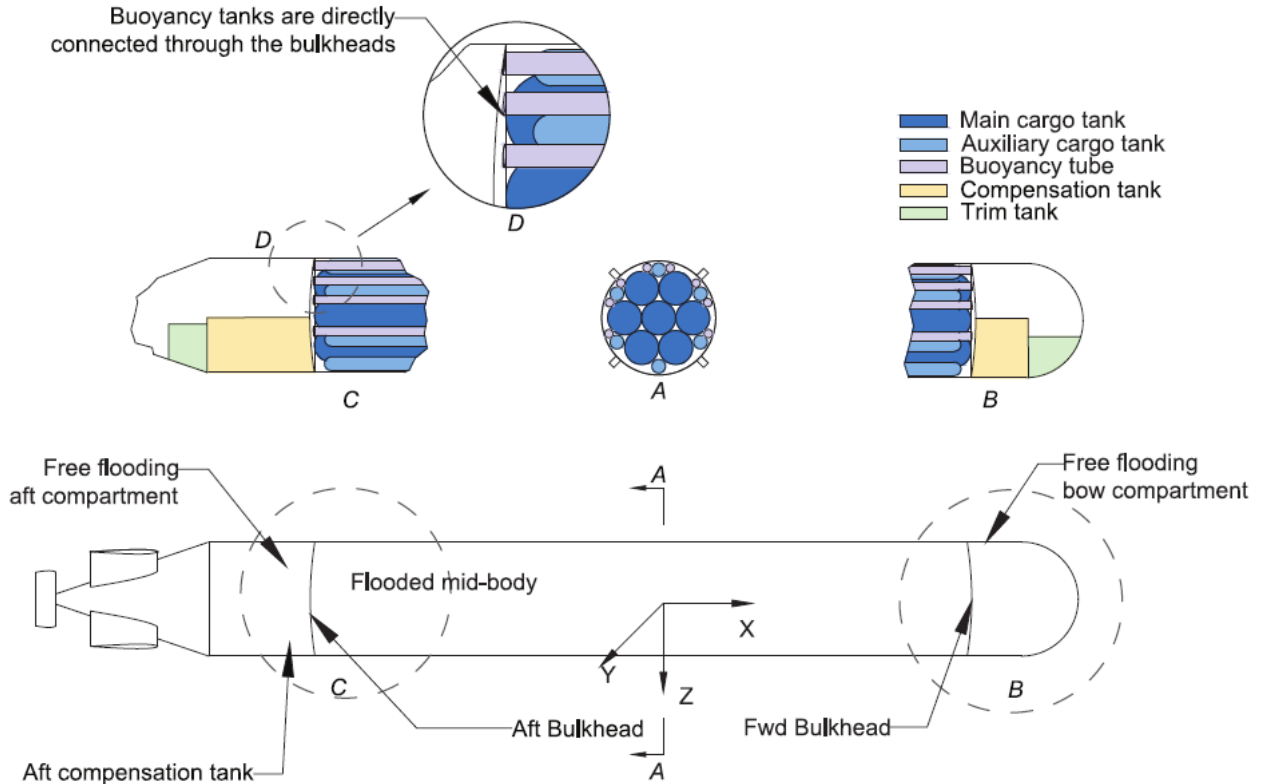


Figure 4.1: General arrangements of compartments (A: flooded mid-body, B: free flooding bow compartment, C: free flooding aft compartment, and D: bulkhead-buoyancy tank connection (Ma et al., 2021))

4.2.2. Weights and spaces distribution

The dry weights, centers of gravity and volume distribution of the main components of the SST are illustrated in Table 4.2. The centroid of the flooded mid-body is set as the origin of the coordinate system. Figure 4.2 illustrates the Flounder diagram of the vessel. The Flounder diagram is used to analyze the volume distribution as described in Table 4.2. It illustrates the SST space distribution over the vessel length without considering the precise design. The lateral axis represents the longitudinal location of the SST, while the vertical axis defines the cross-section area (Ma et al., 2021). The space requirement of individual volume components is represented in the diagram, see Figure 4.2.

Table 4.2: Dry weight and volume distribution of various components (Ma et al., 2021)

Components	Weight [ton]	Center of gravity [m]	Volume [m³]
External hull	2666	(-7.1, 0.0, 0.0)	32,799
Auxiliary cargo tank 1	171	(0.0, -7.1, 0.0)	475
Auxiliary cargo tank 2	171	(0.0, 6.2, -3.6)	475
Auxiliary cargo tank 3	171	(0.0, 6.2, 3.6)	475
Auxiliary cargo tank 4	171	(0.0, 7.1, 0.0)	475
Auxiliary cargo tank 5	171	(0.0, -6.2, 3.6)	475
Auxiliary cargo tank 6	171	(0.0, -6.2, -3.6)	475
Main cargo tank 1	681	(0.0, 0.0, 0.0)	1931
Main cargo tank 2	681	(0.0, 5.0, 0.0)	1931
Main cargo tank 3	681	(0.0, 2.5, 4.3)	1931
Main cargo tank 4	681	(0.0, -2.5, 4.3)	1931
Main cargo tank 5	681	(0.0, -5.0, 0.0)	1931
Main cargo tank 6	681	(0.0, -2.5, -4.3)	1931
Main cargo tank 7	681	(0.0, 2.5, -4.3)	1931
Buoyancy tank 1	46	(0.0, -7.5, 2.1)	123
Buoyancy tank 2	46	(0.0, -7.5, -2.1)	123
Buoyancy tank 3	46	(0.0, -5.6, -5.4)	123
Buoyancy tank 4	46	(0.0, -1.9, -7.5)	123
Buoyancy tank 5	46	(0.0, 1.9, -7.5)	123
Buoyancy tank 6	46	(0.0, 5.6, -5.4)	123
Buoyancy tank 7	46	(0.0, 7.5, -2.1)	123
Buoyancy tank 8	46	(0.0, 7.5, 2.1)	123
Fwd bulkhead	147	(50.0, 0.0, 0.0)	-
Aft bulkhead	147	(-50.0, 0.0, 0.0)	-
Fwd compensation tank	100	(65.3, 0.0, 5.0)	800
Aft compensation tank	100	(-65.3, 0.0, 5.0)	800

Mid-body bulkhead 1	10	(25.0, 0.0, 0.0)	-
Mid-body bulkhead 2	10	(-25.0, 0.0, 0.0)	-
Fwd trim tank	35	(67.8, 0.0, 5.0)	200
Aft trim tank	35	(-67.8, 0.0, 5.0)	200
Machinery	1000	(-33.7, 0.0, 6.0)	8288
Permanent ballast	997	(4.0, 0.0, 8.0)	

Table 4.3: SST external hull dimensions (Ma et al., 2021)

Parameter	Free flooding bow compartment	Flooded mid-body	Free flooding aft compartment
Length [m]	23.75	100.0	40.25
Thickness [m]	0.041	0.025	0.041
Steel weight [ton]	521	1374	771
Frame spacing [m]	1.0	1.5	1.0

Table 4.4: Internal tank properties of the SST (Ma et al., 2021)

Tanks	Number of tanks	Length [m]	Diameter [m]	Wall thickness [m]
Auxiliary cargo tank	6	97.5	2.5	0.029
Main cargo tank	7	100	5	0.057
Buoyancy tank	8	100	1.25	0.015
Compensation tank	2	15	8	0.015
Trim tank	2	5	7	0.015

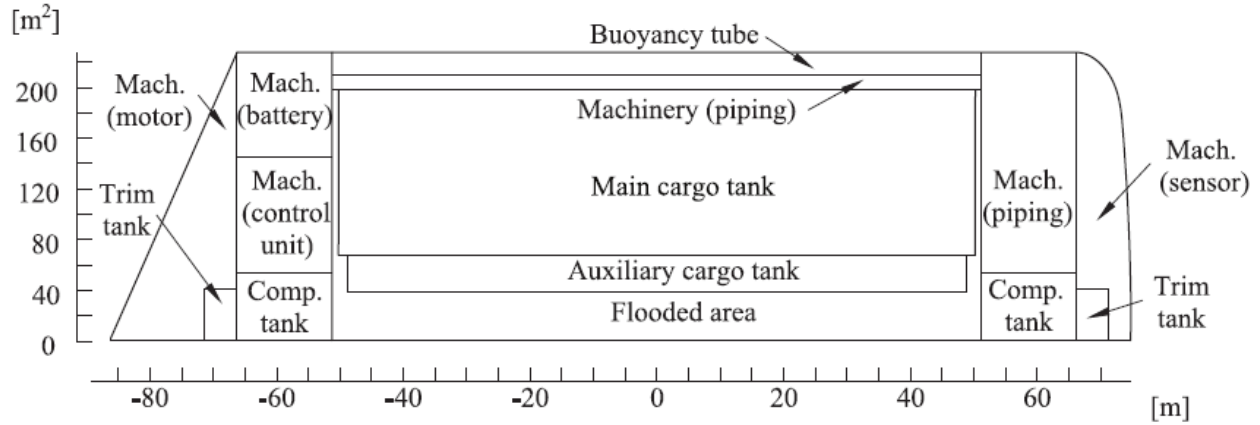


Figure 4.2: Flounder diagram of the SST (Ma et al., 2021)

4.3. Seakeeping model

4.3.1. Coordinate system

The SST's global coordinate system, seakeeping coordinate system, and body-fixed coordinate system are illustrated in Figure 4.3. The earth-fixed or global coordinate system (o_n, x_n, y_n, z_n) is considered an inertial frame of reference. It is also represented as North, East, and down. The seakeeping coordinate system (o_h, x_h, y_h, z_h) follows the SST path and travels at the same velocity as the SST. The wave-induced motion causes the SST to oscillate regarding the seakeeping frame when SST travels at a constant speed (including the zero-speed scenario). Like an earth-fixed coordinate system, a seakeeping reference frame sometimes refers to an inertial frame. The body-fixed coordinate system (o_b, x_b, y_b, z_b) moves relative to the earth-fixed coordinate system and is located at the center of gravity (CoG) of the SST. The vessel's center of gravity (CoG) is located directly below the center of Buoyancy (CoB).

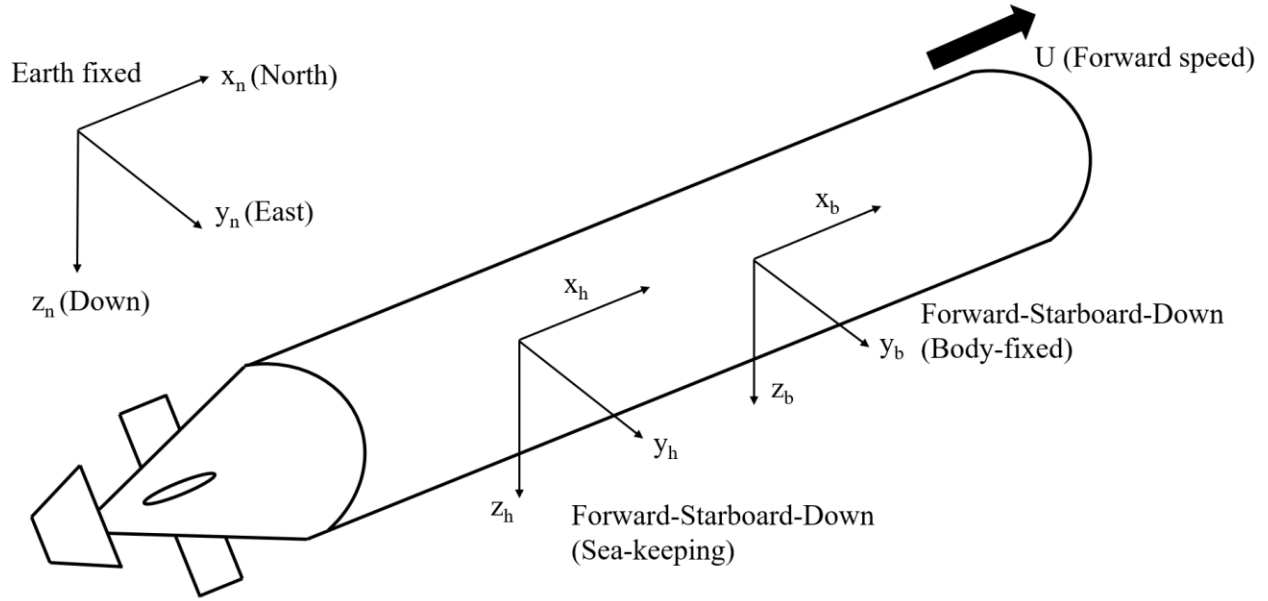


Figure 4.3: SST coordinate SST

4.3.2. Plant model

The SST's equation of motion can be presented as

$$\begin{aligned}
 \text{Inertia forces} & \quad M_{RB}\dot{v} + M_A\dot{v} \\
 \text{Damping forces} & \quad + (D_p + D_v)v_r + \mu_r \\
 \text{Restoring forces} & \quad + G\eta + g_0 \\
 \text{Wave forces} & \quad = \tau_{waves}
 \end{aligned} \tag{4.1}$$

where M_A is the added mass matrix, M_{RB} is the mass matrix, D_p and D_v are the linear potential damping and viscous damping, respectively, $G\eta + g_0$ is the restoring force and ballast force and τ_{waves} is the wave-induced forces (Froude-Krylov (FK) and diffraction forces).

4.3.3. Actuator model

The fore and aft skegs are the primary actuator used on the SST for the bending moment and fatigue analysis. The following section provides some background information on the skegs model.

Skegs

The skegs on the starboard and port sides of the bow and aft are implemented in the model to control the vessel's depth and pitch motion. When the SST has to descend or ascend, two skegs (either bow or aft) turn at the same time to avoid motion coupling (for example, an undesirable roll motion during vessel pitch, for instance). The SST is designed using Bower's airfoil profile (Bowers et al., 2016). The lift force generated by the skeg is expressed as

$$\tau_s = 0.5\rho C_L S_{skeg}(\delta_s - \theta)u^2 \quad (4.2)$$

where C_L is the skeg's lift coefficient ($C_L = 6.1 \text{ rad}^{-1}$), S_{skeg} is the area of skeg ($S_{skeg} = 50 \text{ m}^2$ for bow skeg and $S_{skeg} = 40 \text{ m}^2$ for the aft skeg), ρ is the seawater density ($\rho = 1025 \text{ kg/m}^3$), θ is the angle of attack and δ_s is the skeg angle. For the given study, we assume SST is traveling at the constant water depth, therefore $\delta_s = 0$.

4.4. Simulink implementation

The 2-D planar multibody Simulink model for the SST is developed using the abovementioned mathematical framework, see Figure 4.4. The given model is based on the multibody equation of motion. The bending moment responses are obtained using time-domain simulation under different load cases. The stress time series are later obtained with the aid of bending moment response, which is further used to perform the fatigue assessment of the SST hull.

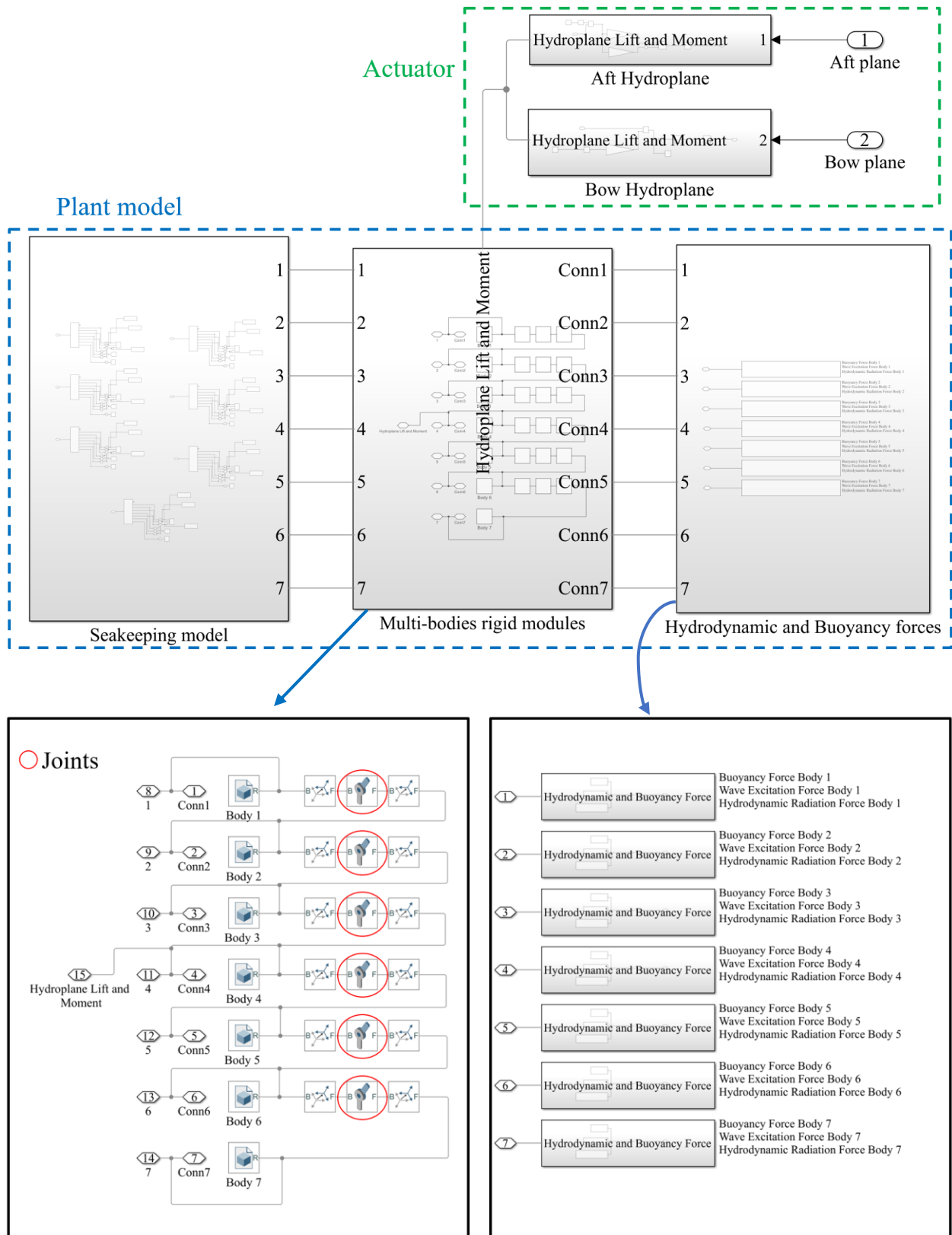


Figure 4.4: SST 2-D planar Simulink model (7 bodies)

The Simulink model is divided into two blocks:

- Plant block: This block is used to describe the SST in the Simulink environment. This block implements all the equations of motion of the SST body. This is accomplished by investigating the hydrodynamic forces (including added mass and damping), the hydrofoil's lift force, and the hydrostatic force of the vessel. The number of plant models is the same as the number of bodies.
- Actuator block: The actuator blocks consist of bow and aft skegs. The actuator block is used to maintain the constant position of the vessel at the given water depth.

Finally, the numerical simulations are performed for the different sea states using Simulink. The main idea is to define the stiffness in joints, see Figure 4.4. The SST should behave exactly like a single rigid body if the connection strength is infinite.

4.5. Control system design – Proportional-Integral-Derivative Controller

Proportional-Integral-Derivative (PID) type Controller is used to transform the open-loop control system of the vessel into a closed-loop control system. It regulates the motion and accomplishes the appropriate performance for the system being evaluated due to its great popularity in marine operation discipline and among autonomous underwater vehicles (AUVs) (Schjøberg & Utne, 2015).

The control loop block layout to keep the vessel at the desired depth/position is illustrated in Figure 4.5. A PID controller receives the error $e(t)$ between the measured and reference values. The closed-loop diagram shows how the actuator influences the PID controller's input u . The input u is multiplied by some correction factors (proportional gain K_P , integral gain K_I and derivative gain K_D) and is fed into the SST plant model to obtain the output y . The control system's performance can be enhanced by carefully tweaking these gains. The PID controller is expressed as

$$u(t) = K_P e(t) + K_I \int_0^t e(t) dt + K_D \frac{de(t)}{dt} \quad (4.3)$$

where K_P , K_I and K_D are the proportional, integral, and derivative gains, respectively and $e(t)$ is the difference between the reference value and the measured value.

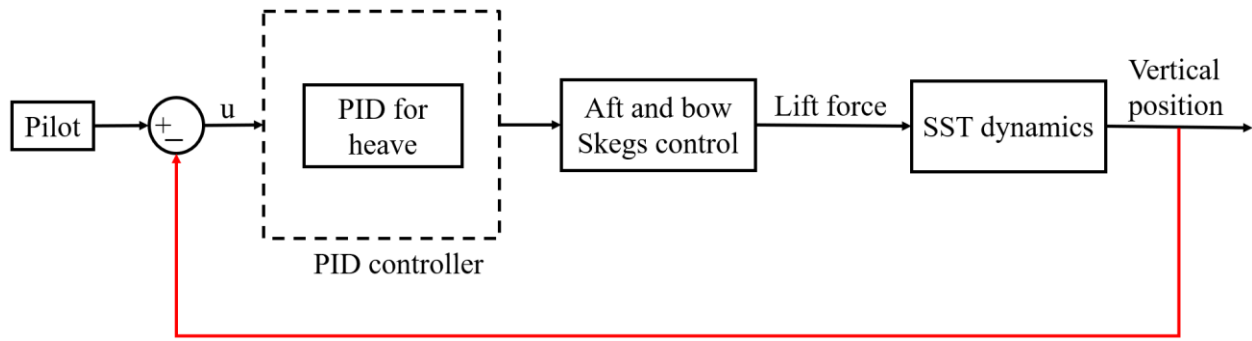


Figure 4.5: SST's control system block

For the bending moment analysis in the thesis, SST should travel at a constant water depth. Therefore, the most critical motion is the heave motion. The $e(t)$ is the error between the measured heave response and the desired heave. The output from the controller controls the bow and aft hydroplane angle to keep the SST at the desired water depth.

Chapter 5 – Bending moment assessment using the multibody approach

In the first phase of the thesis, the bending moment assessment of the SST hull due to wave effect is carried out using the multibody approach. The main focus of this chapter is to present a multibody methodology that can be used as an alternative to the traditional finite element method. The procedure for the analysis is presented in the following way:

- Selecting the load cases for the assessment (H_s and T_p)
- Defining the case study
- Controller tuning
- Convergence study
- Determination of time-domain and power spectral density (PSDs) responses
- Effect of water depth

Many scenarios with various model fidelity, wave characteristics, and operating depths are studied to examine the bending moment's influence.

5.1. Design load cases

Table 5.1 shows the various significant wave heights (H_s) and spectral peak periods (T_p) that are obtained using North Sea hindcast data measured for a period of 10 years (from 2001 to 2010). The three relative load cases are selected to simulate the SST's highly probabilistic operational condition. The Joint North Sea Wave Project (JONSWAP) spectrum is used to model the time-varying irregular waves using the given H_s and T_p values. Each simulation is run for 1 hour.

Table 5.1: Load cases for simulation

Load cases	H_s (m)	T_p (sec)	Wave direction (deg)	Simulation length (sec)
LC1	1.9	11.7	180	3600
LC2	2.5	12.1	180	3600
LC3	3.2	12.7	180	3600

5.2. Case studies

The SST hull is divided into three, five, seven and nine rigid modules to analyze the influence of model fidelity and above load conditions on the bending moment. Ma et al., (2021) presented the depth definition for the SST. The depth definition is as follows: safety depth (40 m), nominal diving depth (70 m) and test diving depth (105 m). Based on the given depth definition, the operating depth range for the vessel is between 40 m and 70 m. When the baseline design was proposed by Ma et al., (2021), it is mentioned that it travels at the nominal water depth of 70 m at the slow speed of 6 knots for maximum energy efficiency.

Using the multibody approach, considering the model fidelity, depth definition and operating speed, various case studies are presented to perform the bending moment assessment on the SST hull. The torpedo shape of the SST consists of a hemispherical bowl with a radius of 8.5 m at the fore, a cylindrical mid-body section 130.5 m long, and a conical aft section of 25 m long (Ma et al., 2021). This makes a relatively simple geometry for the vessel. Because of the simple geometry shape, the author of the thesis decided to use the hull's simplified cylindrical shape when performing the convergence study to decide the minimum number of bodies/modules required. The different case studies are presented in Table 5.2.

Table 5.2: A case study for the bending moment assessment

Case study	Hull geometry	No. of bodies	Operating depth (m)	Operating speed (knots)	Controller type
cyl-3-70-6-tu	Simplified cylindrical hull	Three	70	6	Tuned
cyl-5-70-6-tu		Five	70	6	Tuned
cyl-7-70-6-tu		Seven	70	6	Tuned
cyl-9-70-6-tu		Nine	70	6	Tuned
tor-7-40-6-tu	Torpedo	Seven	40	6	Tuned
tor-7-70-6-tu	shape hull	Seven	70	6	Tuned

5.3. PID controller tuning

The PID controller is tuned using the Matlab transfer function-based PID tuner app. The fundamental tuning idea for the chosen PID controller is given by Åström et al., (2006). The system model linearization is applied at an operational point to tune the PID controller. By modifying the phase margin settings and frequency domain's bandwidth, the tuner will automatically compute the appropriate controller gains and map out the system impulse response. The most optimal PID controller gains for the cases mentioned above are given in Table 5.3.

It is important to note that the main focus of the study is on the multibody concept rather than the PID controller tuning.

Table 5.3:PID controller gains

Hull geometry	No. of bodies	K_P	K_I	K_D
Simplified cylindrical hull	Three	-4.62	-1.5×10^{-4}	-97.63
	Five	-3.44	-1.4×10^{-4}	-115.17
	Seven	-6.14	-1.5×10^{-4}	-200.57
	Nine	-5.92	-1.4×10^{-4}	-137.98
Torpedo shape hull	Seven	-0.404	-6.820×10^{-4}	-59.418

5.4. Convergence study

A full-fledged convergence study is carried out on the simplified cylindrical hull geometry. The main aim of this study is to determine the minimum number of bodies required for performing a bending moment assessment. The hydrodynamic forces, which consist of excitation force and radiation force, are applied to the center of each body. The response of each body can be obtained by solving the multibody equation of motion, see Eq. 2.28. The number of bodies determines the accuracy of the results: the more bodies, the more reliable and accurate the bending moment results for the SST hull.

For the convergence study, the bending moment results for the three, five, seven and nine bodies are compared and plotted against each other at different longitudinal locations on the hull. The simulation is carried out in regular wave conditions with the wave amplitude and wave period set to 1 m and 10 secs. The results are obtained for the 70 m water depth, and the optimal gains are used to tune the PID controller. The convergence study results are illustrated in Figure 5.1. The bending moment response for the five, seven and nine bodies at a different longitudinal location are very close to each, while the three-body SST underestimates the bending moment. One reason could be that the three bodies might not have enough points to capture all the wave encounter frequencies.

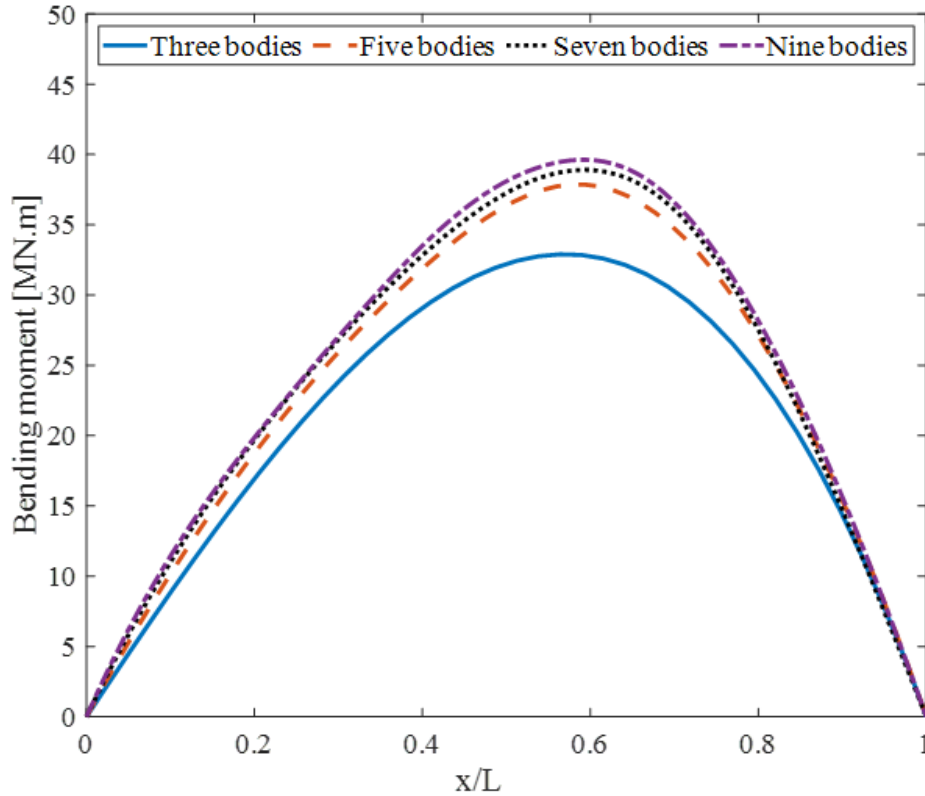


Figure 5.1: Bending moment convergence study (Regular waves: $H = 1$ m and $T = 10$ secs)

Figure 5.2 shows the comparison of the heave and pitch response for the different bodies in the regular wave condition with the wave amplitude of 1 m and wave period of 10 secs. The time series responses of the heave and pitch at the 70 m water depth are used for the comparison. It can be seen from the results that the heave response for three, five, seven and nine bodies are almost 0 m, which means the controller is very efficient and effective in maintaining the depth. On the other hand, some small oscillations are observed in the pitch response with different frequencies. These minor irregularities or peaks might be caused by small oscillating frequencies in joints while connecting two bodies in Matlab Simulink.

To further determine the ideal number of bodies among the five, seven and nine, the bending moment responses at three particular time instances (i.e. at 520 secs, 525 secs and 530 secs) are determined and plotted, see Figure 5.3. The simulation conditions (i.e. regular waves, water depth and controller gains) are the same as mentioned above.

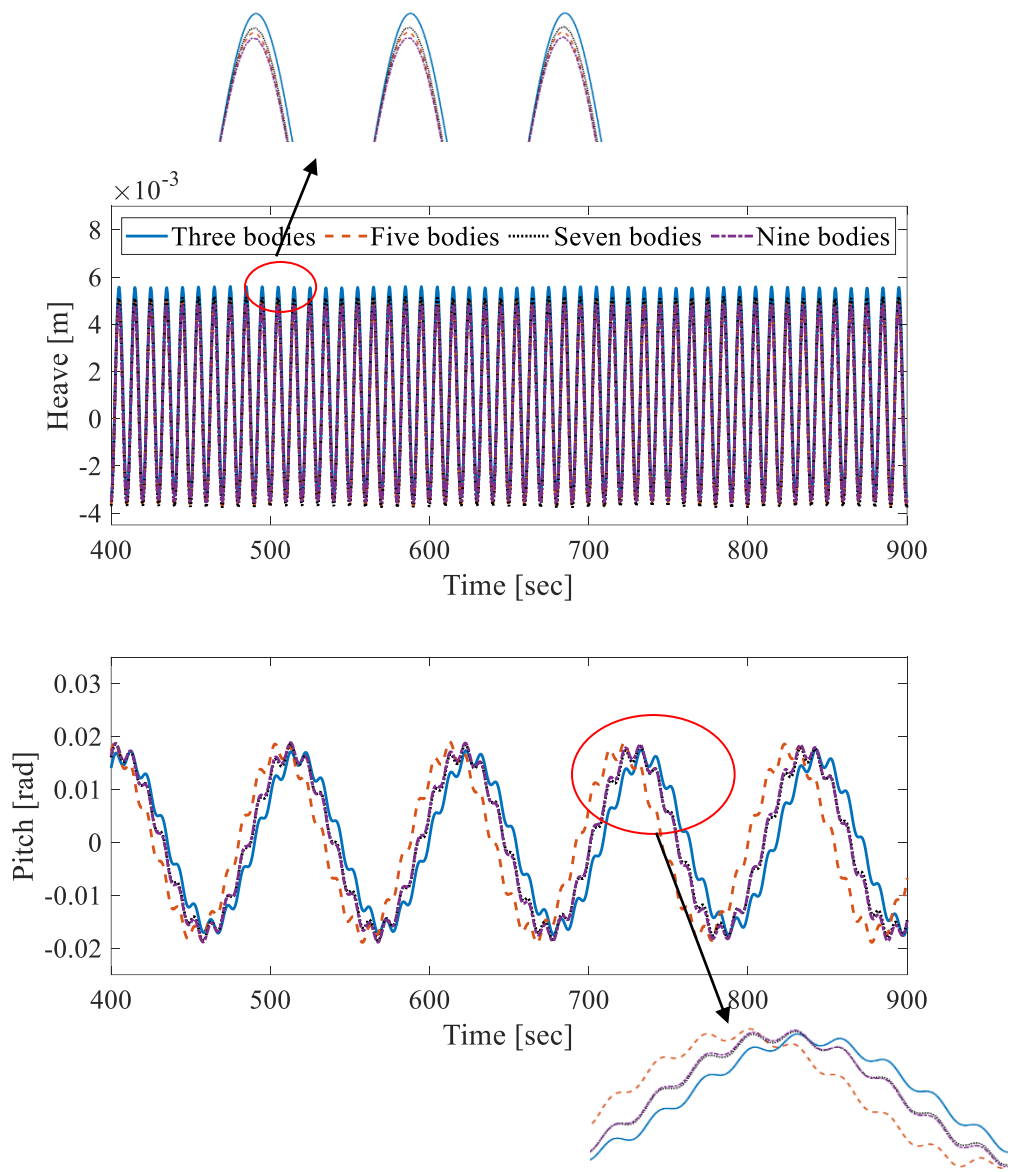


Figure 5.2: Time series response of heave and pitch for different numbers of bodies (Regular waves: $H = 1$ m and $T = 10$ secs)

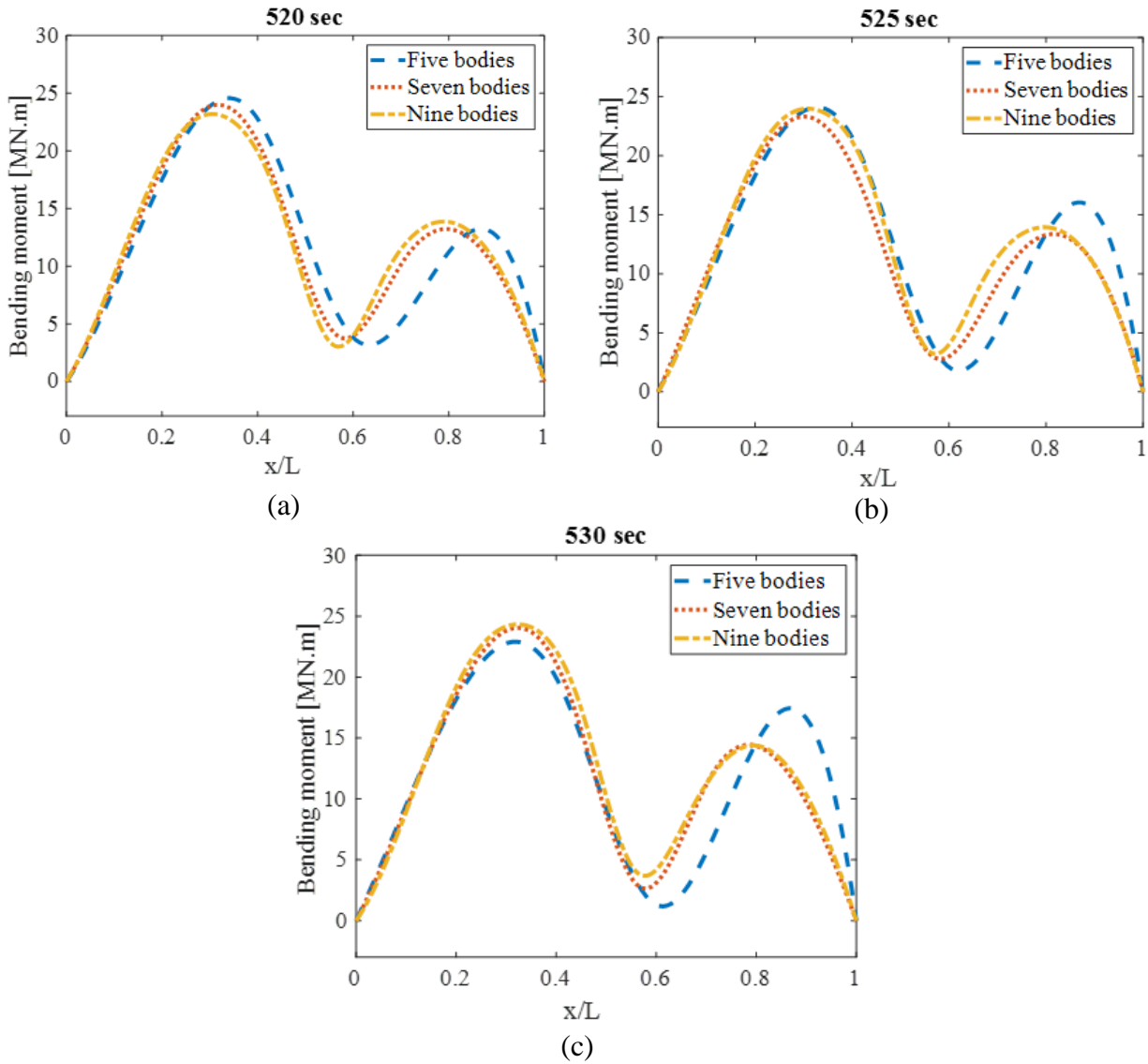


Figure 5.3: Bending moment response at (a) 520 secs, (b) 525 secs and (c) 530 secs

Figure 5.3 illustrates that the bending moment response at three different time instances fits very well for seven and nine bodies. In contrast, for five bodies, the responses vary greatly. An explanation given earlier for the three-body SST can also be applied on five bodies, i.e. five bodies might not be enough to capture all the wave encounter frequencies.

After performing a convergence study, the author of the thesis decided to use seven bodies to present further results. All the further results in this chapter and the following chapters of this thesis are presented for the seven-body actual torpedo-shape SST hull.

5.5. Time-domain and power spectral density response

Figure 5.4. illustrates the time-domain bending moment response at the different longitudinal locations for the seven-body torpedo-shape SST. The time-series response is obtained for the LC1 load case. The power spectral density response of the same for all the load cases is presented in Figure 5.5. All the simulation is performed at 70 m water depth.

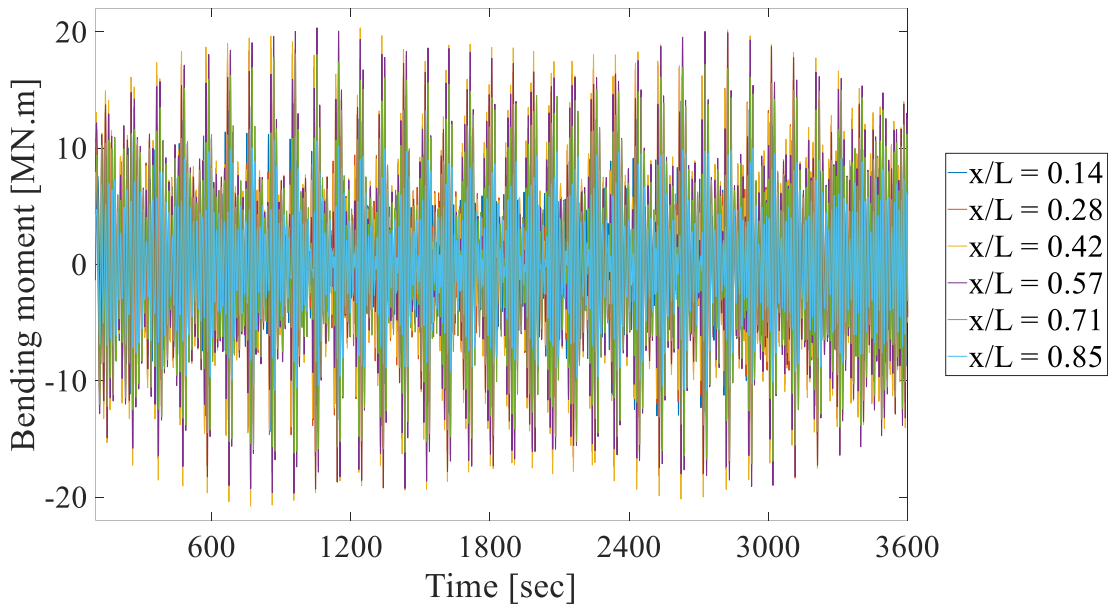
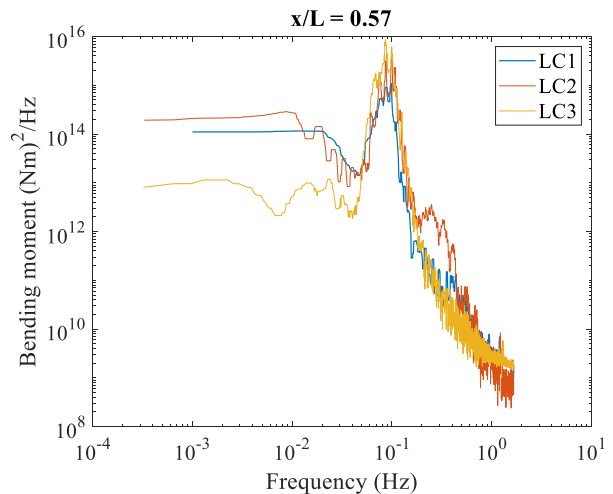
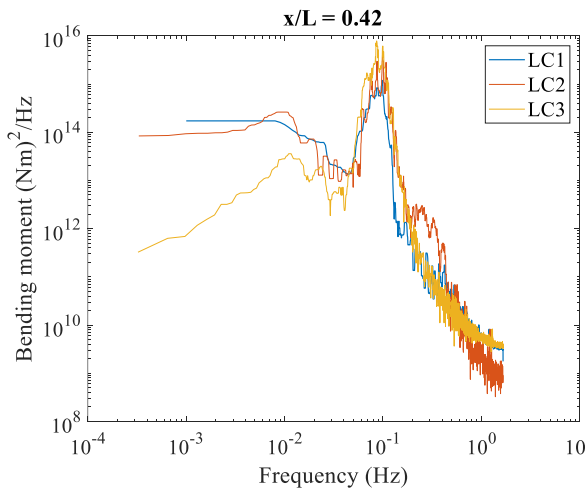
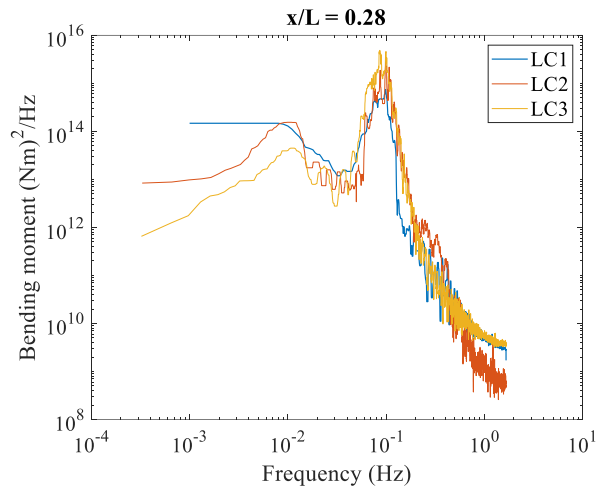
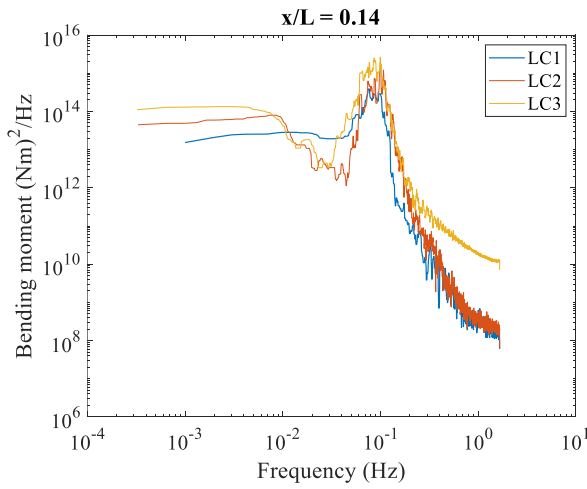


Figure 5.4: Time series response (LC1 load case)

It can be concluded from the result that the dynamic part of the bending moment response is crucial since the static bending moment response is significantly small. This is due to the wave-induced pitch excitation moment, which has high oscillations but a lower mean value, dominating the bending moment effect on the multibody SST hull. Table 5.4 shows a statistical overview of the bending moment for the various load case scenarios. Since both ends of the multibody SST are free, the bending moment at $x/L = 0$ and $x/L = 1$ is zero.

Table 5.4: Statistical summary for bending moment for LC1, LC2 and LC3 load cases

x/L	Mean value, LC1 (MNm)	Mean value, LC2 (MNm)	Mean value, LC3 (MNm)	Standard deviation, LC1 (MNm)	Standard deviation, LC2 (MNm)	Standard deviation, LC3 (MNm)
0.14	0.0421	0.116	0.184	5.35	7.76	11.46
0.28	0.0722	0.132	0.254	7.12	10.18	13.7
0.42	0.0643	0.143	0.231	8.18	11.91	16.11
0.57	0.0478	0.165	0.187	7.96	11.70	15.79
0.71	0.0286	0.164	0.128	6.77	9.88	13.25
0.85	0.0147	0.0725	0.081	4.10	5.90	7.8



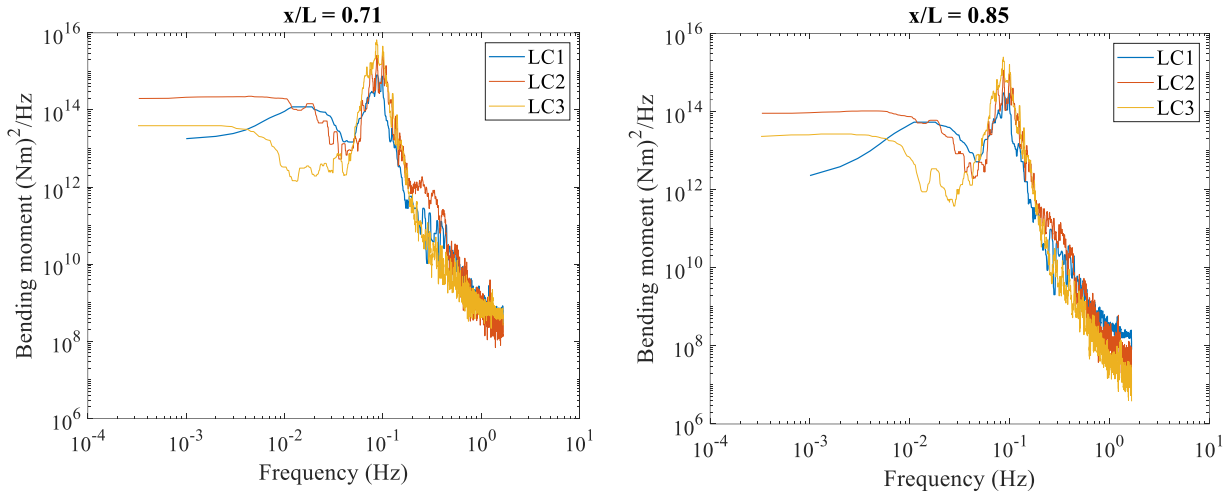


Figure 5.5: Power spectral density at different location for LC1, LC2 and LC3 load cases

The power spectral density (PSD) distribution shows the multibody SST's dynamic properties. Because the multibody SST hull is predominantly exposed to hydrodynamic forces and moments, waves are the main excitation source. Low-frequency waves are primarily responsible for the dynamic bending moment response of the multibody SST. A strong grasp of dynamic behaviour is also required to enhance the vessel's design and obtain extreme values.

5.6. Effect of water depth

The operating range for the SST is between 40 m and 70 m. Therefore, it is necessary to quantify the effect of bending moment at 40 m water depth to better understand the wave effect. The simulation is performed for all load cases. The statistical results for the 40 m water depth are compared to those obtained for the 70 m water depth. It is found that the standard deviation for the 40 m water depth is approximately 0 to 50% higher than the 70 m water depth. This can greatly impact the SST hull's structural performance and cause a higher amount of fatigue damage at 40 m water depth. Table 5.5 shows the statistical comparison of the bending moment for the LC1 load case at 40 m and 70 m water depths.

Table 5.5: Statistical comparison for bending moment for LC1, LC2 and LC3 at 40 m and 70 m water depth

x/L	Mean value, 40 m depth (MNm)	Mean value, 70 m depth (MNm)	Standard deviation, 40 m depth (MNm)	Standard deviation, 70 m depth (MNm)
LC1				
0.14	0.0584	0.0421	6.09	5.35
0.28	0.111	0.0722	8.39	7.12
0.42	0.117	0.0643	8.21	8.18
0.57	0.0708	0.0478	7.25	7.96
0.71	0.0280	0.0286	6.84	6.77
0.85	0.0253	0.0147	5.00	4.10
LC2				
0.14	0.0367	0.116	10.04	7.76
0.28	0.142	0.132	11.26	10.18
0.42	0.359	0.143	12.22	11.91
0.57	0.451	0.165	11.60	11.70
0.71	0.180	0.164	10.13	9.88
0.85	0.0604	0.0725	6.60	5.90
LC3				
0.14	0.176	0.184	14.21	11.46
0.28	0.243	0.254	17.67	13.7
0.42	0.269	0.231	24.59	16.11
0.57	0.206	0.187	23.20	15.79
0.71	0.144	0.128	20.14	13.25
0.85	0.109	0.081	12.96	7.8

Chapter 6 – Fatigue assessment of the Subsea Shuttle Tanker hull

Fatigue damage is a gradual localized plastic deformation process in a material subjected to fluctuating or cyclic loads and strain at high-stress concentration regions. This can lead to cracks or complete fractures after a certain number of fluctuations. This type of stress is known as "fatigue stress," and it is substantially lower than yield or tensile stress (Xin, 2013). SST undergoes an oscillatory motion because of unpredictable waves, currents, and vessel motion in the offshore environment, as discussed in Chapter 5. This is the main cause of fatigue damage. The fatigue data on these offshore structures generally exhibits statistical variations due to the high cycle fatigue (HCF) conditions placed on them, see Figure 6.1.

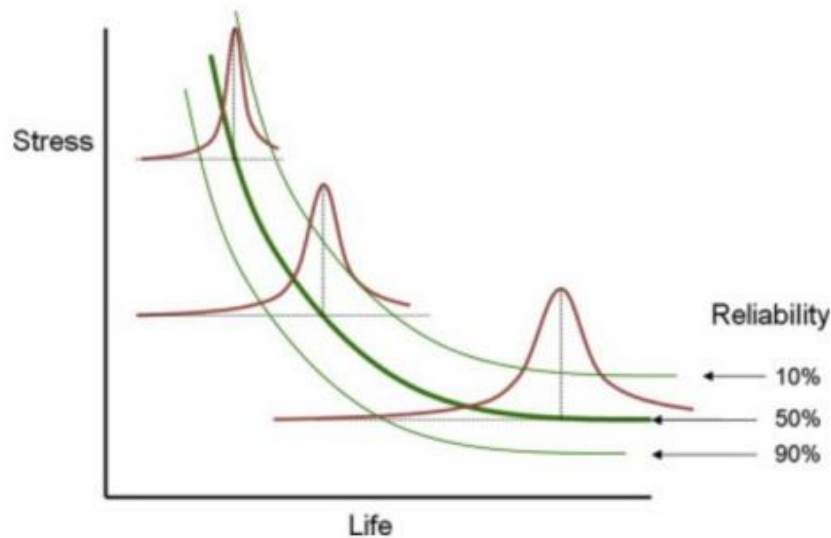


Figure 6.1: Statistical behaviour of fatigue life (Xin, 2013)

The preliminary study conducted by the author shows that the dynamic pressure between 40-70 m water depth is around 3-6 % of the hydrostatic pressure. Even though dynamic pressure is very low compared to hydrostatic pressure contribution, it is necessary to quantify and justify the damage while investigating the structural performance of the SST hull, as fatigue is nothing but the sum of damages.

6.1. Fatigue analysis methodology

Typically, the fatigue assessment consists of three major steps. First, the determination of stresses caused by the cyclic loading induced by the waves. The stress time series can be derived using the bending moment values obtained in Chapter 5. Second, Local stresses in structural details (i.e. stiffener welds) are determined using the stress concentration factor (SCF). Little variation in the SCF can cause a significant difference in the fatigue damage outcome and life prediction. Third, the "Rainflow counting" method to determine the stress cycles and stress range. Finally, the accumulated damage is determined using the "Palmgren-Miner" rule (Sen, 2006). A detailed explanation of the "Rainflow counting" method and "Palmgren-Miner" rule is given in Chapter-2 section 2.5.2, 2.5.3, 2.6.3.

The inverse of fatigue damage gives the fatigue life. Because of the various uncertainty involved, the fatigue life process is quite difficult. These key uncertainties are as below (Sen, 2006):

- The statistical scatter is applied to the S-N curves (i.e., the component's life varies even when subjected to the same load history).
- SST hull thickness is not uniform.
- Uncertainty associated with the Miner's rule.
- Eccentricity during the manufacturing and fabrication process.
- Uncertainty associated with the hindcast data.
- Uncertainty associated with the numerical modelling.
- Uncertainty in SCF calculation for the local details.

6.2. Overview of local stress calculation

Because of the influence of the geometric change, the structural stress differs from the nominal stress in places with structural discontinuities. It is frequently associated with geometric or hotspot stress in the fatigue assessment. The notch stress is the overall stress at the root, including local effects due to the weld toe and stress increase owing to the weld geometry and connections, see Figure 6.2 (DNV, 2010b).

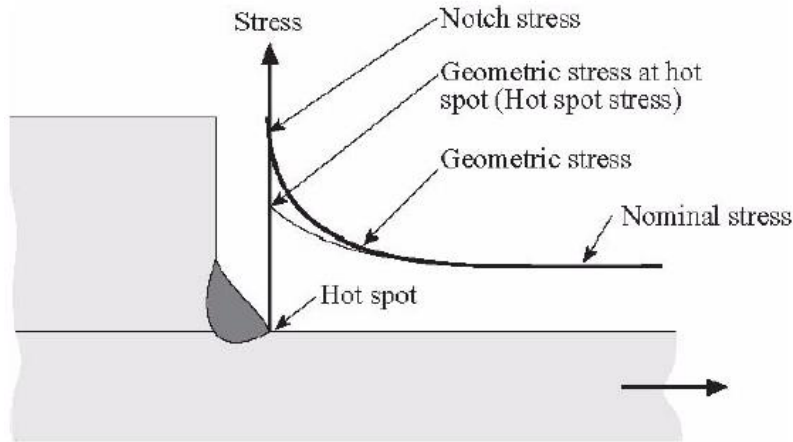


Figure 6.2: Definition of different stresses (DNV, 2010b)

The increase in the stress in the local details is normally expected to be proportional to the nominal stress. The geometric stress at the hot spot is calculated as nominal stress times stress concentration factor (SCF). When calculating SCF, it is common practice to compute the nominal and local structure stress using basic recommendations. The SCF is given by:

$$SCF = \frac{\sigma_l}{\sigma_n} \quad (6.1)$$

where σ_l is the geometric stress at the hot spot, which is generally obtained using finite element (FE) analysis and σ_n is the nominal stress calculated using either global FE analysis or beam theory. The change in relative stiffness of the local structure affects the SCF. The SCF computation often requires just the local structural detail (DNV, 2010b).

6.3. FEA modelling of local detail

This section provides the detail and step-by-step explanation of the FEA modelling of local weld details at Stiffeners.

6.3.1. Analysis model

The finite element model of the mid-body section of the SST is created using Ansys mechanical workbench 2020R1. The layout of the mid-body section and the circumferential stiffeners supporting the external hull is presented in Figure 6.3. The effective cross-section of the stiffeners and the stiffener properties are presented in Figure 6.4 and Table 6.1, respectively.

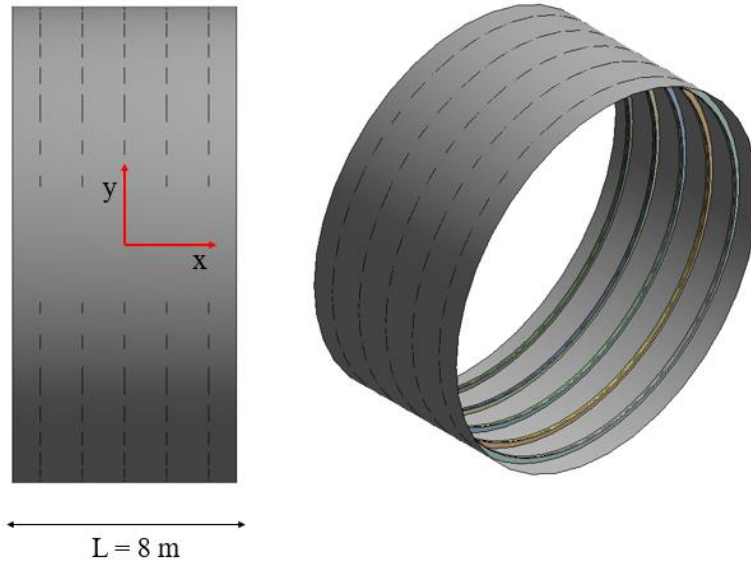
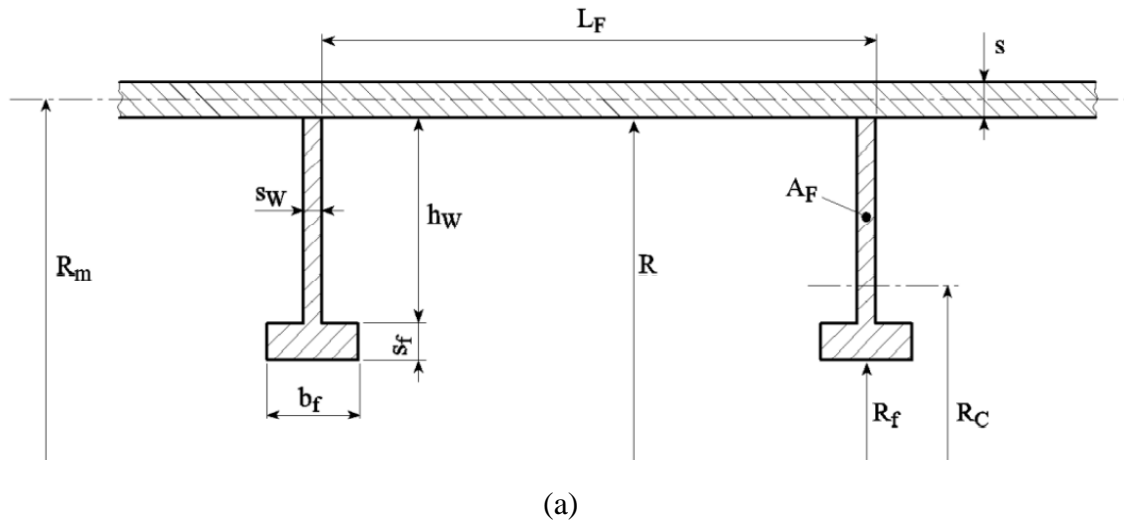


Figure 6.3: The 3-D model of the mid-body section



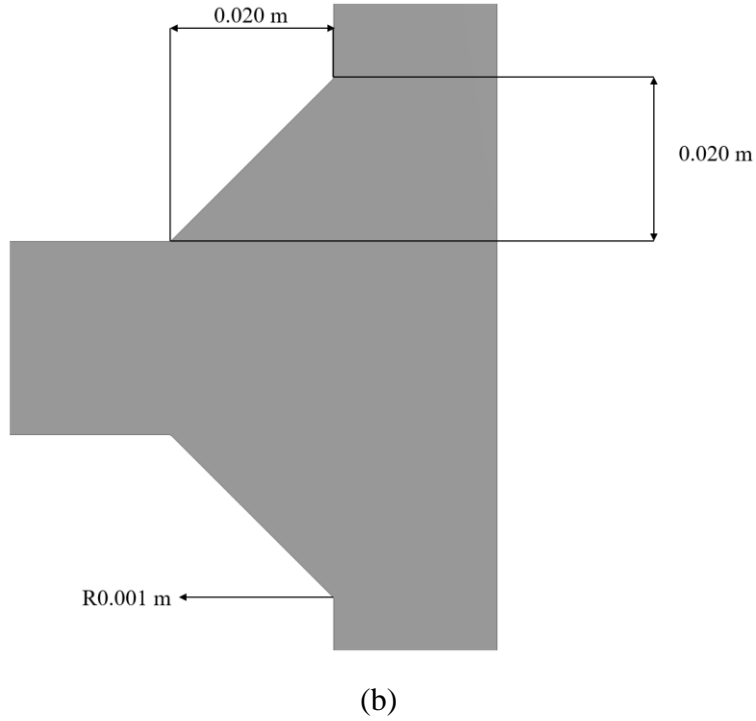


Figure 6.4: (a) Cross-section of the external hull stiffener (DNV, 2018); (b) Weld details

Table 6.1: Properties of stiffeners (Ma et al., 2021)

Parameter	Free flooding compartment	Flooded compartment
Frame web height, h_w	0.300 m	0.300 m
Frame web thickness, s_w	0.030 m	0.030 m
Flange width, b_f	0.100 m	0.100 m
Flange thickness, s_f	0.033 m	0.033 m
Frame spacing, L_F	1 m	1.5 m
Frame cross-sectional area, A_F	0.012 m ²	0.012 m ²
Inner radius to the flange of the frame, R_f	6.138 m	6.138 m

Two different types of loading: external pressure and bending moment, are acting on the external hull of the SST. The external pressure problem is modelled in 2D for an axisymmetric analysis

because of their symmetric geometry and loading. This will lower the number of elements and greatly reducing computational time. The bending moment problem is modelled as a shell element.

6.3.2. Material properties

The local detail model used in this study uses linear elastic analysis to calculate the stress concentration factor. Table 6.2 shows the material properties applied in the linear FE analysis for cylindrical shells and stiffeners. The material properties of cylindrical shell and stiffeners are the same.

Table 6.2: Material properties of the SST section (Ma et al., 2021)

Material	VL-D47
Young's modulus	206 GPa
Yield strength	460 MPa
Tensile strength	550 MPa
Poisson's ratio	0.3

6.3.3. Mesh details

The element types used for this study are quadrilateral for both 2D axisymmetric and 3D analysis. In the critical locations of interest, triangular and tetrahedral elements are avoided because they are comparably stiffer and do not capture bending accurately unless the mesh is extremely fine (Skotny, 2019). Second-order elements are used at the hot spot near the welds to capture realistic deformation.

The Linear elements can be used in the area of less interest, provided the mesh quality, accuracy and model stiffness in the geometric representation are taken care of. Table 6.3 represents the element types used for this study's analyses. It is very important to examine mesh for convergence using the mesh convergence criteria specified in DNV-RP-F112, regardless of the type of elements, size and order (DNV, 2019).

Table 6.3: Summary of elements type

Model	Mesh area	ANSYS terminology	Element type
2D	Entire model	PLANE 183	2D 8-node plane (second order)
3D	Entire model	SHELL 181	3D 4-node shell (second order)

6.3.4. Mesh convergence study

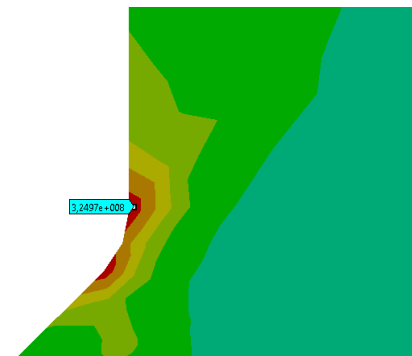
If the mesh convergence of a FE analysis is not verified properly, the results cannot be regarded as reliable. The mesh size influences the results of an FEA. Therefore, it is crucial to refine the mesh to the point where further refinement won't significantly alter the results and converge to a solution.

Figure 6.5 illustrates a mesh convergence study for the 2D axisymmetric model at the weld toe. This study analyzes four different mesh sizes on the weld toe, starting with coarse, intermediate, fine and very fine mesh refinement. It should be noted that even though an all-quad-free face mesh type was applied, very few triangles were created during meshing.

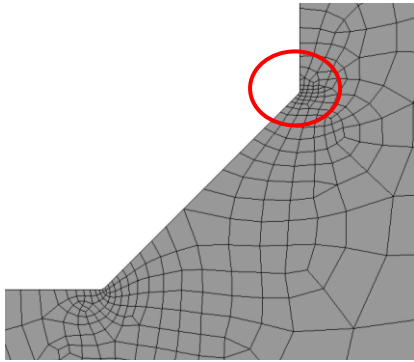
Coarse mesh refinement



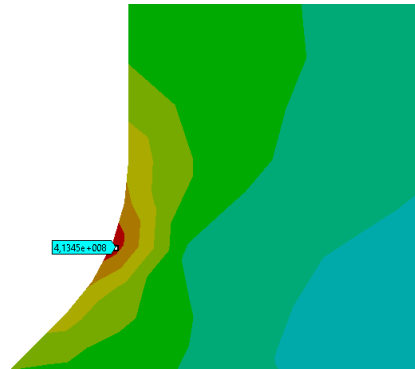
$$\sigma_{eq\ max} = 325.7\ MPa$$



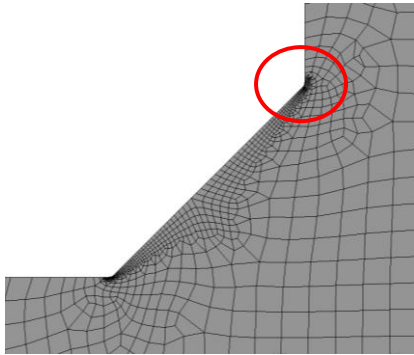
Intermediate mesh refinement



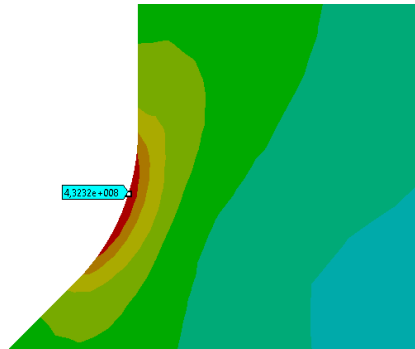
$$\sigma_{eq\ max} = 413.4\ MPa$$



Fine mesh refinement



$$\sigma_{eq\ max} = 432.3\ MPa$$



Very-fine mesh refinement



$$\sigma_{eq\ max} = 433.2\ MPa$$

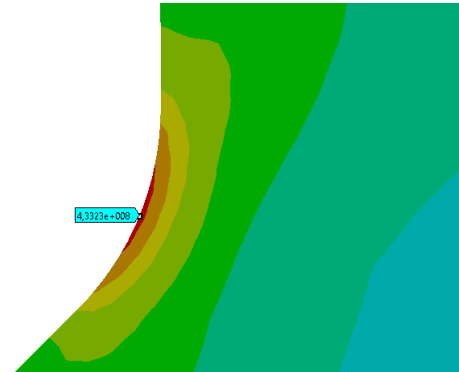


Figure 6.5: Mesh convergence study for 2D axisymmetry model - Mesh refinement model and corresponding max. equivalent stress at welds

The maximum equivalent stress is obtained and plotted for four different mesh refinements at the weld toe. According to the DNV-RP-F112 (DNV, 2019), the convergence error for linear analysis should be less than 3%. Figure 6.6 shows that the maximum equivalent stress at the weld toe converges at a very fine mesh for the 2D axisymmetry model. Figure 6.7 shows that maximum equivalent stress at the welds converges at the fine mesh for the 3D model. Because the mesh has

already converged at the very fine mesh and fine mesh for the 2D and 3D models, respectively, the results of any subsequent mesh refinement are legitimate according to the mesh convergence criterion. Therefore, fine mesh refinement is used to obtain the SCF for both the models.

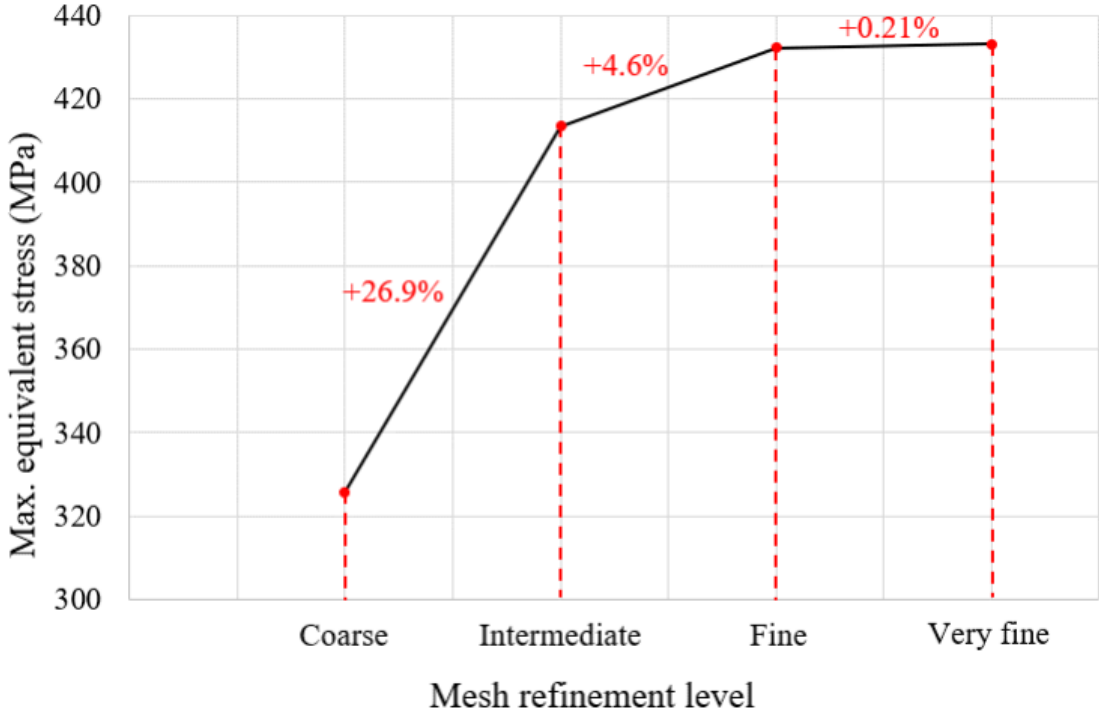


Figure 6.6: Plot of mesh convergence study of 2D axisymmetric model

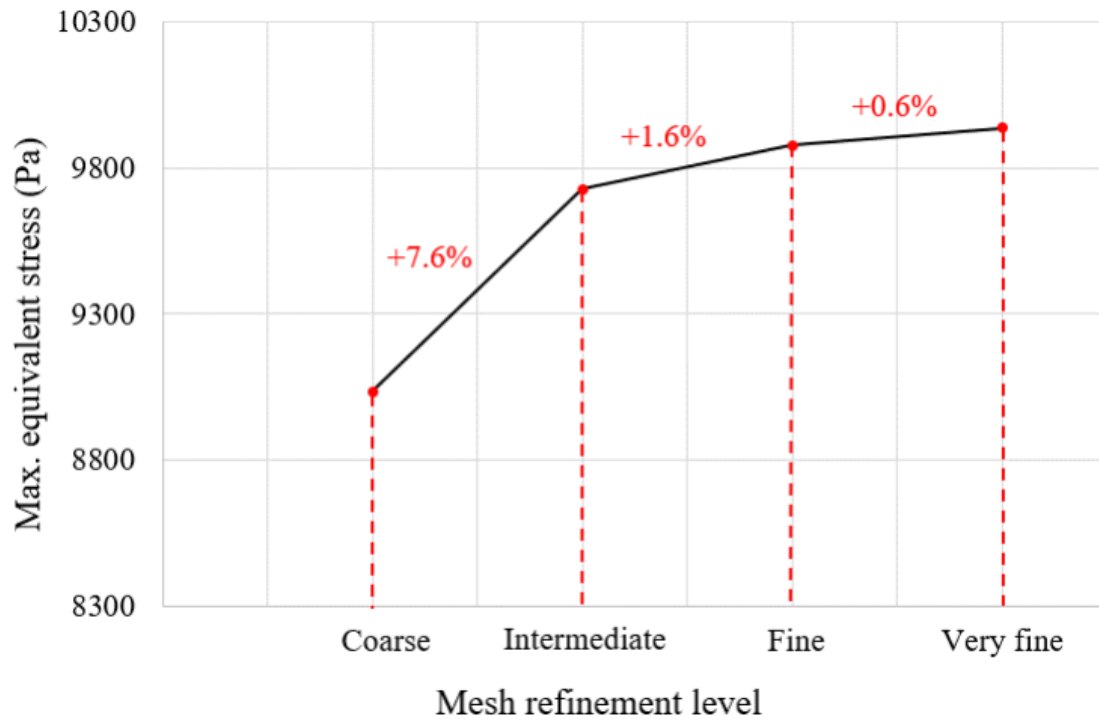


Figure 6.7: Plot of mesh convergence study of 3D model



Figure 6.8: 3D ANSYS model showing fine mesh

6.3.5. Loads and boundary conditions

Figure 6.9 illustrates the load and boundary conditions and the selected direction for the imposed action. For this study, the 2D model is loaded with external pressure (A, on the left figure) of 7.04 bar on the cylindrical shell's outer surface, and the shell model is loaded with the bending moment (A, on the right model) of 50000 Nm about z-axis on the free end. Another end of the model is rigidly fixed (B).

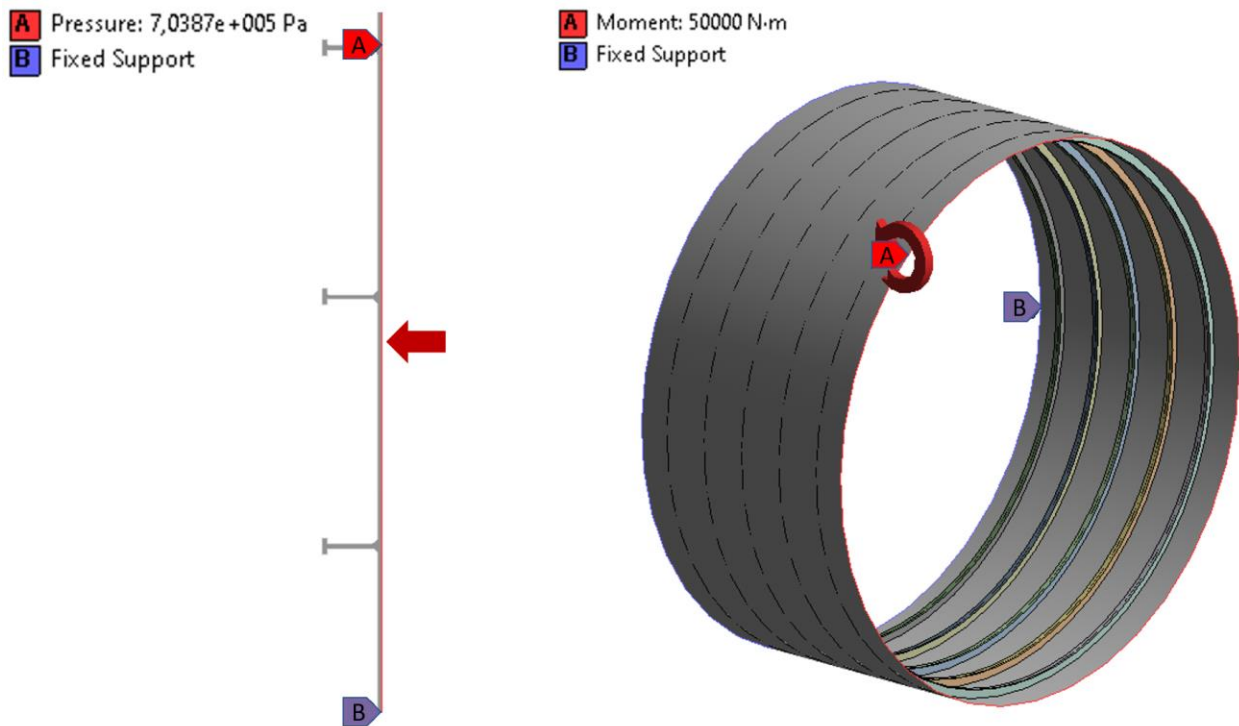


Figure 6.9: Load and boundary condition for 2D axisymmetric model (Left) and shell model (Right)

6.3.6. FE analysis results: SCF

The models are subjected to different loadings (i.e. external pressure and bending moment) to compute the stress concentration factor in the details. It was anticipated that any effects from the boundary conditions are assumed to be insignificant enough to be ignored because the main focus of the study is the local weld details at the stiffeners. The two different models (2D and 3D) of the

sub-structure are shown in Figure 6.10. All the quadrilateral elements use a 4-node shell element for the 3D model and an 8-node plane element for the 2D axisymmetric model, and the local maximum stress is determined at the welds. The stress concentration factor at the local detail is found using Eq. (6.1) and shown in Table 6.4.

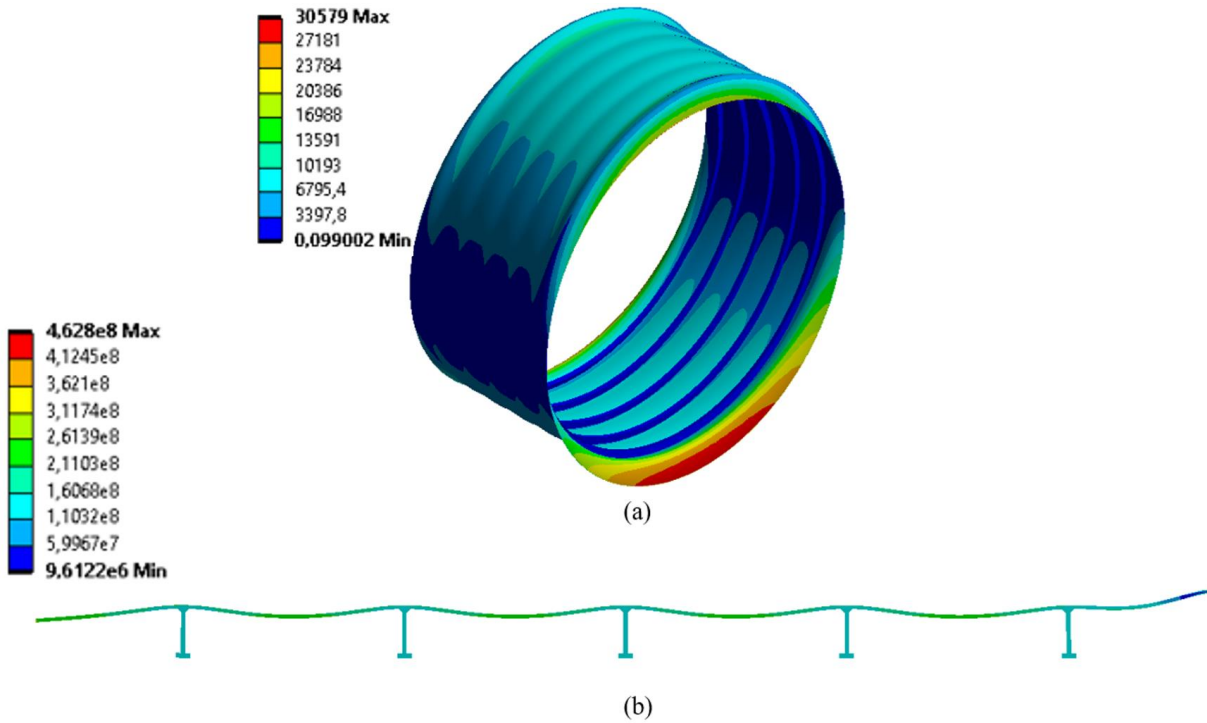


Figure 6.10: Equivalent stress plot: 3D model loaded with bending moment (a) and 2D axisymmetry model loaded with external pressure (b)

Table 6.4: SCF calculated using ANSYS for different models and different loadings

Applied load	SCF
External pressure	1.81
Bending moment	1.24

Furthermore, the 3D surface model will be unable to capture the weld's local detail very efficiently and will underestimate the weld's local stresses. The 2D model can provide the actual

representation of the welds, but only axisymmetric loading can be analyzed. Therefore, finding the method of evaluating SCF accurately at the local weld details is necessary.

One way is to create a 3D solid model of the sub-section to represent the local weld details, but this is not considered the most appropriate way because of the computational efforts. Another approach can be to model the weld as a solid element, and the rest of the geometry can be modelled as a shell. This will require a precise meshing approach to connect two different element types. Many studies have examined and linked the key factors encountered in evaluating SCF at the local details (Peterson, 1953). These factors include various types of loads, physical parameters, stress raisers, and material susceptibility.

However, some studies have considered the SCF resulting from the superposition of the discontinuities (Paul Jr & Faucett, 1962). Paul Jr & Faucett, (1962) proposed a methodology for integrating the two different SCF determined from two stress raisers (i.e. notch). They showed that when the two stress raisers are superposed, the resulting SCF will depend on the SCF from stress raiser 1 and SCF from stress raiser 2. The resulting SCF can be determined by taking the product of the SCF for the individual notches.

$$SCF_{sup} = SCF_1 \times SCF_2 \quad (6.2)$$

where SCF_{sup} is the resultant stress concentration factor for the superposed geometry, SCF_1 and SCF_2 is the individual stress concentration factor derived from two different geometry notches. Mowbray Jr, (1950) investigated the same problem experimentally with strain gages and proposed that SCF_{sup_exp} was slightly less than the product of the SCF_1 and SCF_2 .

$$SCF_{sup_exp} \leq SCF_1 \times SCF_2 \quad (6.3)$$

Based on Eq. (6.2), the resultant SCF, which is used for determining the fatigue damage of the SST hull, can be determined by the product of individual SCF corresponding to external pressure and bending moment. A conservative approach like the one mentioned above is reasonable to use for the subsea autonomous vehicle like SST. The detailed information regarding the current approach can be found in (Paul Jr & Faucett, 1962; Vicentini, 1967).

Table 6.5: Resultant SCF from combined external pressure and bending

SCF_{res}	$1.81 \times 1.24 = 2.24$
-------------	---------------------------

6.4. Wave-induced fatigue

The operational depth of the SST mainly governs wave-induced fatigue. The operational depth of 40 m and 70 m is used for the fatigue assessment. DNV-RP-C203 (DNV, 2010a) is the recommended practice for the fatigue assessment on the SST hull. The study approach is based on S-N curves. The S-N curves in DNV-RP-C203 (DNV, 2010a) are based on the mean-minus-two standard deviation obtained from the specimens' laboratory fatigue testing. The S-N curves have a 97.7% chance of surviving during the design life.

The basic design S-N curve is represented as (DNV, 2010a)

$$\log N = \log \bar{a} - m \cdot \log (\Delta \sigma) \quad (6.4)$$

where N is the number of cycles to failure for the stress range $\Delta \sigma$, $\log \bar{a}$ is the intercept of $\log N$ axis by the S-N curve (see Eq. (6.3)), m is the slope of the S-N curve, and $\Delta \sigma$ is the stress range in MPa (see Eq. (6.5)).

$$\Delta \sigma = \Delta \sigma_0 \cdot SCF \left(\frac{t}{t_{ref}} \right)^k \quad (6.5)$$

where $\Delta \sigma_0$ is the nominal stress range, SCF is the stress concentration factor, t_{ref} reference wall thickness for welded connection (DNV, 2010a), t is the wall thickness of the SST, k is the thickness exponent on fatigue strength.

$$\log \bar{a} = \log a - 2 \cdot S_{\log N} \quad (6.6)$$

where $\log a$ is the intercept of the mean S-N curve with the $\log N$ axis and $S_{\log N}$ is the standard deviation of $\log N$.

For the fatigue assessment on the SST hull, the S-N curves derived from fatigue experiments and approved by the DNV-GL class guidelines are used (DNV, 2015). The chosen S-N curve is suitable for both normal and high-strength steel. The hot spot C2 curve is used together with stress data to show the welded details. A thickness effect and additional stress concentration may be necessary to portray true welds details accurately, but this thesis does not consider it. The S-N curve corresponding to C2 is presented in Figure 6.11.

Table 6.6: S-N curve parameters for C1

S-N Curve	Material	$N \leq 10^7$		$N \geq 10^7$	
		$\log \bar{a}$	m	$\log \bar{a}$	m
C2	Welded joint	13.301	3.5	16.902	5.5

Many researchers (Gaidai et al., 2020; Gemilang & Karunakaran, 2017; Legras et al., 2013; Orimolade et al., 2015) have demonstrated that these curves are helpful for the efficient fatigue assessment of the various structures in offshore conditions.

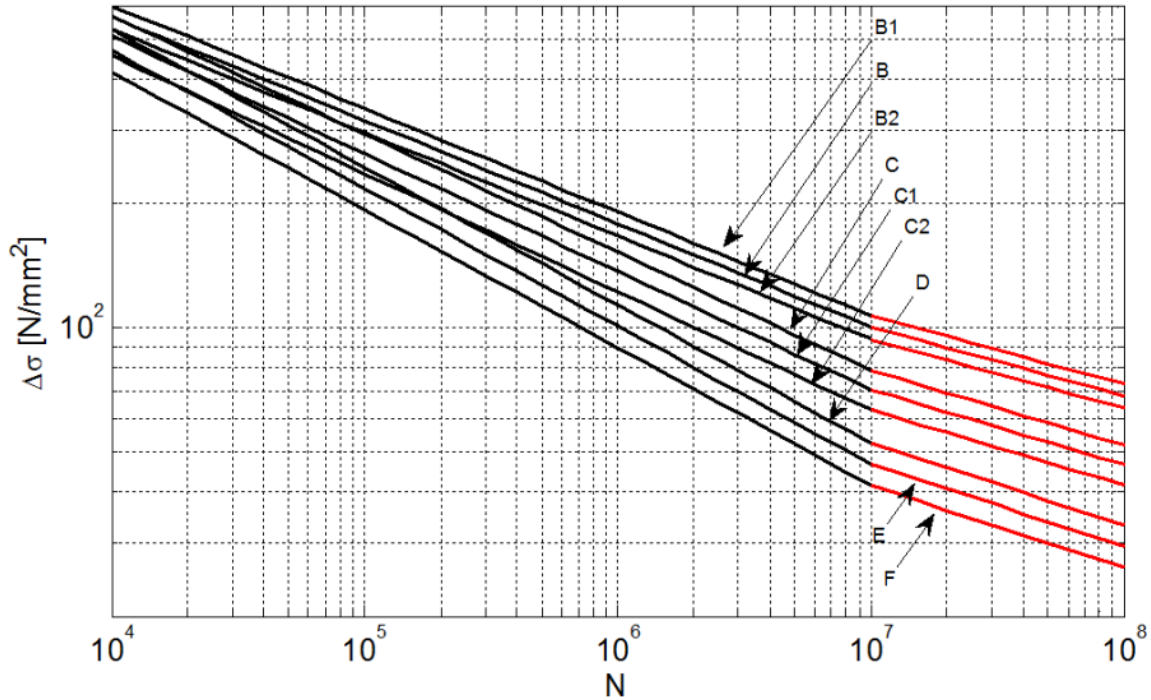


Figure 6.11: S-N curves in seawater with cathodic protection(CP) (DNV, 2015)

The cumulative fatigue life of the SST hull at different longitudinal locations is calculated based on the S-N curves by assuming linear cumulative damage using the Palmgren-Minor rule (Miner, 2021) (see Chapter-2, section 2.5.3 and Eq. (2.36)).

In Norway, it is recommended to use seawater S-N curve with cathodic protection and a high Design Fatigue Factor (DFF), especially for the splash zones (DNV, 2015). In this thesis, DFF equal to 10 is considered due to the high consequence of the failure. A high DFF is used because inspection and maintenance in some critical areas of the welds are regarded as challenging. This means the fatigue cracking probability is reduced (DNV, 2010a). For instance, DFF equal to 10 indicates that the fatigue crack probability throughout the lifespan becomes very low (accumulated probability less than 10^{-4} and annually less than 10^{-5} the final year in operation).

6.5. Environmental conditions

The wave conditions are based on location in the North Sea with a water depth of 300 m (DNV, 2010c). Table 6.7 summarizes all environmental parameters (H_s and T_p) and their probability of

occurrence for the 20 load cases used in this study. All the load cases are the sea state that will occur most often during its operation for the whole service life. The Joint North Sea Wave Project (JONSWAP) spectrum is used to model the time-varying irregular waves using the given H_s and T_p values. All the simulations are run for 1 hour.

Table 6.7: Representative sea states and their probability of occurrence

Load case	Wave height H_s (m)	Peak period T_p (secs)	Probabilities (%)	Exposure/year (Hrs)
1	1.5	8	4.16	364.21
2	1.5	9	4.62	405.07
3	1.5	10	5.65	495.29
4	1.5	11	6.80	595.53
5	1.5	12	4.36	382.20
6	2	9	4.72	413.81
7	2	10	6.75	591.68
8	2	11	6.78	594.25
9	2	12	5.66	495.81
10	2	13	6.48	567.52
11	2	14	6.02	527.42
12	2.5	11	6.57	575.23
13	2.5	14	7.46	653.36
14	3	11	5.06	443.11
15	3	12	4.19	366.78
16	3	13	3.94	345.19
17	4	9	1.46	127.74
18	4.5	14	4.48	392.48
19	5	10	1.27	111.04
20	5	14	3.56	312.29

The stress time series is obtained by calculating the bending moment for each sea state given in Table 6.7. The multibody approach presented in Chapter-4 and Chapter-5 is used to calculate the bending moment. Later, Python script is formulated to calculate the fatigue damage using the Rainflow counting approach (Matsuishi & Endo, 1968) (see Chapter-2 section 2.5.2, 2.5.3, and 2.6.3). The Rainflow counting approach evaluates fatigue data by compressing a spectrum of variable stresses into a collection of stress reversals. As a result, the Palmgren-Miner rule (Miner, 2021) can be used to evaluate the fatigue life of a structure under a complicated load. The total damage is estimated at the six different longitudinal locations of the multi-body SST hull.

All the simulations are performed for the seven-body actual torpedo-shape SST hull.

6.6. Fatigue assessment results – Hydrodynamics vs Hydrostatic

This section shows the results of accumulated fatigue damage and fatigue life of the SST due to wave-induced loads and changes in hydrostatic pressure due to dive-in and dive-out.

6.6.1. Wave-induced fatigue

Figure 6.12 and Figure 6.13 illustrates the fatigue damage and fatigue life over the longitudinal locations of the seven-body SST hull. For both the water depth, the critical locations for the damage are almost identical, with the most considerable fatigue damage occurring in the flooded-mid body of the SST. The uneven weight and buoyancy distribution in the vessel and high length to the width ratio results in the maximum bending stress at the mid-section of the vessel.

The major contributor of the damages are the effect from long waves (H_s above 2 m and T_p above 12 secs). The fatigue life increases up to 30 % when the SST travels at the water depth of 70 m, compared to the 40 m water depth. This means that going deep into the sea, decreases the effect of the long waves. This is why 70 m water depth is chosen as a nominal diving depth during operation. The summary of the fatigue damage and fatigue life is presented in Table 6.8.

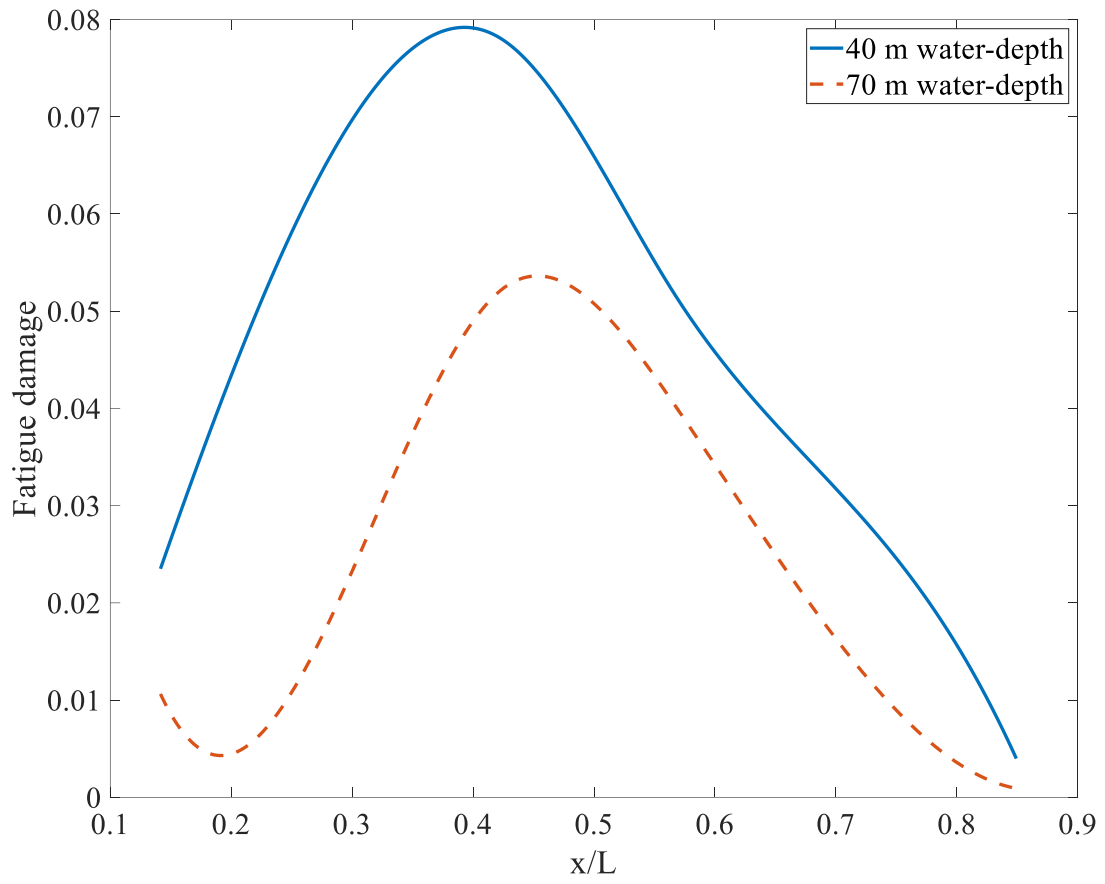


Figure 6.12: Fatigue damage at different longitudinal locations

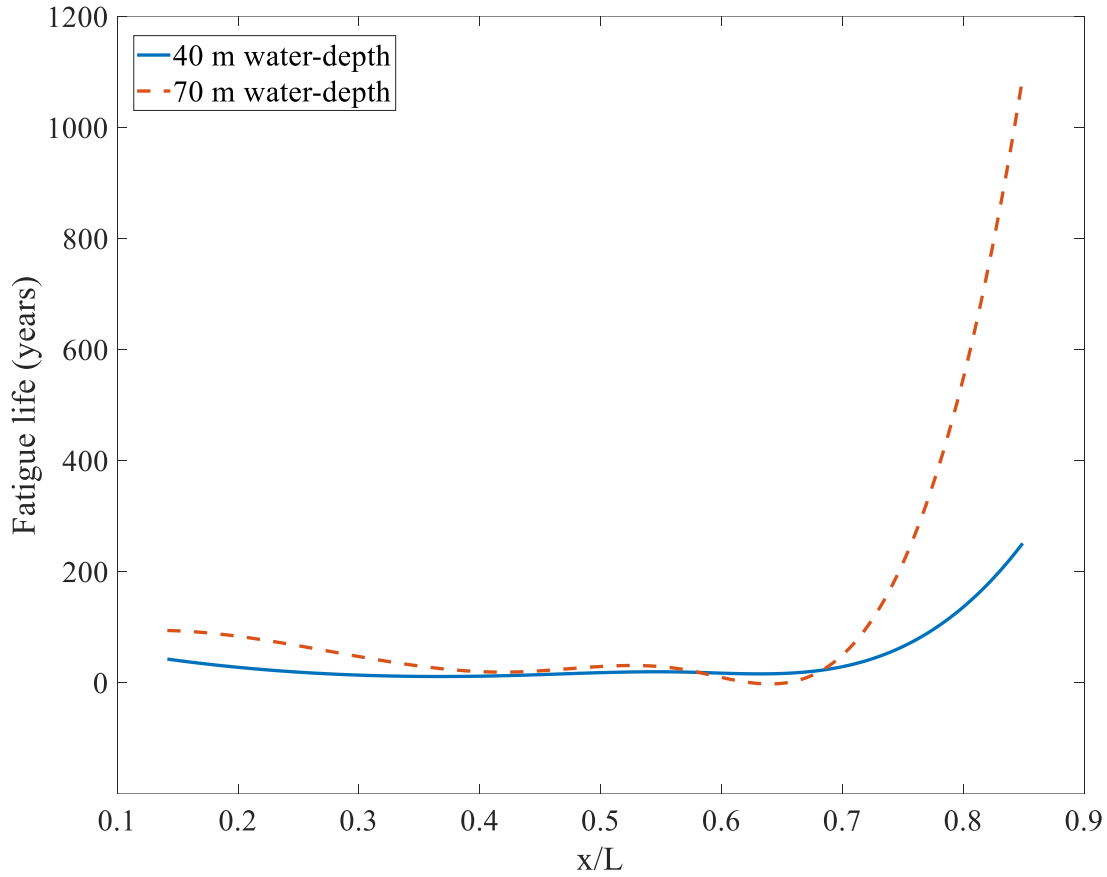


Figure 6.13: Fatigue life (years) at different longitudinal locations

Table 6.8: Summary of wave-induced fatigue at 40 m and 70 m water depth

40 m water depth						
x/L	0.142	0.283	0.425	0.566	0.708	0.849
Damage	0.0235	0.0662	0.0779	0.0518	0.0307	0.00398
Life (years)	42	15	13	19	33	251

70 m water depth						
x/L	0.142	0.283	0.425	0.566	0.708	0.849
Damage	0.0106	0.0186	0.0523	0.0405	0.0151	0.00092
Life (years)	94	53	19	25	66	1090

6.6.2. Fatigue due to hydrostatic pressure

The hoop stress is determined using a hydrostatic pressure of 0.703 MPa (nominal diving depth of SST, i.e., 70 m) applied on the external face of the SST pressure hull. Thus, a simple hand calculation is carried out to get a contribution of fatigue damage due to changes in hydrostatic pressure during dive-in and dive-out.

The SST can perform two weekly trips up to 70 m water depth (Xing et al., 2022). Therefore, the number of cycles in a year will become 104.28. Due to the high consequences of failure, DFF is chosen as 10. The summary of the fatigue life estimation due to hydrostatic pressure is presented in Table 6.9. Generally, the SST hull is flooded with water, and there are internal pressure vessels to compensate for the effect of the hydrostatic pressure, but they are not considered in this study. Therefore, fatigue life can be significantly increased if the latter conditions are considered.

Table 6.9: Summary of fatigue life due to hydrostatic pressure

σ_{hoop}	239.314 MPa
n	104.28
N	5520.66
<i>Accumulated damage (one year)</i>	0.188
<i>Fatigue life (years)</i>	5

Chapter 7 – Conclusion and recommendations for future work

7.1. Conclusion

The thesis is divided into two main parts. The first part of the thesis proposed a reliable and efficient multi-body approach to determine the bending moment of the SST under the effect of waves. The proposed approach is based on the discrete-module-beam bending-based hydroelasticity method. A continuous SST is divided into several multi-body rigid modules, and a planar sea-keeping model is established in Matlab Simulink based on the multi-body equation of the motion. The forces, which include hydrostatic restoring forces, waves excitation forces and radiation forces, are exerted on the center of gravity of each rigid module. The Cummins equation's convolution term is effectively solved using a state-space model. The convergence study is carried out by defining the stiffness in the connection joints to determine the most optimal number of bodies needed to perform the bending moment assessment. The accuracy of the dynamic response and bending moment is influenced by the number of decomposed bodies (i.e. the higher number of bodies, the higher the accuracy). The results show that a lower number of bodies (i.e., three and five) underestimates the bending moment at the given time instance even though the motion response converges for the heave and pitch direction. The less accurate response for the three and five-body SST can be because they may not have enough points to capture all wave encounter frequencies.

The second part of the thesis is the fatigue assessment of the SST hull, considering the effect of the local stresses at the welds. The finite element model of the flooded-mid body of the SST is prepared using the Ansys mechanical workbench 2020R1, followed by the mesh convergence study. Two different types of loading (i.e., external pressure and bending moment) are applied on the external hull of the SST to compute the SCF at the critical location. A 2D axisymmetric model is prepared to represent the external pressure problem, and the bending moment problem is modelled in 3D using shell elements. The resultant SCF is determined using the superposition approach. This approach indicates that the resultant SCF can be found by multiplication of the SCF obtained from the two individual models, provided that the stresses are linearly related to the loads. The fatigue assessment is based on the North Sea scatter diagram data. The analysis considers 20 load cases, and the simulation time for each load is one hour. The fatigue life of the

multi-body SST is then calculated using the Palmgren-Miner rule and the Rainflow counting approach based on the stress history. This method is capable of accurately and quickly assessing structural fatigue damage. The main contribution of the fatigue damage is expected due to long waves effect. The fatigue life at the flooded-mid body of the SST increases with the operation depth. This is because the effect from the long waves decreases with the depth resulting in less damage. However, there is significantly less contribution from the shorter waves. The minimum fatigue life observed is 13 and 19 years at the $x/L = 0.425$ at the 40 m and 70 m water depth, respectively. The fatigue life due to changes in hydrostatic pressure during dive-in and dive-out is five years. The average operation life of a military submarine is around 25-30 years. This low fatigue life of SST in this study is due to the high DFF consideration, thin-wall hull structure and stiffeners frames associated with a submarine, unless the numerous stiffeners and/or thick walls are used. Generally, the SST hull is flooded with water, and there are internal pressure vessels to compensate for the effect of the hydrostatic pressure, but they are not considered in this study. Therefore, fatigue life can be significantly increased if the latter conditions are considered.

7.2. Recommendations for future work

The following research studies are identified by the author for further study:

- The uncertainty associated with the stress concentration factor (SCF) value and how to reduce SCF to increase the fatigue life.
- Buckling assessment of the SST hull under the effect of hydrostatic pressure considering surface imperfection and stiffeners. The author provides the preliminary work (draft) (see Appendix G – Appended papers 2), and the approach is tested on the cylindrical shells to check the accuracy and correctness of the method. The numerical results show a good agreement with the experimental results.

References

- Allen, M., Antwi-Agyei, P., Aragon-Durand, F., Babiker, M., Bertoldi, P., Bind, M., Brown, S., Buckeridge, M., Camilloni, I., & Cartwright, A. (2019). *Technical Summary: Global warming of 1.5 C. An IPCC Special Report on the impacts of global warming of 1.5 C above pre-industrial levels and related global greenhouse gas emission pathways, in the context of strengthening the global response to the threat of climate change, sustainable development, and efforts to eradicate poverty.*
- American Bureau of Shipping. (2003). *Guide for the fatigue assessment of offshore structures.* American Bureau of shipping.
- Ariduru, S. (2004). *Fatigue life calculation by rainflow cycle counting method* [Master Thesis, Middle East Technical University]. <https://open.metu.edu.tr/handle/11511/14919>
- Åström, K. J., Hägglund, T., & Astrom, K. J. (2006). *Advanced PID control* (Vol. 461). ISA-The Instrumentation, Systems, and Automation Society Research Triangle Park.
- Benasciutti, D., & Tovo, R. (2006). Comparison of spectral methods for fatigue analysis of broadband Gaussian random processes. *Probabilistic Engineering Mechanics*, 21(4), 287–299. <https://doi.org/10.1016/j.probenmech.2005.10.003>
- Bowers, A. H., Murillo, O. J., Jensen, R. R., Eslinger, B., & Gelzer, C. (2016). *On wings of the minimum induced drag: Spanload implications for aircraft and birds.*
- British Standard. (2019). *BS 7910.* <https://standard.no/no/Nettbutikk/produktkatalogen/Produktpresentasjon/?ProductID=1109530>
- Carbon Capture and Storage Association. (2020). CCSA. <https://www.ccsassociation.org/>
- Chakrabarti, S. (2005). *Handbook of Offshore Engineering (2-volume set).* Elsevier.
- Choi, Y. R., & Hong, S. Y. (2002, May 26). *An Analysis of Hydrodynamic Interaction of Floating Multi-Body Using Higher-Order Boundary Element Method.* The Twelfth International

- Crippa, M., Guizzardi, D., Muntean, M., Schaaf, E., Solazzo, E., Monforti-Ferrario, F., Olivier, J. G. J., & Vignati, E. (2020). Fossil CO₂ emissions of all world countries. *Luxembourg: European Commission*, 1–244.
- Cummins, W. E., Iiuhl, W., & Uinm, A. (1962). *The impulse response function and ship motions*.
- DNV. (2010a). *DNV-RP-C203: Fatigue Design of Offshore Steel Structures*.
- DNV. (2010b). Fatigue Assessment of Ship Structures DNV Classification Notes No. 30.7. *Det Norske Veritas, Norway*.
- DNV. (2015). DNVGL-CG-0129: Fatigue Assessment of Ship Structures. *No. October*, 1–129.
- DNV. (2018). *Rules for classification: Naval vessels Part 4 Sub-surface ships Chapter 1 Submarines*. <https://rules.dnv.com/docs/pdf/DNV/RU-NAVAL/2018-01/DNVGL-RU-NAVAL-Pt4Ch1.pdf> (accessed on 1 August 2021).
- DNV. (2019). *DNV-RP-F112: Duplex stainless steel – design against hydrogen induced stress cracking*. DNV. <https://www.dnv.com/Default>
- DNV, G. L. (2010c). DNV-RP-C205: Environmental conditions and environmental loads. *Norway: Det Norske Veritas*, 896.
- Dong, Y., Garbatov, Y., & Guedes Soares, C. (2022). Review on uncertainties in fatigue loads and fatigue life of ships and offshore structures. *Ocean Engineering*, 264, 112514. <https://doi.org/10.1016/j.oceaneng.2022.112514>
- Dowling, N. E. (1971). Fatigue failure predictions for complicated stress strain histories. *TAM R* 337. <https://hdl.handle.net/2142/112063>
- Du, J., Li, H., Zhang, M., & Wang, S. (2015). A novel hybrid frequency-time domain method for the fatigue damage assessment of offshore structures. *Ocean Engineering*, 98, 57–65. <https://doi.org/10.1016/j.oceaneng.2015.02.004>

- Duarte, T. (2012). *Ssfitting-manual*. <https://www.nrel.gov/wind/nwtc/assets/pdfs/ssfitting-manual.pdf>
- Falnes, J., & Kurniawan, A. (2002). *Ocean Waves and Oscillating Systems: Linear Interactions Including Wave-Energy Extraction*. Cambridge University Press.
- Faltinsen, O. (1993). *Sea Loads on Ships and Offshore Structures*. Cambridge University Press.
- Fullenbaum, R., Fallon, J., & Flanagan, B. (2013). Oil & Natural Gas Transportation & Storage Infrastructure: Status, Trends, & Economic Benefits. *Washington: IHS Global Inc.* <https://www.circleofblue.org/wp-content/uploads/2014/12/API-Infrastructure-Investment-Study.pdf>
- Gaidai, O., Storhaug, G., Naess, A., Ye, R., Cheng, Y., & Xu, X. (2020). Efficient fatigue assessment of ship structural details. *Ships and Offshore Structures*, 15(5), 503–510.
- Gao, Z., & Moan, T. (2008). Frequency-domain fatigue analysis of wide-band stationary Gaussian processes using a trimodal spectral formulation. *International Journal of Fatigue*, 30(10), 1944–1955. <https://doi.org/10.1016/j.ijfatigue.2008.01.008>
- Gemilang, G. M., & Karunakaran, D. (2017, September 25). *Feasibility Study of Selected Riser Concepts in Deep Water and Harsh Environment*. ASME 2017 36th International Conference on Ocean, Offshore and Arctic Engineering. <https://doi.org/10.1115/OMAE2017-62453>
- Haselibozchaloe, D., Correia, J., Mendes, P., de Jesus, A., & Berto, F. (2022). A review of fatigue damage assessment in offshore wind turbine support structure. *International Journal of Fatigue*, 164, 107145. <https://doi.org/10.1016/j.ijfatigue.2022.107145>
- Hjulstad, Å., Kristiansen, E., & Egeland, O. (2004). State-space representation of frequency-dependent hydrodynamic coefficients. *IFAC Proceedings Volumes*, 37(10), 215–220. [https://doi.org/10.1016/S1474-6670\(17\)31734-2](https://doi.org/10.1016/S1474-6670(17)31734-2)
- Hong, S. Y., Choi, Y. R., & Hong, S. W. (2001, June 17). *Investigation of Draft Effects On Analysis of Hydroelastic Responses of Pontoon-Type VLFS*. The Eleventh International Offshore and Polar Engineering Conference. <https://onepetro.org/ISOPEIOPEC/proceedings-abstract/ISOPE01/All-ISOPE01/7758>

- Hong, S. Y., Kim, J. H., Cho, S. K., Choi, Y. R., & Kim, Y. S. (2003). *Numerical and Experimental Study on Hydrodynamic Interaction of Side-by-Side Moored Multiple Vessels*. 198–215. [https://doi.org/10.1061/40701\(2003\)14](https://doi.org/10.1061/40701(2003)14)
- Hong, S. Y., Kim, J. W., Shin, Y. S., & Ertekin, R. C. (2003, May 25). *An eigenfunction expansion method for hydroelastic analysis of a floating runway*. The Thirteenth International Offshore and Polar Engineering Conference. <https://onepetro.org/ISOPEIOPEC/proceedings-abstract/ISOPE03/All-ISOPE03/8350>
- Hu, Y., Li, D., & Chen, B. (2009). *Structural fatigue reliability analysis for naval architecture and ocean engineering*. Harbin Engineering University Press.
- Humamoto, T., & Fujita, K. (2002, May 26). *Wet-Mode Superposition For Evaluating the Hydroelastic Response of Floating Structures With Arbitrary Shape*. The Twelfth International Offshore and Polar Engineering Conference. <https://onepetro.org/ISOPEIOPEC/proceedings-abstract/ISOPE02/All-ISOPE02/8269>
- Jordán, M. A., & Beltrán-Aguedo, R. (2004). Optimal identification of potential-radiation hydrodynamics for moored floating structures—A new general approach in state space. *Ocean Engineering*, 31(14), 1859–1914. <https://doi.org/10.1016/j.oceaneng.2004.01.007>
- Kim, B. W., Young Hong, S., Kyoung, J. H., & Kyu Cho, S. (2007). Evaluation of bending moments and shear forces at unit connections of very large floating structures using hydroelastic and rigid body analyses. *Ocean Engineering*, 34(11), 1668–1679. <https://doi.org/10.1016/j.oceaneng.2006.10.018>
- Kristiansen, E., Hjulstad, Å., & Egeland, O. (2005). State-space representation of radiation forces in time-domain vessel models. *Ocean Engineering*, 32(17), 2195–2216. <https://doi.org/10.1016/j.oceaneng.2005.02.009>
- Kundu, P. K., Cohen, I. M., & Dowling, D. R. (2015). *Fluid Mechanics*. Academic Press.
- Legras, J.-L., Karunakaran, D. N., & Jones, R. L. (2013, May 6). *Fatigue Enhancement of SCRs: Design Applying Weight Distribution and Optimized Fabrication*. Offshore Technology Conference. <https://doi.org/10.4043/23945-MS>

- Levy, E. C. (1959). Complex-curve fitting. *IRE Transactions on Automatic Control*, *AC-4*(1), 37–43. <https://doi.org/10.1109/TAC.1959.6429401>
- Low, Y. M. (2011). Extending a time/frequency domain hybrid method for riser fatigue analysis. *Applied Ocean Research*, *33*(2), 79–87. <https://doi.org/10.1016/j.apor.2011.02.003>
- Low, Y. M., & Cheung, S. H. (2012). On the long-term fatigue assessment of mooring and riser systems. *Ocean Engineering*, *53*, 60–71. <https://doi.org/10.1016/j.oceaneng.2012.06.017>
- Lu, D., Fu, S., Zhang, X., Guo, F., & Gao, Y. (2019). A method to estimate the hydroelastic behaviour of VLFS based on multi-rigid-body dynamics and beam bending. *Ships and Offshore Structures*, *14*(4), 354–362. <https://doi.org/10.1080/17445302.2016.1186332>
- Ma, Y., Sui, D., Xing, Y., Ong, M. C., & Hemmingsen, T. H. (2021, October 11). *Depth Control Modelling and Analysis of a Subsea Shuttle Tanker*. ASME 2021 40th International Conference on Ocean, Offshore and Arctic Engineering. <https://doi.org/10.1115/OMAE2021-61827>
- Ma, Y., & Xing, Y. (2022). Identification of the safety operating envelope of a novel subsea shuttle tanker. *Ocean Engineering*, *266*, 112750. <https://doi.org/10.1016/j.oceaneng.2022.112750>
- Ma, Y., Xing, Y., Ong, M. C., & Hemmingsen, T. H. (2021). Baseline design of a subsea shuttle tanker system for liquid carbon dioxide transportation. *Ocean Engineering*, *240*, 109891. <https://doi.org/10.1016/j.oceaneng.2021.109891>
- Ma, Y., Xing, Y., & Sui, D. (2022). Trajectory Envelope of a Subsea Shuttle Tanker Hovering in Stochastic Ocean Current—Model Development and Tuning. *Journal of Offshore Mechanics and Arctic Engineering*, *145*(030901). <https://doi.org/10.1115/1.4055282>
- Masashi, K. (1997). A mode-expansion method for predicting hydroelastic behavior of a shall-draft VLFS. *Proceedings of the 16th International Conference on OMAE*, *0*(0), 179–186.
- Masson-Delmotte, V., Zhai, P., Pörtner, H.-O., Roberts, D., Skea, J., Shukla, P. R., Pirani, A., Moufouma-Okia, W., Péan, C., & Pidcock, R. (2018). *Global warming of 1.5 C. An IPCC Special Report on the impacts of global warming*.
- Matsuishi, M., & Endo, T. (1968). Fatigue of metals subjected to varying stress. *Japan Society of Mechanical Engineers, Fukuoka, Japan*, *68*(2), 37–40.

- McCabe, A. P., Bradshaw, A., & Widden, M. B. (2005). A time-domain model of a floating body using transforms. *6th European Wave and Tidal Energy Conference*, 281–288.
- Miner, M. A. (2021). Cumulative Damage in Fatigue. *Journal of Applied Mechanics*, 12(3), A159–A164. <https://doi.org/10.1115/1.4009458>
- Mowbray Jr, A. Q. (1950). *Effect of superposition of stress raisers on members subjected to static or repeated loads*. Department of Theoretical and Applied Mechanics. College of Engineering.
- Newman, J. N. (2018). *Marine Hydrodynamics*. The MIT Press. <https://library.oopen.org/handle/20.500.12657/26039>
- Ogilvie, T. F. (1964). Recent progress toward the understanding and prediction of ship motions. *Proceedings of the 5th Symposium on Naval Hydrodynamics, Bergen, Norway*, Pp. 3-80. <https://repository.tudelft.nl/islandora/object/uuid%3A5accdabd-b484-4450-9613-e1d2c5ee211e>
- Orimolade, A. P., Karunakaran, D., & Meling, T. S. (2015, October 21). *Steel Lazy Wave Risers From Turret Moored FPSO for Deepwater Harsh Environment*. ASME 2015 34th International Conference on Ocean, Offshore and Arctic Engineering. <https://doi.org/10.1115/OMAE2015-41004>
- Palmer, A. C., & King, R. A. (2008). *Subsea Pipeline Engineering 2nd Edition* Tulsa. *Oklahoma: PennWell*, 477–505.
- Paul Jr, F. W., & Faucett, T. R. (1962). *The superposition of stress concentration factors*.
- Perez, T., & Fossen, T. I. (2009). A Matlab Toolbox for Parametric Identification of Radiation-Force Models of Ships and Offshore Structures. *Modeling, Identification and Control: A Norwegian Research Bulletin*, 30(1), 1–15. <https://doi.org/10.4173/mic.2009.1.1>
- Perez, T., Smogeli, O., Fossen, T., & Sorensen, A. J. (2006). An overview of the Marine Systems Simulator (MSS): A simulink toolbox for marine control systems. *Modeling, Identification and Control*, 27(4), Article 4.

- Peterson, R. E. (1953). *Stress Concentration Design Factors*, Johy Willy & Sons. *Inc.*, *New York*.
- Robles, L. B. R., Buelta, M. A., Gonçalves, E., & Souza, G. F. M. (2000). A method for the evaluation of the fatigue operational life of submarine pressure hulls. *International Journal of Fatigue*, 22(1), 41–52. [https://doi.org/10.1016/S0142-1123\(99\)00102-4](https://doi.org/10.1016/S0142-1123(99)00102-4)
- Rohith, T., & Jayalekshmi, R. (2017). Deterministic and spectral fatigue analysis of tubular joints of a jacket platform. *International Journal of Scientific & Engineering Research*, 8(11).
- Rychlik, I. (1987). A new definition of the rainflow cycle counting method. *International Journal of Fatigue*, 9(2), 119–121. [https://doi.org/10.1016/0142-1123\(87\)90054-5](https://doi.org/10.1016/0142-1123(87)90054-5)
- Sanathanan, C., & Koerner, J. (1963). Transfer function synthesis as a ratio of two complex polynomials. *IEEE Transactions on Automatic Control*, 8(1), 56–58. <https://doi.org/10.1109/TAC.1963.1105517>
- Schjøberg, I., & Utne, I. B. (2015). Towards autonomy in ROV operations. *IFAC-PapersOnLine*, 48(2), 183–188. <https://doi.org/10.1016/j.ifacol.2015.06.030>
- Sen, T. K. (2006). Probability of Fatigue Failure in Steel Catenary Risers in Deep Water. *Journal of Engineering Mechanics*, 132(9), 1001–1006. [https://doi.org/10.1061/\(ASCE\)0733-9399\(2006\)132:9\(1001\)](https://doi.org/10.1061/(ASCE)0733-9399(2006)132:9(1001))
- Sim, I. H. (1998). An analysis of the hydroelastic behaviour of large floating structures in oblique waves. *Proceedings of the 2nd International Conference on Hydroelasticity in Marine Technology*, 195–200.
- Skotny, Ł. (2019, February 21). Why is a Triangular Element Stiffer? *Enterfea*. <https://enterfea.com/why-is-a-triangular-element-stiffer/>
- United Nation. (2015). *Paris Agreement—United Nations Framework Convention on Climate Change*. https://unfccc.int/sites/default/files/english_paris_agreement.pdf
- Vestereng, C. (2019). *Shuttle Tankers in Brazil*. www.dnv.com/expert-story/maritime-impact/shuttle-tankers-Brazil.html.

- Vicentini, V. (1967). Stress-concentration factors for superposed notches: A solution for two-dimensional stress-concentration factors for superposed semicircular notches symmetrically placed at the edges of a strip under pure tension is proposed by the author. *Experimental Mechanics*, 7, 117–123.
- Wilson, J. (2008, April 15). *Shuttle tankers vs. Pipelines in the GOM frontier*. <https://www.worldoil.com/magazine/2008/april-2008/features/shuttle-tankers-vs-pipelines-in-the-gom-frontier>
- Wirsching, P. H., & Light, M. C. (1980). Fatigue under Wide Band Random Stresses. *Journal of the Structural Division*, 106(7), 1593–1607. <https://doi.org/10.1061/JSDEAG.0005477>
- Wirsching, P. H., Paez, T. L., & Ortiz, K. (2006). *Random Vibrations: Theory and Practice*. Courier Corporation.
- Xin, Q. (2013). Durability and reliability in diesel engine system design. *Diesel Engine System Design*, 113–202.
- Xing, Y. (2021, October 11). *A Conceptual Large Autonomous Subsea Freight-Glider for Liquid CO2 Transportation*. ASME 2021 40th International Conference on Ocean, Offshore and Arctic Engineering. <https://doi.org/10.1115/OMAE2021-61924>
- Xing, Y., Gaidai, O., Ma, Y., Naess, A., & Wang, F. (2022). A novel design approach for estimation of extreme responses of a subsea shuttle tanker hovering in ocean current considering aft thruster failure. *Applied Ocean Research*, 123, 103179. <https://doi.org/10.1016/j.apor.2022.103179>
- Xing, Y., Ong, M. C., Hemmingsen, T., Ellingsen, K. E., & Reinås, L. (2020). Design Considerations of a Subsea Shuttle Tanker System for Liquid Carbon Dioxide Transportation. *Journal of Offshore Mechanics and Arctic Engineering*, 143(4). <https://doi.org/10.1115/1.4048926>
- Xing, Y., Santoso, T. A. D., & Ma, Y. (2022). Technical–Economic Feasibility Analysis of Subsea Shuttle Tanker. *Journal of Marine Science and Engineering*, 10(1), Article 1. <https://doi.org/10.3390/jmse10010020>

- Yasuzawa, Y., Kagawa, K., Kawano, D., & Kitabayashi, K. (1997). Dynamic response of a large flexible floating structure in regular waves: Proceedings of the 1997 16th International Conference on Offshore Mechanics and Arctic Engineering. Part 1-B (of 6). *Ocean Space Utilization*, 6, 187–194.
- Yu, L., Li, R., & Shu, Z. (2004, May 23). *A Numerical And Experimental Study On Dynamic Responses of MOB Connectors*. The Fourteenth International Offshore and Polar Engineering Conference. <https://onepetro.org/ISOPEIOPEC/proceedings-abstract/ISOPE04/All-ISOPE04/9155>
- Zhao, Y. (2012). A fatigue reliability analysis method including super long life regime. *International Journal of Fatigue*, 35(1), 79–90. <https://doi.org/10.1016/j.ijfatigue.2010.11.011>
- Zwick, D., & Muskulus, M. (2016). Simplified fatigue load assessment in offshore wind turbine structural analysis. *Wind Energy*, 19(2), 265–278. <https://doi.org/10.1002/we.1831>

Appendix B – MATLAB code of frequency-domain identification of radiation model

Use of FDI toolbox to identify a parametric model of the seven-body SST based on hydrodynamic data, including infinite-frequency added mass.

```
clear all;
addpath(' ../FDIToolbox');

%Load data of the SST (structure vessel)
load vessel.mat

Dof_cases = [1 1; 1 5; 1 7; 1 11; 1 13; 1 17; 1 19; 1 23; 1 25; 1 29; 1 31; 1 35; 1
37; 1 41; 3 3; 3 9; 3 15; 3 21; 3 27; 3 33; 3 39; 5 5; 5 7; 5 11; 5 13; 5 17; 5 19; 5
23; 5 25; 5 29; 5 31; 5 35; 5 37; 5 41; 7 7; 7 11; 7 13; 7 17; 7 19; 7 23; 7 25; 7 29;
7 31; 7 35; 7 37; 7 41; 9 9; 9 15; 9 21; 9 27; 9 33; 9 39; 11 11; 11 13; 11 17; 11 19;
11 23; 11 25; 11 29; 11 31; 11 35; 11 37; 11 41; 13 13; 13 17; 13 19; 13 23; 13 25; 13
29; 13 31; 13 35; 13 37; 13 41; 15 15; 15 21; 15 27; 15 33; 15 39; 17 17; 17 19; 17
23; 17 25; 17 29; 17 31; 17 35; 17 37; 17 41; 19 19; 19 23; 19 25; 19 29; 19 31; 19
35; 19 37; 19 41; 21 21; 21 27; 21 33; 21 39; 23 23; 23 25; 23 29; 23 31; 23 35; 23
37; 23 41; 25 25; 25 29; 25 31; 25 35; 25 37; 25 41; 27 27; 27 33; 27 39; 29 29; 29
31; 29 35; 29 37; 29 41; 31 31; 31 35; 31 37; 31 41; 33 33; 33 39; 35 35; 35 37; 35
41; 37 37; 37 41; 39 39; 41 41];

for i = 1:size(Dof_cases,1)

%Extract the data from the vessel structure
Dof = [Dof_cases(i,1),Dof_cases(i,2)]; %1-surge, 2-heave, 3-pitch
Nf = length(vessel.freqs);
W=vessel.freqs(1:Nf-1)';
Ainf=vessel.A(Dof(1),Dof(2),Nf);

A = reshape(vessel.A(Dof(1),Dof(2),1:Nf-1),1,length(W))';
B = reshape(vessel.B(Dof(1),Dof(2),1:Nf-1),1,length(W))';

%Define the structure with identification algorithm options
FDIopt.OrdMax      = 20;
FDIopt.AinfFlag    = 1;
FDIopt.Method      = 2;
FDIopt.Iterations  = 20;
FDIopt.PlotFlag    = 0;
FDIopt.LogLin      = 1;
FDIopt.wsFactor    = 0.1;
FDIopt.wminFactor  = 0.1;
FDIopt.wmaxFactor  = 5;

%call identification routine
[Krad,Ainf_hat]=FDIRadMod(W,A,Ainf,B,FDIopt,Dof);
filename = sprintf('SST_Krad%d%d.mat',Dof_cases(i,1),Dof_cases(i,2));
save(filename,'Krad');
end
```


Appendix C – MATLAB code to determine a state-space model to compute free-surface memory effect for seven body SST

```
clear all;
model = 'SST';

% from hydro model

Dof_cases = [1 1; 1 5; 1 7; 1 11; 1 2; 1 17; 1 19; 1 23; 1 25; 1 29; 1 31; 1 35; 1 8;
1 41; 3 3; 3 9; 3 15; 3 21; 3 27; 3 33; 3 39; 5 1; 5 5; 5 7; 5 11; 5 2; 5 17; 5 19; 5
23; 5 25; 5 29; 5 8; 5 35; 5 37; 5 41; 7 1; 7 5; 7 7; 7 2; 7 13; 7 17; 7 19; 7 23; 7
25; 7 29; 7 31; 7 35; 7 37; 7 41; 9 3; 9 9; 9 15; 9 21; 9 27; 9 33; 9 39; 11 1; 11 5;
2 7; 11 11; 11 13; 11 17; 11 19; 11 23; 11 25; 11 29; 11 31; 11 35; 11 37; 11 41; 2 1;
2 5; 13 7; 13 11; 13 13; 13 17; 13 19; 13 23; 13 25; 13 29; 13 31; 13 35; 13 37; 13
41; 15 3; 15 9; 15 15; 15 21; 15 27; 15 33; 15 39; 17 1; 17 5; 17 7; 17 11; 17 13; 17
17; 17 19; 17 23; 17 25; 17 29; 17 31; 17 35; 17 37; 17 41; 19 1; 19 5; 19 7; 19 11;
19 13; 19 17; 19 19; 19 23; 19 25; 19 29; 19 31; 19 35; 19 37; 19 41; 21 3; 21 9; 21
15; 21 21; 21 27; 21 33; 21 39; 23 1; 23 5; 23 7; 23 11; 23 13; 23 17; 23 19; 23 23;
23 25; 23 29; 23 31; 23 35; 23 37; 23 41; 25 1; 25 5; 25 7; 25 11; 25 13; 25 17; 25
19; 25 23; 25 25; 25 29; 25 31; 25 35; 25 37; 25 41; 27 3; 27 9; 27 15; 27 21; 27 27;
27 33; 27 39; 29 1; 29 5; 29 7; 29 11; 29 13; 29 17; 29 19; 29 23; 29 25; 29 29; 29
31; 29 35; 29 37; 29 41; 31 1; 31 5; 31 7; 31 11; 31 13; 31 17; 31 19; 31 23; 31 25;
31 29; 31 31; 31 35; 31 37; 31 41; 33 3; 33 9; 33 15; 33 21; 33 27; 33 33; 33 39; 35
1; 35 5; 35 7; 35 11; 35 13; 35 17; 35 19; 35 23; 35 25; 35 29; 35 31; 35 35; 35 37;
35 41; 8 1; 37 5; 37 7; 37 11; 37 13; 37 17; 37 19; 37 23; 37 25; 37 29; 37 31; 37 35;
37 37; 37 41; 39 3; 39 9; 39 15; 39 21; 39 27; 39 33; 39 39; 41 1; 41 5; 41 7; 41 11;
41 13; 41 17; 41 19; 41 23; 41 25; 41 29; 41 31; 41 35; 41 37; 41 41];

% dof in simulink model

Order = [1 1; 1 3; 1 1; 1 3; 1 1; 1 3; 1 1; 1 3; 1 1; 1 3; 1 1; 1 3; 1 1; 1 3; 2 2; 2
2; 2 2; 2 2; 2 2; 2 2; 3 1; 3 3; 3 1; 3 3; 3 1; 3 3; 3 1; 3 3; 3 1; 3 3; 3 1; 3
3; 3 1; 3 3];

Dr = zeros(1,1);

m = 35;

ki = 1;
kj = 1;
for curr = 1:m

i = order(curr,1);
j = order(curr,2);
i2 = Dof_cases(curr,1);
j2 = Dof_cases(curr,2);

if i >= j
    filename = sprintf('%s_Krad%d%d.mat',model,j2,i2);
else
    filename = sprintf('%s_Krad%d%d.mat',model,i2,j2);
end
```

```

load(filename);
ssrad = ss(Krad); % Forming SS matrix
A = ssrad.A;
B = ssrad.B;
C = ssrad.C;
D = ssrad.D;

n = size(A,1);

Ar(kj:n+kj-1,kj:n+kj-1) = A;
Br(kj:n+kj-1,i) = B;
Cr(i,kj:n+kj-1) = -C;

ki = ki + 1;
kj = kj + n;

end

ss_model6 = ss(Ar,Br,Cr,Dr);

save('SST_ss_model6.mat','ss_model6');

load('vessel.mat');
vessel.ss_model6 = ss_model6;
save('SST_vessel6.mat','vessel');

```

Appendix D – Python code for Rainflow counting method

```
"""
from numpy import fabs as fabs
import numpy as np

def rainflow(array_ext,
             flm=0, l_ult=1e16, uc_mult=0.5):
    """ Rainflow counting of a signal's turning points with Goodman correction

    Args:
        array_ext (numpy.ndarray): array of turning points

    Keyword Args:
        flm (float): fixed-load mean [opt, default=0]
        l_ult (float): ultimate load [opt, default=1e16]
        uc_mult (float): partial-load scaling [opt, default=0.5]

    Returns:
        array_out (numpy.ndarray): (5 x n_cycle) array of rainflow values:
            1) load range
            2) range mean
            3) Goodman-adjusted range
            4) cycle count
            5) Goodman-adjusted range with flm = 0

    """

    flmargin = l_ult - fabs(flm)           # fixed load margin
    tot_num = array_ext.size               # total size of input array
    array_out = np.zeros((5, tot_num-1))  # initialize output array

    pr = 0                                # index of input array
    po = 0                                # index of output array
    j = -1                                 # index of temporary array "a"
    a = np.empty(array_ext.shape)         # temporary array for algorithm

    # loop through each turning point stored in input array
    for i in range(tot_num):

        j += 1                             # increment "a" counter
        a[j] = array_ext[pr]               # put turning point into temporary array
        pr += 1                            # increment input array pointer

        while ((j >= 2) & (fabs( a[j-1] - a[j-2] ) <= \
            fabs( a[j] - a[j-1] ) ) ):
            lrange = fabs( a[j-1] - a[j-2] )

            # partial range
            if j == 2:
                mean = ( a[0] + a[1] ) / 2.
                adj_range = lrange * flmargin / ( l_ult - fabs(mean) )
                adj_zero_mean_range = lrange * l_ult / ( l_ult - fabs(mean) )
```

```

a[0]=a[1]
a[1]=a[2]
j=1
if (lrange > 0):
    array_out[0,po] = lrange
    array_out[1,po] = mean
    array_out[2,po] = adj_range
    array_out[3,po] = uc_mult
    array_out[4,po] = adj_zero_mean_range
    po += 1

# full range
else:
    mean      = ( a[j-1] + a[j-2] ) / 2.
    adj_range = lrange * flmargin / ( l_ult - fabs(mean) )
    adj_zero_mean_range = lrange * l_ult / ( l_ult - fabs(mean) )
    a[j-2]=a[j]
    j=j-2
    if (lrange > 0):
        array_out[0,po] = lrange
        array_out[1,po] = mean
        array_out[2,po] = adj_range
        array_out[3,po] = 1.00
        array_out[4,po] = adj_zero_mean_range
        po += 1

# partial range
for i in range(j):
    lrange = fabs( a[i] - a[i+1] );
    mean   = ( a[i] + a[i+1] ) / 2.
    adj_range = lrange * flmargin / ( l_ult - fabs(mean) )
    adj_zero_mean_range = lrange * l_ult / ( l_ult - fabs(mean) )
    if (lrange > 0):
        array_out[0,po] = lrange
        array_out[1,po] = mean
        array_out[2,po] = adj_range
        array_out[3,po] = uc_mult
        array_out[4,po] = adj_zero_mean_range
        po += 1

# get rid of unused entries
array_out = array_out[:, :po]

return array_out

```

Appendix E – Python code for fatigue calculator

```
import matplotlib.pyplot
import rainflow
import numpy as np
import pandas as pd

# definition of the stress ranges
a =
np.array([5.0,10.0,15.0,20.0,25.0,30.0,35.0,40.0,45.0,50.0,55.0,60.0,65.0,70.0,75.0,8
0.0])
b = np.array([0.0,0.0,0.0,0.0,0.0,0.0,0.0,0.0,0.0,0.0,0.0,0.0,0.0,0.0,0.0,0.0])
c = np.array([0.0,0.0,0.0,0.0,0.0,0.0,0.0,0.0,0.0,0.0,0.0,0.0,0.0,0.0,0.0,0.0])
d = np.array([0.0,0.0,0.0,0.0,0.0,0.0,0.0,0.0,0.0,0.0,0.0,0.0,0.0,0.0,0.0,0.0])

# number of sea states
s = 20
q = 0

while q<s:

    # reading of the input data

    data = pd.read_excel (r'C:\Users\268054\OneDrive - Universitetet I
Stavanger\General\Fatigue and buckling imperfection\Python code for
fatigue\70m\stress_joint6_70m.xlsx')
    df = pd.DataFrame(data, columns= [q+1])
    data = pd.read_excel (r'C:\Users\268054\OneDrive - Universitetet i
Stavanger\General\Fatigue and buckling imperfection\Python code for
fatigue\70m\test.xlsx')
    dg = pd.DataFrame(data, columns= ['zeros'])

    new_array = np.array(df)
    ext_array = np.array(dg)

    k=0
    h=0
    c = np.array([0.0,0.0,0.0,0.0,0.0,0.0,0.0,0.0,0.0,0.0,0.0,0.0,0.0,0.0,0.0,0.0])

    while k<(new_array.size-1):
        if new_array[k]<new_array[k-1] and new_array[k]<new_array[k+1]:
            ext_array[h] = new_array[k]
            h+=1
        if new_array[k]>new_array[k-1] and new_array[k]>new_array[k+1]:
            ext_array[h] = new_array[k]
            h+=1
        k+=1

    print(ext_array)

# rainflow analysis
from rainflow import rainflow
```

```

out_array = rainflow(ext_array)

print("Rainflow Output:")
print(out_array)

# cycle counting
i = 0
while i<(out_array.size)/5:
    if out_array[0,i]<=5.5:
        b[0]=b[0]+out_array[3,i]
    if out_array[0,i]>5.5 and out_array[0,i]<=10.5:
        b[1]=b[1]+out_array[3,i]
    if out_array[0,i]>10.5 and out_array[0,i]<=15.5:
        b[2]=b[2]+out_array[3,i]
    if out_array[0,i]>15.5 and out_array[0,i]<=20.5:
        b[3]=b[3]+out_array[3,i]
    if out_array[0,i]>20.5 and out_array[0,i]<=25.5:
        b[4]=b[4]+out_array[3,i]
    if out_array[0,i]>25.5 and out_array[0,i]<=30.5:
        b[5]=b[5]+out_array[3,i]
    if out_array[0,i]>30.5 and out_array[0,i]<=35.5:
        b[6]=b[6]+out_array[3,i]
    if out_array[0,i]>35.5 and out_array[0,i]<=40.5:
        b[7]=b[7]+out_array[3,i]
    if out_array[0,i]>40.5 and out_array[0,i]<=45.5:
        b[8]=b[8]+out_array[3,i]
    if out_array[0,i]>45.5 and out_array[0,i]<=50.5:
        b[9]=b[9]+out_array[3,i]
    if out_array[0,i]>50.5 and out_array[0,i]<=55.5:
        b[10]=b[10]+out_array[3,i]
    if out_array[0,i]>55.5 and out_array[0,i]<=60.5:
        b[11]=b[11]+out_array[3,i]
    if out_array[0,i]>60.5 and out_array[0,i]<=65.5:
        b[12]=b[12]+out_array[3,i]
    if out_array[0,i]>65.5 and out_array[0,i]<=70.5:
        b[13]=b[13]+out_array[3,i]
    if out_array[0,i]>70.5 and out_array[0,i]<=75.5:
        b[14]=b[14]+out_array[3,i]
    if out_array[0,i]>75.5:
        b[15]=b[15]+out_array[3,i]

    i+=1

# probability inclusion
date = pd.read_excel(r'C:\Users\268054\OneDrive - Universitetet i Stavanger\General\Fatigue and buckling imperfection\Python code for fatigue\70m\prob_test_DFF.xlsx')
prob = pd.DataFrame(date, columns= ['Probability'])
Scat = np.array(prob)

Scatter = Scat[q]
c = b*Scatter

#Accumulated cycles calculation

```

```
d[0]=d[0]+c[0]+c[1]+c[2]+c[3]+c[4]+c[5]+c[6]+c[7]+c[8]+c[9]+c[10]+c[11]+c[12]+c[13]+c[14]+c[15]
```

```
d[1]=d[1]+c[1]+c[2]+c[3]+c[4]+c[5]+c[6]+c[7]+c[8]+c[9]+c[10]+c[11]+c[12]+c[13]+c[14]+c[15]
```

```
d[2]=d[2]+c[2]+c[3]+c[4]+c[5]+c[6]+c[7]+c[8]+c[9]+c[10]+c[11]+c[12]+c[13]+c[14]+c[15]
```

```
  d[3]=d[3]+c[3]+c[4]+c[5]+c[6]+c[7]+c[8]+c[9]+c[10]+c[11]+c[12]+c[13]+c[14]+c[15]
```

```
  d[4]=d[4]+c[4]+c[5]+c[6]+c[7]+c[8]+c[9]+c[10]+c[11]+c[12]+c[13]+c[14]+c[15]
```

```
  d[5]=d[5]+c[5]+c[6]+c[7]+c[8]+c[9]+c[10]+c[11]+c[12]+c[13]+c[14]+c[15]
```

```
  d[6]=d[6]+c[6]+c[7]+c[8]+c[9]+c[10]+c[11]+c[12]+c[13]+c[14]+c[15]
```

```
  d[7]=d[7]+c[7]+c[8]+c[9]+c[10]+c[11]+c[12]+c[13]+c[14]+c[15]
```

```
  d[8]=d[8]+c[8]+c[9]+c[10]+c[11]+c[12]+c[13]+c[14]+c[15]
```

```
  d[9]=d[9]+c[9]+c[10]+c[11]+c[12]+c[13]+c[14]+c[15]
```

```
  d[10]=d[10]+c[10]+c[11]+c[12]+c[13]+c[14]+c[15]
```

```
  d[11]=d[11]+c[11]+c[12]+c[13]+c[14]+c[15]
```

```
  d[12]=d[12]+c[12]+c[13]+c[14]+c[15]
```

```
  d[13]=d[13]+c[13]+c[14]+c[15]
```

```
  d[14]=d[14]+c[14]+c[15]
```

```
  d[15]=d[15]+c[15]
```

```
  q+=1
```

```
# damage calculation
```

```
SN =
```

```
np.array([11419970345055, 252348077248, 27133016267, 5576157395, 1634293119, 599560619, 256  
818175, 123216834, 64466066, 36113117, 21379877, 13248543, 9032401, 6968781, 5473757, 4367018]  
)
```

```
D = d/SN
```

```
acc_D = sum(D)
```

```
annual_D = 365*24*3600*acc_D*10/3600
```

```
total_life = 1/(annual_D)
```

```
print("Stress Range", a)
```

```
print("Cycles", b)
```

```
print("Damage", d)
```

```
print("Miner",D)
```

```
print("Summation",acc_D)
```

```
print("accumulated annual damage",annual_D)
```

```
print("fatigue life",total_life)
```

```
j = 0
```

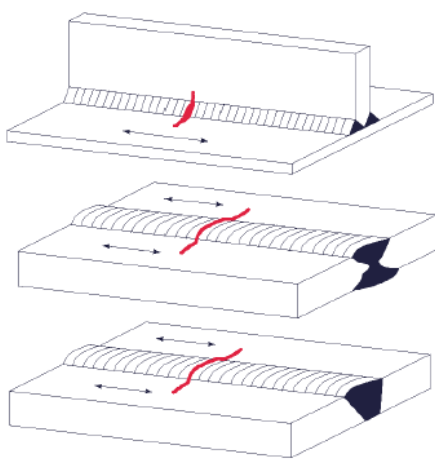
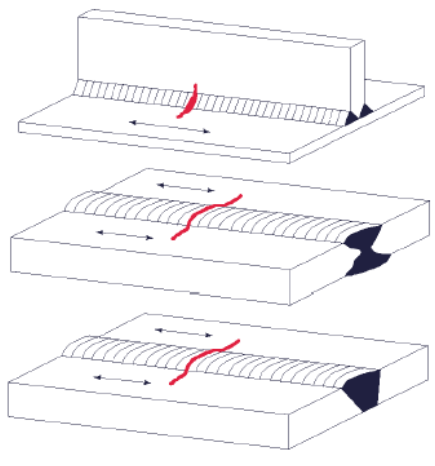
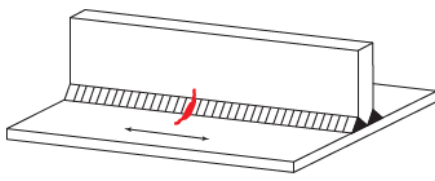
```
while j<(D.size):
```

```
  if D[j]>=1:
```

```
    print("Warning! Too many cycles for stress range", j+1)
```

```
  j+=1
```

Appendix F – Illustration of FAT class with *FAT X* number (DNV, 2015)

K_p/FAT N/mm^2	Figure	Description	Requirement
0.72/125		<p>1. Automatic welds carried out from both sides.</p>	<p>1. No start-stop position is permitted except when the repair is performed by a specialist and inspection carried out to verify the proper execution of the repair.</p>
0.80/112		<p>2. Automatic fillet or butt welds carried out from both sides, but containing stop-start positions.</p> <p>3. Automatic butt welds made from one side only, with a backing bar, but without start-stop positions.</p>	<p>3. When the detail contains start-stop positions use $K_p = 0.90$ or <i>FAT</i> 100</p>
0.90/100		<p>4. Manual fillet or butt welds.</p> <p>5. Manual or automatic butt welds carried out from one side only, particularly for box girders.</p> <p>6. Repaired automatic or manual fillet or butt welds.</p>	<p>5. A very good fit between the flange and web plates is essential. Prepare the web edge such that the root face is adequate for the achievement of regular root penetration with out brake-out.</p> <p>6. Improvement methods that are adequately verified may restore the original category.</p>

Appendix G – Appended papers

Paper -1

Modelling and analysis of the bending moment in a Subsea Shuttle Tanker under the effect of waves using a multi-body approach

Karan Sandipkumar Patel, Yucong Ma, Yihan Xing, Lin Li

Paper -2

Lower bound buckling capacity prediction for the isotropic cylindrical shell under axial compression loading using a probabilistic approach (Draft)

Karan Sandipkumar Patel, Yucong Ma, Yihan Xing

OMAE2023-100707

MODELING AND ANALYSIS OF THE BENDING MOMENT IN A SUBSEA SHUTTLE TANKER UNDER THE EFFECT OF WAVES USING A MULTI-BODY APPROACH

Karan Sandipkumar Patel

University Stavanger
Stavanger Norway

Yihan Xing

University Stavanger
Stavanger Norway

Yucong Ma

University Stavanger
Stavanger Norway

Lin Li

University Stavanger
Stavanger Norway

ABSTRACT

The Subsea Shuttle Tanker (SST) is a cost-effective, novel sizeable autonomous vehicle designed to transport liquid CO₂ between land facilities and smaller marginal fields. The SST travels underwater at a nominal diving depth of 70 m, allowing it to carry out freight operations in all weather conditions. Accurate structural assessment of large submarines is an essential part of structural reliability. In many practical cases, finite element methods (FEM) are used to predict the structural performance of the hull, but they come with significant computational expenses and time. This paper aims to present a reliable and efficient multi-body approach based on the discrete-module-beam bending-based hydroelasticity method to study the hydro-elastic behavior of SST hull at 40 and 70 m water depth. First, the continuous hull of the SST is discretized into several multi-body rigid modules. Then, a planar multi-body seakeeping model is presented to study the bending moment response of an interconnected multi-body rigid module under wave loads. The bending moment results are first measured using simplified multi-body geometry to ensure the use of the optimal number of model fidelity. The bending moment time series and power spectral density (PSD) have been analyzed in this paper. Numerical results also show that the mean bending moment at 40 m water depth is approximately 3 to 40 % greater than at 70 m water depth.

Keywords: submarine, autonomous underwater vehicle, seakeeping, potential flow theory, multi-body dynamics, bending moment

1. INTRODUCTION

1.1. Subsea Shuttle Tanker

Subsea pipelines and shuttle tankers are commonly used to transport hydrocarbons from offshore fields to onshore land facilities [1]. Laying a pipeline can be very expensive for the remotely located deep-water oil and gas fields with low-profit margins. Shuttle tanker operations are highly weather-dependent and cannot be carried out during severe weather conditions.

Considering this, various autonomous vehicles, such as autonomous freight submarines [2] and subsea gliders [3], are developed to be used as potential alternatives to subsea pipelines and shuttle tankers. Since these vessels operate subsurface, transportation is not halted even in extreme weather conditions.

Several ideas for the novel sizeable autonomous vehicle were presented by the Equinor ASA [4 & 5] in two research disclosures in 2019 for transporting liquid CO₂ from land or offshore-based facilities to subsea wells for an improved recovery process. Xing et al. [6] investigated primary design considerations regarding Subsea Shuttle Tanker (SST) to make it economically feasible. After that, the baseline design for an innovative 33600-ton SST was presented by Ma et al. [2].

The SST travels at 6 knots speed for maximum energy efficiency and at a 70 m constant water depth to attenuate the wave effects [2]. The wave loads or wave effects on the external hull of the SST are reduced up to a great extent at the given water depth. However, it is still essential to quantify and justify this reduction of wave effects in the given conditions to accurately predict the SST hull's structural performance. In addition, these dynamic load effects can potentially lead to fatigue damage to the SST external pressure hull. Also, as the SST has a large length-to-beam ratio, the external hull can be deformed by the combined effect of wave-induced loads and uneven weight and buoyancy distribution. FIGURE 2 illustrates the dynamic pressure variation with the depth and has a negative value under the wave trough and a positive value under the wave crest.

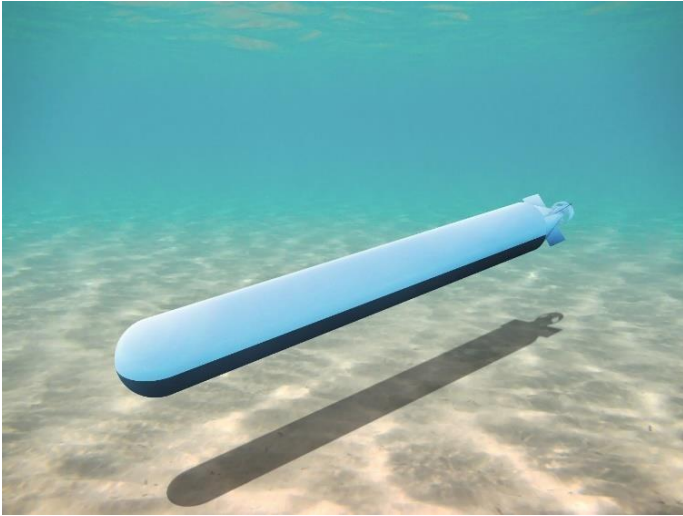


FIGURE 1: SUBSEA SHUTTLE TANKER (SST) [2]

In recent years, a substantial quantity of research has already been done on Very Large Floating Structures (VLFSs) like cargo and passenger ships, bridges, emergency bases, terminal airports, etc [7]. However, there is hardly any work done for large submarines regarding efficient and reliable structural assessment. In this work, the authors adapted the existing experiences on VLFSs and proposed a reliable and efficient multi-body approach for large slender structures like SST to study the bending moment response of the SST hull under the wave effects for an accurate structural assessment.

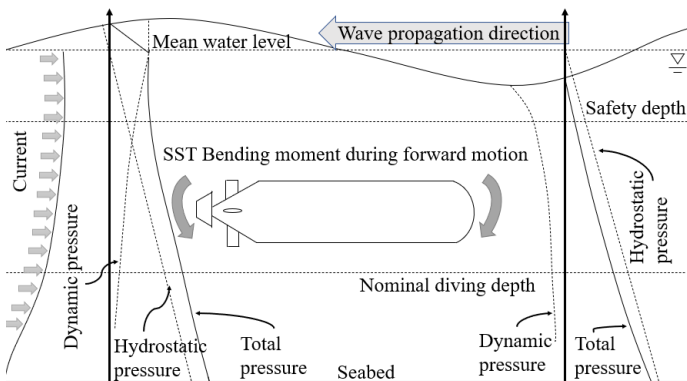


FIGURE 2: ENVIRONMENTAL LOADING ON THE SST HULL DURING ITS FORWARD MOTION

Accurately predicting the interaction between fluid fields and SST is a fundamental aspect. The classic hydrodynamic technique assumes the structure of a rigid body; therefore, it ignores the impact of structural deformation and gives an imprecise hydrodynamic response estimation [7]. Therefore, the hydro-elastic theory is more suitable for investigating large structures' or vessels' hydrodynamic responses. The hydrodynamic responses can be obtained by combining the structural dynamic and hydrodynamic equations, considering the interaction between hydrodynamic, inertia, and elastic forces [7]. Two-dimensional [8 & 9] and three-dimensional [10] hydro-

elastic theory was developed in the frequency domain, whereas Liu and Sakai [11] developed time-domain hydro-elastic theory at the same time. With the aid of two-dimensional and three-dimensional hydro-elastic theory, large semi-submersible pontoons are investigated, see [12].

Many VLFSs, which comprise several modules, are being analyzed using these theories and the multi-body analysis approach. Multi-body VLFSs such as side-by-side moored floating production storage and offloading (FPSO)-shuttle tanker systems are investigated by Hong et al. [13]. Global and local motion responses are numerically determined considering multi-body interaction and compared with the model test results. Choi and Hong [14] use the higher-order boundary element method (HOBEM) to investigate the hydrodynamic interaction of a floating multi-body system. The results are compared for two different offloading arrangements, side-by-side and tandem arrangements. Yu et al. [15] investigate multi-body mobile offshore base system's responses and connector forces by assuming bodies as rigid in numerical calculation. Several methods, such as the mode superposition method [16-18], eigenfunction expansion method [19 & 20] and direct method [21 & 22], have been used to investigate hydro-elastic responses. Kim et al. [23] investigate bending moment, stresses, and shear forces at connections of VLFS using a multi-body equation of motion. Hydrodynamic responses are calculated on each node, and total structural motion is derived by putting these responses together. Nonetheless, obtaining these responses in each mode is challenging due to irregular shape or stiffness. As a result, the direct method is used to examine structures whose modes are difficult to determine.

This paper investigates the SST hull's bending moment response using the multi-body approach based on the discrete-module-beam-bending based hydro-elastic method. First, a multi-body SST seakeeping planar model is presented based on the multi-body equation of motion. The empirical data are generated using time-domain simulation under different load cases. The main idea is to present a reliable and efficient methodology to investigate the structural performance and response of the SST hull against the bending moment under the influence of hydrodynamic forces considering hydroelectricity and connection stiffness.

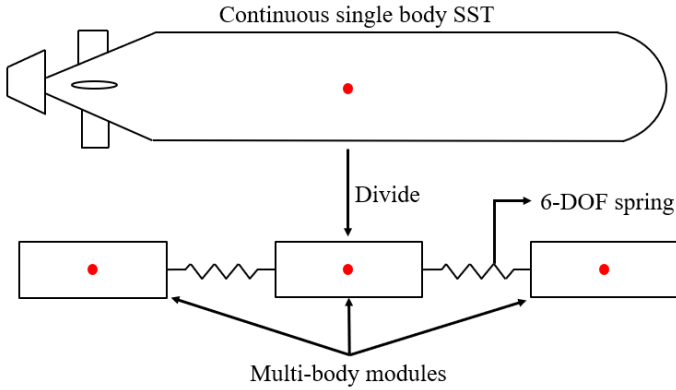
2. THEORETICAL BACKGROUND

The continuous flexible hull of the SST is divided into several bodies, as illustrated in FIGURE 3. Each body is considered a rigid body with no deformation. Subsequently, a spring flexibly connects two neighboring bodies. The hydrodynamic interaction with neighboring bodies affects the 6 degrees of freedom motion of each body. This paper uses linear wave theory assumptions to deal with hydrodynamic aspects, i.e., small wave steepness, non-viscous, incompressible, and irrotational flow. Then, hydrodynamic coefficients for the multi-body SST are calculated from potential flow theory, which breaks the total structural loads into the wave excitation force and radiation effect. Finally, multi-body SST responses in the presence of waves are obtained by solving a multi-body equation

of motion considering hydroelectricity and connection stiffness. The bending stiffness of the spring in pitch direction is given by Eq. (1):

$$K_{\theta} = \frac{4EI}{L} \quad (1)$$

where L is the length of the module, E is the modulus of elasticity, and I is the inertia moment.



• Center of Gravity
FIGURE 3: CONTINUOUS SST DIVIDED INTO MULTI-BODIES

2.1. Hydrodynamic Theory

The equation of motion of any offshore structure and marine vessel can be given as:

$$M_{RB}\ddot{\xi} = \tau \quad (2)$$

where: M_{RB} is the rigid body mass matrix; $\xi \triangleq [x, y, z, \phi, \theta, \psi]^T$ is a displacement vector that defines the position of the vessel or structure with respect to a reference frame (x-surge, y-sway, and z-heave, ϕ -roll, θ -pitch, and ψ -yaw); and $\tau \triangleq [X, Y, Z, K, M, N]^T$ is a force vector in a body frame (X -surge, Y -sway, and Z-heave, K-roll, M-pitch, and N-yaw).

$$\tau = \tau_{rad} + \tau_{visc} + \tau_{res} + \tau_{exc} \quad (3)$$

where τ_{rad} is radiation force due to a change in the momentum of the fluid, τ_{res} is restoring force due to buoyancy and gravity, τ_{ext} is wave excitation force by incident waves, τ_{visc} is viscous force.

Time-domain model

In this paper, the time-domain radiation force is represented by Cummin's equation [24]:

$$\tau_{rad} = -A_{\infty}\ddot{\xi} - \int_0^t K(t-t')\dot{\xi}(t')dt' \quad (4)$$

The first term in Eq. (4) reflects pressure force owing to the structure's acceleration and A_{∞} is infinite frequency added mass and K is retardation or memory function. The energy transfer from the motion of the structure to radiation waves is captured by the second term. It represents a fluid memory model. The kernel of the convolution term is the matrix of the memory function.

Combining Eq. (3) and Eq (4), Cummins [24] equation can be written as

$$(M_{RB} + A_{\infty})\ddot{\xi} + \int_0^t K(t-t')\dot{\xi}(t')dt' + G\xi = \tau_{exc} \quad (5)$$

The above equation represents the equation of motion of any offshore structure and vessel, provided the linear wave theory assumption is satisfied.

Frequency domain model

Radiation force in the frequency domain can be written as [25 & 26]

$$\tau_{rad}(j\omega) = -A(\omega)\ddot{\xi}(j\omega) - B(\omega)\dot{\xi}(j\omega) \quad (6)$$

where $A(\omega)$ and $B(\omega)$ are frequency-dependent added mass and damping. The equation of motion in the frequency domain can be written as

$$[-\omega^2[M + A(\omega)] + j\omega B(\omega) + G]\xi(j\omega) = \tau_{exc}(j\omega) \quad (7)$$

With the aid of the Fourier transform, Ogitive [27] shows the relationship between added mass and damping coefficient in the time domain and frequency domain.

$$A(\omega) = A_{\infty} - \frac{1}{\omega} \int_0^{\infty} K(t) \sin(\omega t) dt \quad (8)$$

$$B(\omega) = \int_0^{\infty} K(t) \cos(\omega t) dt \quad (9)$$

Again, using Fourier transform, the retardation function in the frequency domain can be represented as:

$$K(j\omega) = B(\omega) + j\omega[A(\omega) - A_{\infty}] \quad (10)$$

In this paper, the hydrodynamic coefficients ($A(\omega)$ and $B(\omega)$) for a finite set of frequency is obtained by using hydrodynamic codes (Wadam) based on potential theory.

Therefore, using the above equations, the equation of motion of the multi-body SST in the frequency domain is given as follows:

$$\begin{aligned}
& [-\omega^2[M_k + A_{kk}] + j\omega B_{kk} + G]\xi \\
& + \sum_{j=1, j \neq k}^n [-\omega^2 A_{kj} + j\omega B_{kj}]\xi \quad (11) \\
& = \tau_{exc}(j\omega)
\end{aligned}$$

where n is the number of bodies or modules, M_k is the mass matrix of the body k , A_{kk} and B_{kk} are the added mass and damping matrix caused by the moment of the body k by itself, G is hydrostatic or restoring force, ξ is the displacement vector, A_{kj} and B_{kj} are the added mass and damping matrix of the body k caused by the movement of body j . The number of equations is the same as the number of bodies.

Identification of Radiation-force model

A non-parametric fluid memory model can be utilized to construct a simulation model based on the Cummin [24] equation. This approach required saving a previous step's data to solve the convolution integral. The last-mentioned approach can be very time consuming and difficult to implement. Therefore, in this paper the fluid memory model is solved using linear time-invariant parametric model.

$$\mu = \int_0^t K(t-t')\dot{\xi}(t')dt' \approx \begin{cases} \dot{x} = \hat{A}x + \hat{B}\xi \\ \hat{\mu} = \hat{C}x \end{cases} \quad (12)$$

where x represents the state vector or fluid memory effect and \hat{A} , \hat{B} , and \hat{C} are constants.

In the frequency domain, Eq (12) can be written as

$$K(j\omega) \approx \hat{R}(j\omega) = \hat{C}(j\omega I - \hat{A})^{-1}\hat{B} \quad (13)$$

where $\hat{R}(s)$ is a transfer function. A state-space model (Eq. (12)) can be obtained by estimating the transfer function via canonical realization [28].

2.2. Forward Speed Effect

Added mass and damping coefficient will influence by the forward speed of the SST. SST travel at the 70 m constant water depth with the speed of 6 knots in the x-direction, see FIGURE 5. This problem may alternatively be characterized in the seakeeping frame as SST performing wave-induced oscillation in a steady flow of velocity U in the negative x-direction.

Due to the doppler effect, a regular wave is observed with a different angular frequency called encounter frequency ω_e in the seakeeping frame. The encounter frequency ω_e for the heading angle β between the wave propagation direction and SST can be given as [26]

$$\omega_e = \omega - kU\cos(\beta) \quad (14)$$

with ω is incoming wave frequency, k is wave number, U is forward speed, and β is heading angle.

Forward speed is considered by using encounter frequency. The authors considered the wave frequency range from 0.1 to 5 rad/sec with the step of 0.05 rad/sec. The corresponding wave number can be determined using dispersion relationship. Finally, using Eq. (14), the encounter frequency can be obtained which can be used as an input to a hydrodynamic softwares like WADAM.

In theory, the added mass and damping coefficients for any vessel moving at a forward speed can be written in the form [26]:

$$A_{jk} = A_{jk}^0 + UA_{jk}^{(1)} + U^2A_{jk}^{(2)} \quad (15)$$

$$B_{jk} = B_{jk}^0 + UB_{jk}^{(1)} + U^2B_{jk}^{(2)} \quad (16)$$

2.3. Approach

Obtaining a suitable mathematical model is very challenging for anyone seeking to develop a control system for a marine system. For this study, the Marine Hydro add-in provides with most widely used hydrodynamic codes. These codes calculate the added-mass and damping coefficients, restoring coefficients, excitation force and body motion transfer function (force-RAOs (response amplitude operator) and motion-RAOs), mean-drift force and moment, and so on using the geometrical parameters of the vessel and its loading conditions. The data structure of the SST is obtained using Marine System Simulator (MSS) [28]. The latter offers a smooth interface for the quick deployment of marine vessel models in three steps, see FIGURE 4:

- 1) Load the SST data into hydrodynamic software and execute it. For this paper, the authors used WADAM.
- 2) SST's data structure is obtained in MATLAB using the raw hydrodynamic data generated in WADAM.
- 3) With the aid of the Hydro add-in Simulink model, time-domain simulations are obtained for different sea states.

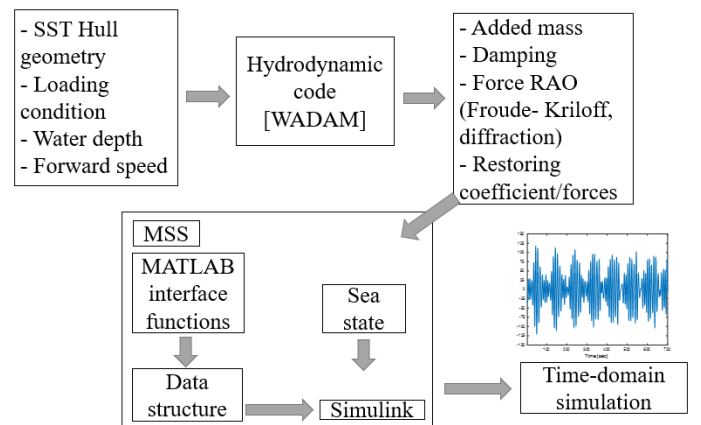


FIGURE 4: MARINE HYDRO CAPABILITIES

3. SUBSEA SHUTTLE TANKER PLANAR MODEL

3.1. Design Parameters

Ma et al. [2] presented the baseline design of the SST. SST travels at 70 m below mean sea level at the speed of 6 knots for maximum energy efficiency.

TABLE 1 shows the most important design parameters for the SST.

TABLE 1: DESIGN PARAMETER OF SST

Parameter	Unit	Value
Length	m	164
Beam	m	17
Total mass (m)	kg	3.36×10^7
Pitch moment of inertia (I_{yy})	$\text{kg} \cdot \text{m}^2$	3.63×10^9
Centre of buoyancy [x_b, y_b, z_b]	m	[0, 0, -0.41]
Aft skeg position (x_s)	m	-70
Bow skeg position (x_b)	m	30
Skeg area (A_s)	m	40
Carbon dioxide capacity	kg	1.7×10^6

3.2. Seakeeping Model

3.2.1. Coordinate system

FIGURE 5 represents the global coordinate system, body-fixed coordinate system, and seakeeping coordinate system of the SST. The global coordinate system (o_n, x_n, y_n, z_n) or earth fixed coordinate system is North, East, and Down and is considered inertial. The body-fixed coordinate system (o_b, x_b, y_b, z_b) is located at the vessel's center of gravity (CoG), and its motion is relative to the global coordinate system. The seakeeping coordinates system (o_h, x_h, y_h, z_h) moves at the same speed as the SST following its path. When the SST moves at a constant speed (which includes the situation of zero speed), the wave-induced motion causes the SST to oscillate with respect to the seakeeping frame. It is also considered an inertial frame. The center of buoyancy (CoB) of the vessel is located right above the CoG.

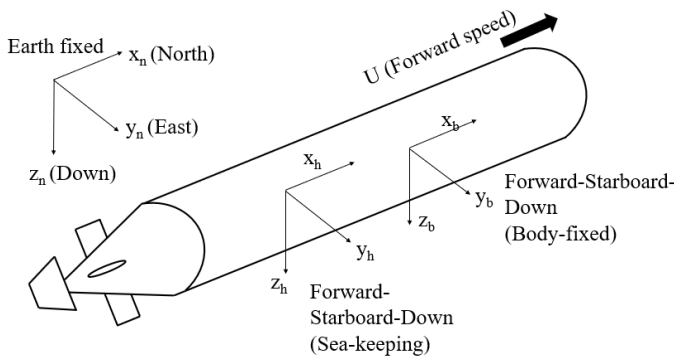


FIGURE 5: THE COORDINATE SYSTEM OF THE SST

3.2.2. Plant model

The equation of motion of SST can be written as:

$$\begin{aligned}
 \text{Inertia forces} & M_{RB}\dot{v} + M_A\dot{v} \\
 \text{Damping forces} & + (D_p + D_v)v_r + \mu_r \\
 \text{Restoring forces} & + G\eta + g_0 \\
 \text{Wave forces} & = \tau_{waves}
 \end{aligned} \tag{17}$$

where M_{RB} is the rigid body mass matrix, M_A is the added mass matrix, D_p is the linear potential damping, D_v is the viscous damping; $G\eta + g_0$ is ballast and restoring force; τ_{waves} is the wave excitation forces (consists of Froude-Krylov and diffraction force).

3.2.3. Actuator model

The only actuator system carried on SST is skegs. Brief information on the skegs model is given in the following section.

Skegs

Pitch and depth are controlled by two skegs on the port and starboard sides of the SST bow and aft. The lift force produced by a skeg is given as:

$$\tau_s = 0.5\rho C_L S_{skeg} (\delta_s - \theta) u^2 \tag{18}$$

where $C_L = 6.1 \text{ rad}^{-1}$ is the lift coefficient of the skeg, which is, ρ is the density of seawater, $S_{skeg} = 40 \text{ m}^2$ and 50 m^2 are the aft skeg area and bow skeg area, respectively, δ_s is skeg angle which is fixed to 0 radians, θ is the angle of attack, and u is velocity. Bower's airfoil profile [29] is used in the design of the SST.

3.3. Simulink Implementation

With the aid of the above-mentioned mathematical formulation, the 2-D planar multi-body Simulink model is prepared for the SST. The empirical data is generated using time-domain simulation to determine the structural performance and response of the SST hull against the bending moment under the influence of hydrodynamic forces. It is divided into two blocks:

- Plant model: The equation of motion of the SST body is represented by the plant model by considering added mass, damping and body lift force.
- Actuators: This is the actuator contribution block, which includes aft and bow skegs.

Numerical simulations using Simulink are performed by defining the stiffness of the connection in joints, as shown in FIGURE 6. Theoretically, the behavior of the SST with infinite strength of the connection is identical to that of the single rigid body.

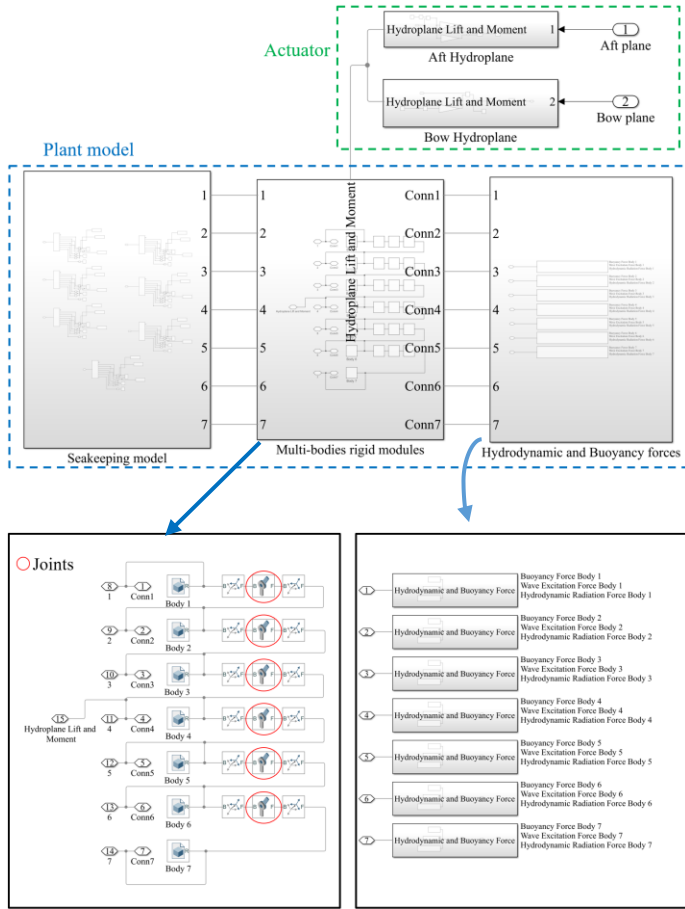


FIGURE 6: SEVEN BODIES SST SIMULINK DYNAMIC MODEL

4. CONTROL SYSTEM DESIGN

4.1. Proportional-Integral-Derivative Controller

The open-loop control system of the SST can be transformed into a closed-loop control system with the aid of a Proportional-Integral-Derivative (PID) type controller. Because of its popularity among autonomous subsea vehicles and marine operation fields, it controls the motion and achieves the desired performance for the system under consideration [30].

FIGURE 7 illustrates the control loop block diagram for the SST depth control issue. The error $e(t)$ between a measured value and the reference value is the input to a PID controller. The diagram illustrates that the actuator controls the input u from the PID controller. Then it is fed into the SST seakeeping block to obtain the output y with a correction multiplied by a proportional gain (K_p), integral gain (K_i), and derivative gain (K_d). The PID controller is described as:

$$u(t) = K_p e(t) + K_i \int_0^t e(t) dt + K_d \frac{de(t)}{dt} \quad (19)$$

where K_p is the proportional gain; K_i is the integral gain; K_d is the derivative gain; $e(t)$ is the error between the measured value and reference value.

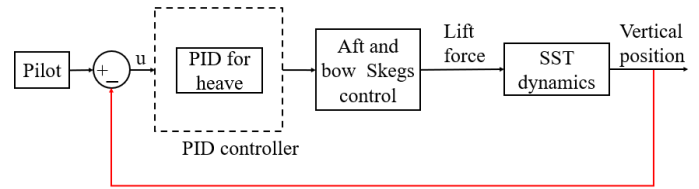


FIGURE 7: CONTROL BLOCK FOR SST

In this paper, $e(t)$ is the error between the measured heave response and the desired value of the SST. The output is the aft and bow hydroplane angle which is used to maintain the desired position of the SST. The controller gains of individual PID controllers in the heave direction, i.e., their corresponding K_p , K_i and K_d values, are used to tune this SST motion control.

5. CASE STUDY

Several cases with different model fidelity, operating depth, and wave parameters are considered to investigate the effect of bending moment.

The wave data are generated using the North Sea hindcast data from 2001 to 2010. TABLE 2 shows three closely comparable load instances chosen to emulate a highly probabilistic operational state faced by the SST. The time-varying irregular waves are modeled using Joint North Sea Wave Project (JONSWAP) with the respective significant wave height (H_S) and spectral peak period (T_P) values as shown in TABLE 2.

TABLE 2: WAVE PARAMETERS FOR SIMULATIONS

Load cases	H_S (m)	T_P (sec)	Simulation length (sec)
LC1	1.9	11.7	3600
LC2	2.5	12.1	3600
LC3	3.2	12.7	3600

The continuous SST is divided into three, five, seven, and nine bodies to investigate the effect of bending moments due to the model fidelity and above load condition in the 180° wave direction (head sea).

The depth definitions of the SST are as follows, see [2]:

- The safety depth is 40 m.
- The nominal diving depth is 70 m.
- The test diving depth is 105 m.

According to the depth mentioned in earlier definitions, the SST's operating depth range is between 40 m (safety depth) and 70 m (nominal diving depth). For maximum energy efficiency, SST travels at the slow speed of 6 knots at the nominal water depth of 70 m.

Based on the above depth definition, model fidelity, and load conditions, the different case studies are presented in TABLE 3 to investigate the bending moment for the SST hull when it is traveling at the constant speed of 6 knots.

TABLE 3: CASE STUDIES

Case study	No. of body	Operating depth (m)	Operating speed (knots)	Control type
3-70-6-tu	Three	70	6	Tunned
5-70-6-tu	Five	70	6	Tunned
7-70-6-tu	Seven	70	6	Tunned
9-70-6-tu	Nine	70	6	Tunned

The SST hull has a torpedo shape with a hemispherical bow, a long cylindrical mid-body section 130.5 m long, and a conical aft section 25 m long [2]. Because of the long cylindrical mid-body section, the geometry is relatively simple. Therefore, in this paper, the actual torpedo-shape SST is replicated with the simplified cylindrical geometry during the convergence study when deciding the minimum required number of bodies.

6. RESULT AND DISCUSSIONS

6.1. Controller Tuning for the Simplified Shape of SST

The Matlab transfer function-based PID tuner app is used in this paper as a tuning tool. Astrom et al. [31] highlighted the basic tuning principle for the selected controller. For the tuning, the PID tuner applies a system model linearized at an operational point. The tuner will automatically calculate the necessary controller gains and map out the system impulse response by adjusting the frequency domain's bandwidth and phase margin settings. TABLE 4 represents the most optimal PID controller gain for three, five, seven and nine bodies, respectively.

TABLE 4: MOST OPTIMAL PID CONTROLLER GAINS

Gains	Three bodies	Five bodies	Seven bodies	Nine bodies
K_p	-4.62	-3.44	-6.14	-5.92
K_i	-1.5×10^4	-1.4×10^4	-1.5×10^4	-1.4×10^4
K_d	-97.63	-115.17	-200.57	-137.98

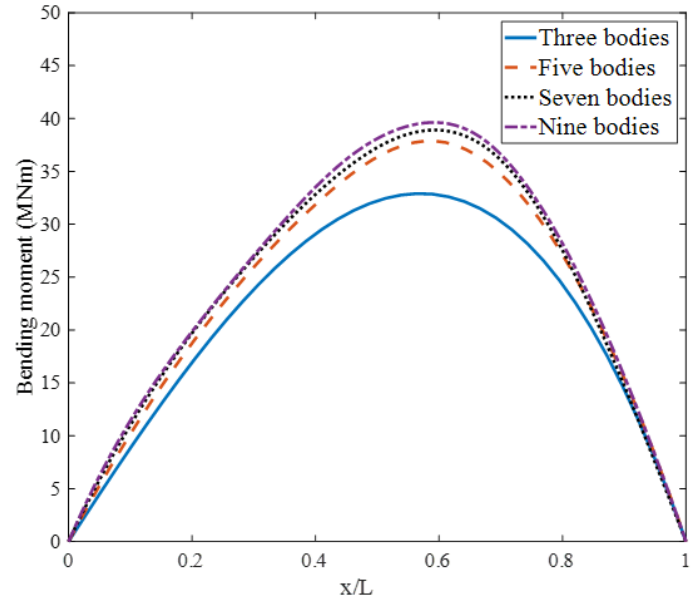
6.2. Convergence Study for the Simplified Multi-Body Structure

A full-fledged convergence study is performed to ensure the use of the optimal number of model fidelity for performing bending moment analysis to achieve reliable results. A set of wave excitation and radiation forces are exerted on the center of each module. The motion of each module can be obtained by solving Eq. (11). The number of decomposed bodies influences the accuracy of the calculated results. Theoretically, the dynamic response and bending moment accuracy increase by increasing the number of bodies.

To validate the convergence of different model fidelity, the bending moment results are compared for the three, five, seven, and nine bodies SST model in regular wave conditions at the nominal diving depth of 70 m, see FIGURE 8. The PID controller is tuned to its optimal gains, see TABLE 4. In all calculations, the wave amplitude and wave period are set to 1 m and 10 secs.

The simulation time for three, five, seven and nine bodies is almost the same, which makes the chosen methodology fast and reliable. However, it should be noted that the formation of input

data structure for radiation force for Simulink for the higher number of bodies may require some MATLAB coding for quick deployment.

**FIGURE 8: BENDING MOMENT DISTRIBUTION OF THE MULTI-BODY SST**

A comparison of the time series of the vertical displacement response and pitch response at the above-mentioned wave conditions and water depths is presented in FIGURE 9. The PID controller is tuned to its optimal gains. It is observed that the response amplitude in the heave and pitch direction is quite close to each other for different bodies. It is also noted that the pitch response has several small oscillations with different frequencies. These small peaks or irregularities can be because of small frequency oscillations in joint connections in MATLAB Simulink.

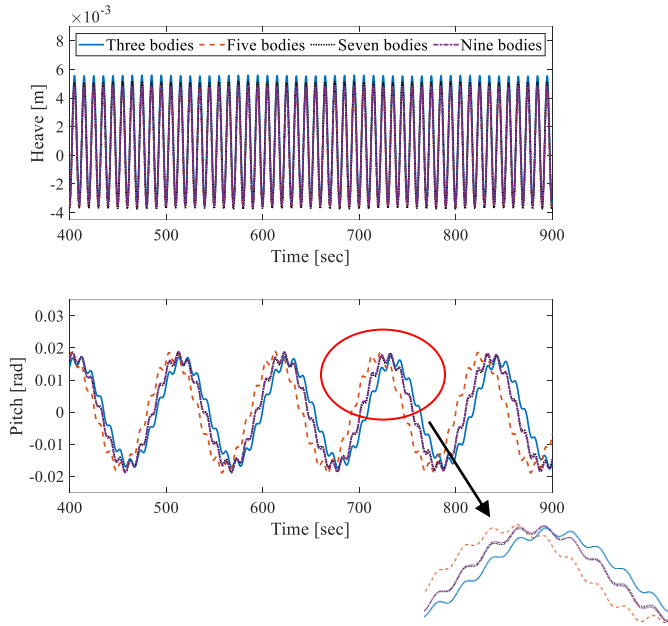


FIGURE 9: HEAVE AND PITCH RESPONSE OF MULTI-BODY SST

The bending moment response at three different time instances (i.e., at 520 secs, 525 secs, and 530 secs) are presented for five, seven, and nine-bodies SST models, see FIGURE 10. The wave amplitude is 1 m, the wave period is 10 sec, and the water depth is 70 m.

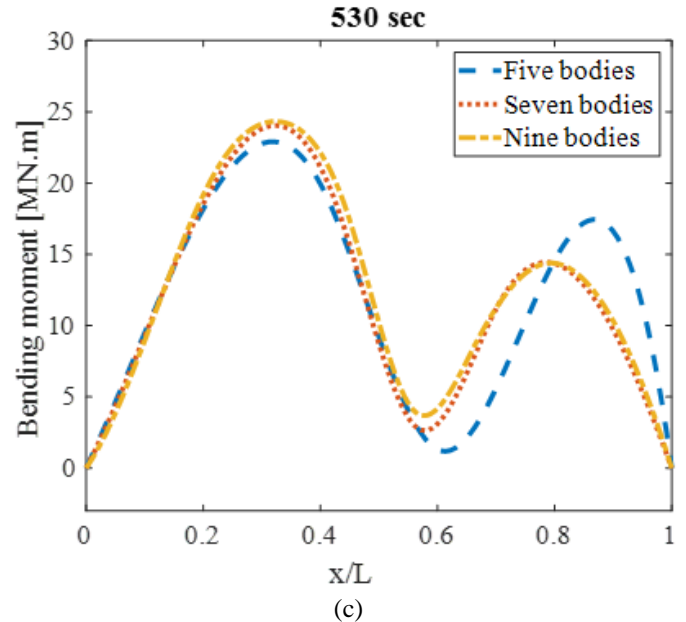
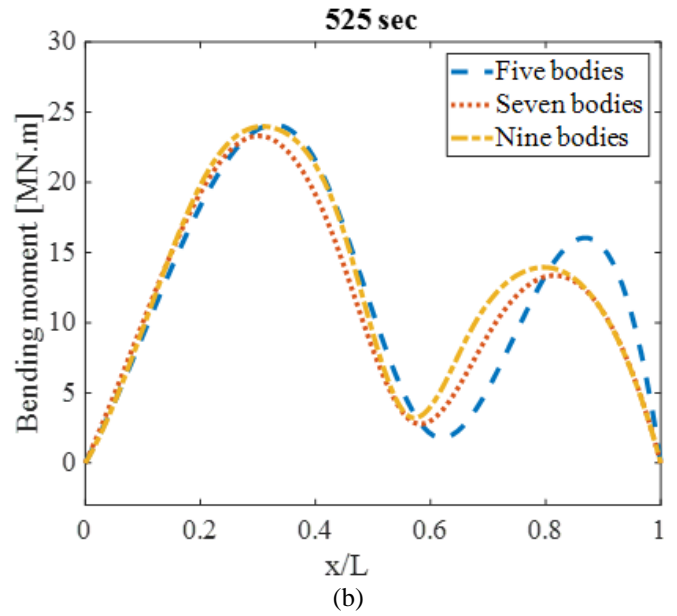
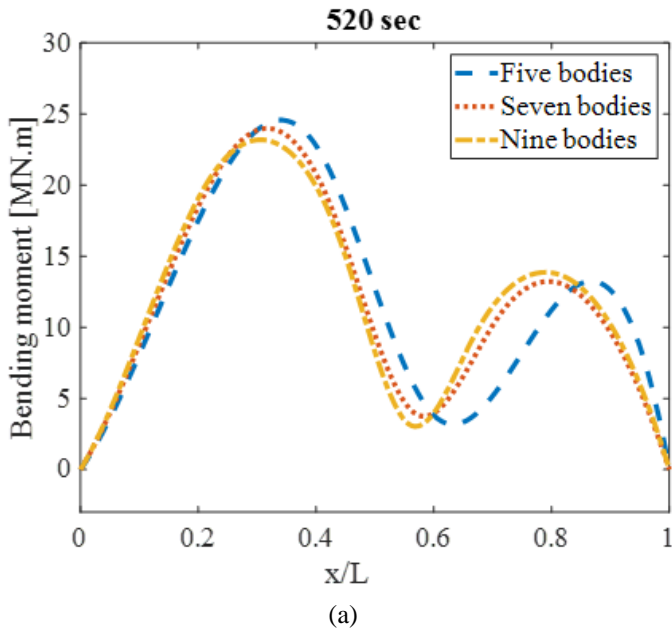


FIGURE 10: BENDING MOMENT RESPONSE AT (a) 520, (b) 525 AND (c) 530 SECS

As shown in FIGURE 10, the bending moment responses at the three different time instances agree well with the seven and nine-bodies model but not the five-bodies model. This can be because five bodies might not have sufficient points to capture all the encounter frequencies experienced by the SST.

Lu et al. [7] also showed and verified the accuracy of the proposed multi-body approach by comparing several test cases with the experimental results and found that the results shows quite a good agreement with each other. Therefore, the authors used seven bodies to present further results of the actual torpedo-shaped SST hull. It is obvious that to obtain more accurate results, the continuous SST should be divided into more

modules. However, wave-induced bending moment analysis does not require a large number of modules.

6.3. Controller Tuning for the Torpedo-shaped SST

The most optimal PID controller gains for the actual torpedo-shape seven bodies SST are presented in TABLE 5.

TABLE 5: MOST OPTIMAL PID GAINS FOR TORPEDO-SHAPE SEVEN BODIES SST

Gains	Seven bodies
K_P	-0.404
K_I	-0.0006820
K_D	-59.418

6.4. Time-Domain Responses and Power Spectral Density (PSDs)

The time-domain response and PSD distribution of the bending for the torpedo-shape seven bodies SST at different longitudinal locations are presented in FIGURE 11 & FIGURE 12, respectively. All the simulation studies are performed at 70 m water depth.

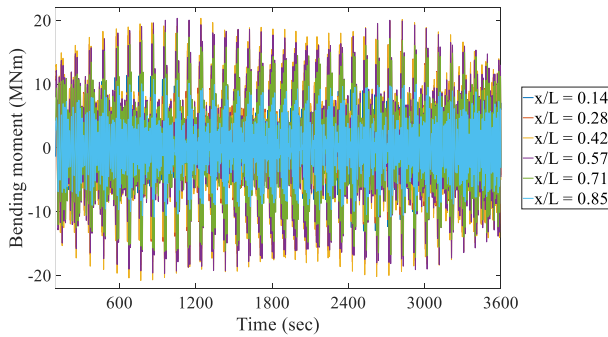


FIGURE 11: TIME SERIES PLOT (LC1 LOAD CASE)

The generalized time series response of bending moment at the different longitudinal locations is illustrated in FIGURE 11 for the LC1 load case. The static part of the bending moments responses is much smaller than the dynamic part, which is significant. This is because the bending moment effects on the SST hull are dominated by the pitch excitation moments that are characterized by large oscillations but small mean values. The statistical summary, including the mean value and standard deviation (STD) value, for bending moment of different load cases is presented in TABLE 6. The bending moment at $x/L = 0$ and $x/L = 1$ is zero, as both ends of all multi-body SST structures are free.

TABLE 6: STATISTICAL SUMMARY FOR BENDING MOMENT FOR LC1, LC2 AND LC3 LOAD CASE

x/L	Mean value (kNm)	Mean value (kNm)	Mean value (kNm)	STD value (MNm)	STD value (MNm)	STD value (MNm)
	(LC1)	(LC2)	(LC3)	(LC1)	(LC2)	(LC3)
0.14	42.1	116.6	184.1	5.35	7.76	11.46

0.28	72.2	132.3	254.5	7.12	10.18	13.7
0.42	64.3	143.8	231.8	8.18	11.91	16.11
0.57	47.8	164.9	187.3	7.96	11.70	15.79
0.71	28.6	164.1	128.5	6.77	9.88	13.25
0.85	14.7	72.5	81.0	4.10	5.90	7.8

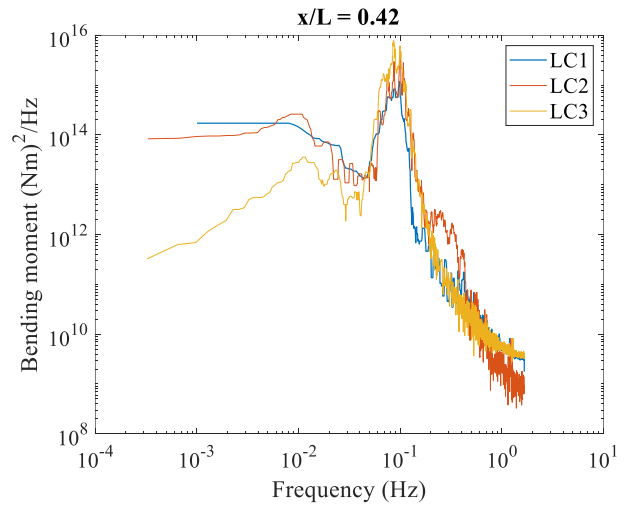
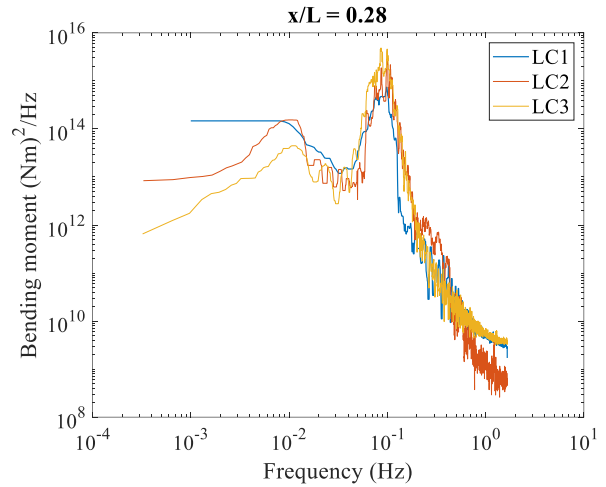


FIGURE 12: POWER SPECTRAL DENSITY

The PSDs distribution reveals the dynamic characteristics of the multi-body SST. The multi-body SST hull is mainly subjected to hydrodynamic forces and moments; therefore, the dominant excitation is from waves. For the dynamic bending moment response of the multi-body SST hull, the responses are mainly caused by low-frequency waves. Furthermore, a solid understanding of dynamic behavior is necessary to evaluate the extreme or design bending moment value and improve the design and analysis of the flexible hull of the SST.

6.5. Water Depth Effect

Furthermore, the wave effect is attenuated with water depth. According to the depth definition in Section 6, the operating depth range for the SST is between 40 m (safety depth) and 70

m (nominal diving depth). To better understand the wave effect on the SST hull, bending moment analysis at the 40 m water depth for the LC1 load case is performed. The statistical results are compared with those from 70 m water depth, as in TABLE 7. The mean bending moment at 40 m water depth is approximately 40% higher than at 70 m water depth. At both depths, there is not much variation in the standard deviation.

TABLE 7: STATISTICAL COMPARISON FOR BENDING MOMENT AT 40 M AND 70 M WATER DEPTH

Longitudinal distance	Mean value-40m depth (kN.m)	Mean value-70m depth (kN.m)	STD value-40m depth (MN.m)	STD value-70m depth (MN.m)
$x/L = 0.14$	58.41	42.1	6.09	5.35
$x/L = 0.28$	111.23	72.2	8.39	7.12
$x/L = 0.42$	117.37	64.3	8.21	8.18
$x/L = 0.57$	70.76	47.8	7.25	7.96
$x/L = 0.71$	28.03	28.6	6.84	6.77
$x/L = 0.85$	25.29	14.7	5.00	4.10

7. CONCLUSION

This paper proposed a reliable and efficient multi-body approach to investigate the bending moment response of the SST using the time-domain discrete-module-beam-bending based hydro-elastic technique.

First, a planar seakeeping model of the SST is developed based on a multi-body concept to study the bending moment response under the effect of waves. The total external forces, including radiation force, hydrostatic restoring force, and wave excitation force exerted on the CoG of each module, are calculated using multi-body hydrodynamic theory. A full-fledged convergence study has been carried out for three, five, seven, and nine bodies SST by defining the stiffness in the connection joints. The results show that the number of decomposed bodies influences the accuracy of the calculated results. The dynamic response and bending moment accuracy increase by increasing the number of bodies. The lower number of bodies (i.e., three and five) can provide good response in heave and pitch direction but may underestimate the bending moment response at a given time. This can be because three and five bodies SST may not have sufficient points to capture all the wave encounter frequencies, thereby giving the less accurate response.

It is important to note that this study's focus was on the multi-body concept rather than the way of subsequent bending moment assessment. However, a solid understanding of dynamic behavior is necessary to evaluate the extreme or design bending moment values and improve the design and analysis of the flexible hull of the SST.

Furthermore, the following research studies have been identified and planned by the authors:

- Extreme or design bending moment analysis of multi-body SST using state-of-the-art "Average Conditional Exceedance Rate (ACER) method".

- Efficient fatigue assessment of the SST hull.

REFERENCES

- [1] Norsk Petroleum, 2021, "The oil and gas pipeline system."
- [2] Ma, Y., Xing, Y., Ong, M. C., and Hemmingsen, T. H., 2021, "Baseline design of a subsea shuttle tanker system for liquid carbon dioxide transportation," *Ocean Engineering*, **240**, p. 109891. DOI: /10.1016/j.oceaneng.2021.109891.
- [3] Xing, Y., "A Conceptual Large Autonomous Subsea Freight-Glider for Liquid CO₂ Transportation" *Proc. ASME 2021 40th International Conference on Ocean, Offshore and Arctic Engineering*, p. V006T006A052. DOI: /10.1115/OMAE2021-61924.
- [4] Equinor Energy AS, 2019, "Subsea shuttle system," Research Disclosure, RD 662093.
- [5] Ellingsen, K. E., Ravndal, O., Reinas, R., Hansen, J. H., Marra, F., Myhre, E., Dupuy, P. M., and Sveberg, K., 2020, "Subsea Shuttle System," Research Disclosure, RD 677082.
- [6] Xing, Y., Ong, M. C., Hemmingsen, T., Ellingsen, K. E., and Reinås, L., 2021, "Design considerations of a subsea shuttle tanker system for liquid carbon dioxide transportation," *Journal of Offshore Mechanics and Arctic Engineering*, 143(4). DOI: /10.1115/1.4048926.
- [7] Lu, D., Fu, S., Zhang, X., Guo, F., and Gao, Y., 2019, "A method to estimate the hydroelastic behaviour of VLFS based on multi-rigid-body dynamics and beam bending," *Ships and Offshore Structures*, **14**(4), pp. 354-362. DOI: /10.1080/17445302.2016.1186332.
- [8] Betts, C. V., Bishop, R. E. D., and Price, W. G., 1977, "The symmetric generalized fluid forces applied to a ship in a seaway," *RINA Supplementary Papers*, **119**.
- [9] Bishop, R. E. D., and Price, W. G., 1997, "The generalized antisymmetric fluid forces applied to a ship in a seaway," *International Shipbuilding Progress*, **24**, pp. 3-14. DOI: /10.3233/ISP-1977-2426901.
- [10] Wu, Y., 1984, "Hydroelasticity of floating bodies," University of Brunel.
- [11] Liu, X., and Sakai, S., 2002, "Time domain analysis on the dynamic response of a flexible floating structure to waves," *Journal of engineering mechanics*, **128**(1), pp. 48-56. DOI: /10.1061/(ASCE)0733-9399(2002)128:1(48).
- [12] Phan, T. S., and Temarel, P., "Antisymmetric behaviour of pontoon and semi-submersible types of very large floating structure in regular oblique waves," *Proc. The Fourteenth International Offshore and Polar Engineering Conference, OnePetro*, pp. 04-085.
- [13] Hong, S. Y., Kim, J. H., Cho, S. K., Choi, Y. R., and Kim, Y. S., 2005, "Numerical and experimental study on hydrodynamic interaction of side-by-side moored multiple vessels," *Ocean Engineering*, **32**(7), pp. 783-801. DOI: /10.1016/j.oceaneng.2004.10.003.
- [14] Choi, Y. R., and Hong, S. Y., "An analysis of hydrodynamic interaction of floating multi-body using higher-order boundary element method," *Proc. The Twelfth International Offshore and Polar Engineering Conference, OnePetro*.

- [15] Yu, L., Li, R., and Shu, Z., "A Numerical and Experimental Study on Dynamic Responses of MOB Connectors," *Proc. The Fourteenth International Offshore and Polar Engineering Conference*, OnePetro, pp. 04-037.
- [16] Hong, S. Y., Choi, Y. R., and Hong, S. W., "Investigation of draft effects on analysis of hydroelastic responses of pontoon-type VLFS," *Proc. The Eleventh International Offshore and Polar Engineering Conference*, OnePetro, pp. 01-036.
- [17] Humamoto, T., and Fujita, K., "Wet-mode superposition for evaluating the hydroelastic response of floating structures with arbitrary shape," *Proc. The twelfth international offshore and polar engineering conference*, OnePetro, pp. 02-044.
- [18] Kashiwagi, M., "A mode-expansion method for predicting hydroelastic behavior of a shallow-draft VLFS," *Proc. Proceedings of the 16th International Conference on OMAE*, pp. 179-186.
- [19] Hong, S. Y., Kim, J. W., Shin, Y. S., and Ertekin, R. C., "An eigenfunction-expansion method for hydroelastic analysis of a floating runway," *Proc. The Thirteenth International Offshore and Polar Engineering Conference*, OnePetro, pp. 03-019.
- [20] Kim, J. W., "An eigenfunction expansion method for predicting hydroelastic behavior of a shallow-draft VLFS," *Proc. Proceeding of the 2nd International Conference on Hydroelasticity in Marine Technology, Fukuoka, 1998*, pp. 47-59.
- [21] Sim, I. H., "An analysis of the hydroelastic behaviour of large floating structures in oblique waves," *Proc. Proceedings of the 2nd International Conference on Hydroelasticity in Marine Technology*, pp. 195-200.
- [22] Yasuzawa, Y., Kagawa, K., Kawano, D., and Kitabayashi, K., "Dynamic response of a large flexible floating structure in regular waves," *Proc. Proceedings of the 1997 16th International Conference on Offshore Mechanics and Arctic Engineering. Part 1-B (of 6)*, ASME, pp. 187-194.
- [23] Kim, B. W., Hong, S. Y., Kyoung, J. H., and Cho, S. K., 2007, "Evaluation of bending moments and shear forces at unit connections of very large floating structures using hydroelastic and rigid body analyses," *Ocean engineering*, **34**(11-12), pp. 1668-1679. DOI: /10.1016/j.oceaneng.2006.10.018.
- [24] Cummins, W., Iuuhl, W., and Uinm, A., 1962, "The impulse response function and ship motions."
- [25] Newman, J. N., 2018, *Marine hydrodynamics*, The MIT press.
- [26] Faltinsen, O., 1993, *Sea loads on ships and offshore structures*, Cambridge university press.
- [27] Ogilvie, T. F., "Recent progress toward the understanding and prediction of ship motions," *Proc. 5th ONR Symp. on Naval Hydrodynamics*.
- [28] Taghipour, R., Perez, T., and Moan, T., 2008, "Hybrid frequency-time domain models for dynamic response analysis of marine structures," *Ocean Engineering*, **35**(7), pp. 685-705. DOI: /10.1016/j.oceaneng.2007.11.002.
- [29] Bowers, A. H., Murillo, O. J., Jensen, R. R., Eslinger, B., and Gelzer, C., 2016, "On wings of the minimum induced drag: Spanload implications for aircraft and birds."
- [30] Schjøllberg, I., and Utne, I. B., 2015, "Towards autonomy in ROV operations," *IFAC-PapersOnLine*, **48**(2), pp. 183-188. DOI: /10.1016/j.ifacol.2015.06.030.
- [31] Åström, K. J., Häggglund, T., and Astrom, K. J., 2006, *Advanced PID control*, ISA-The Instrumentation, Systems, and Automation Society Research Triangle Park.

Lower bound buckling capacity prediction for the isotropic cylindrical shell under axial compression loading using a probabilistic approach

Karan Sandipkumar Patel¹⁾, Yucong Ma^{1,*}, Yihan Xing¹⁾

1. Department of Mechanical and Structural Engineering and Materials Science, University of Stavanger, Stavanger, Norway

*Corresponding author: yucong.ma@uis.no

Abstract

Buckling loads of thin-walled cylindrical shells subjected to axial force vary substantially because of their extreme sensitivity to various imperfections. This paper proposes a probabilistic analysis approach to predict the lower-bound buckling loads for axially loaded cylindrical shells. First, Fourier series expansion is used to describe measured imperfection signatures. Next, the Monte Carlo simulation approach generates stochastic realizations of the imperfection. The finite element analysis determines the eigenvalue buckling for each realization of the surface imperfection. Last, the eigenvalue buckling loads with imperfection are fitted using state-of-the-art Gumbel distribution and the Average Conditional Exceedance Rate (ACER) function to predict the lower bound buckling capacity at the desired exceedance probability. The design methodology shows the evolution of design techniques for imperfection-sensitive shells from the early 1980s, and the results are validated with experimental data. The confidence interval obtained using the ACER method is higher than the Gumbel fitting method, meaning ACER will overpredict the buckling capacity. The results show that the lower-bound capacities of the chosen cylindrical shells are slightly higher than the experimental results and compared with widely used design-by-rules criteria like NASA SP-8007, ASME BPVC VIII-2 and DNV.

Keywords

Buckling, imperfections, cylindrical shells, Gumbel distribution, ACER, Monte Carlo simulation, knockdown factor

1. Introduction

Reducing structural weight is a key design driver for developing future-generation submarines and aerospace vehicles which are economically feasible. Reducing the wall thickness would be an obvious choice for the designers to reduce manufacturing and operational expenditure costs for the cylindrical shell case.

Thin-walled cylindrical structures are used in various engineering applications, including offshore, marine and pipeline structures, civil engineering, and aeronautical vehicles. The failure due to buckling is the critical failure factor since these structures are typically subjected to significant axial compression loads [1-5]. Due to this axial compression loading, there is a large deformation on the surface of the shell. This deformation is perpendicular to the loading direction. The buckling phenomenon is followed by considerably reducing the shell's load-bearing capacity [4].

The maximum buckling load-bearing capacity N_{per} of the thin-walled cylindrical shells subjected to the axial compression load is given by Eq. (1) [6]

$$N_{per} = \frac{2\pi Et^2}{\sqrt{3(1-\nu^2)}} \quad (1)$$

where E is the modulus of elasticity, t is the wall thickness, and ν is the Poisson's coefficient. From the Eq. (1) it should be noted that the buckling load-bearing capacity is independent of the length L and radius R of the cylindrical shell.

When considering plastic buckling, the maximum theoretical buckling load-bearing capacity (squash load) is linked to the yield strength Y and can be calculated using Eq. (2) [6]

$$N_{squash} = 2\pi ERtY \quad (2)$$

The buckling capacity of the cylindrical shells reduces greatly without thick walls and/or stiffeners structure. The load-carrying capacity of the cylindrical shell is susceptible to various imperfections. Around the beginning of the 20th century, an extensive amount of experiments were carried out on cylindrical shells to understand Buckling under axial compression. Based on the outcomes of the experiments, the Lower Bound Design Philosophy has provided shell designers with a valuable tool for effective shell design [7]. When calculating the load-carrying capacities of a thin-walled cylindrical shell structure, lower bound design philosophy becomes the highly conservative deterministic technique [8, 9]. The uncertainties are compensated by employing an empirical knockdown factor (KDF). The experimental lower-bound buckling capacity is determined by multiplying KDF with a perfect shell buckling load [7]. In the 1960s, NASA SP-8007 [10] offered a practical design guideline to provide recommended lower-bound KDFs for cylindrical shells, as indicated in Eq. (3).

$$\lambda_{exp} = \frac{N_{exp}}{N_{per}} = 1 - 0.902 \times \left(1 - e^{-\frac{\sqrt{R/t}}{16}}\right) \quad (3)$$

Fig. 1 illustrates the plot of the knockdown factor versus the radius-to-thickness ratio (R/t) obtained from a large number of experiments [7].

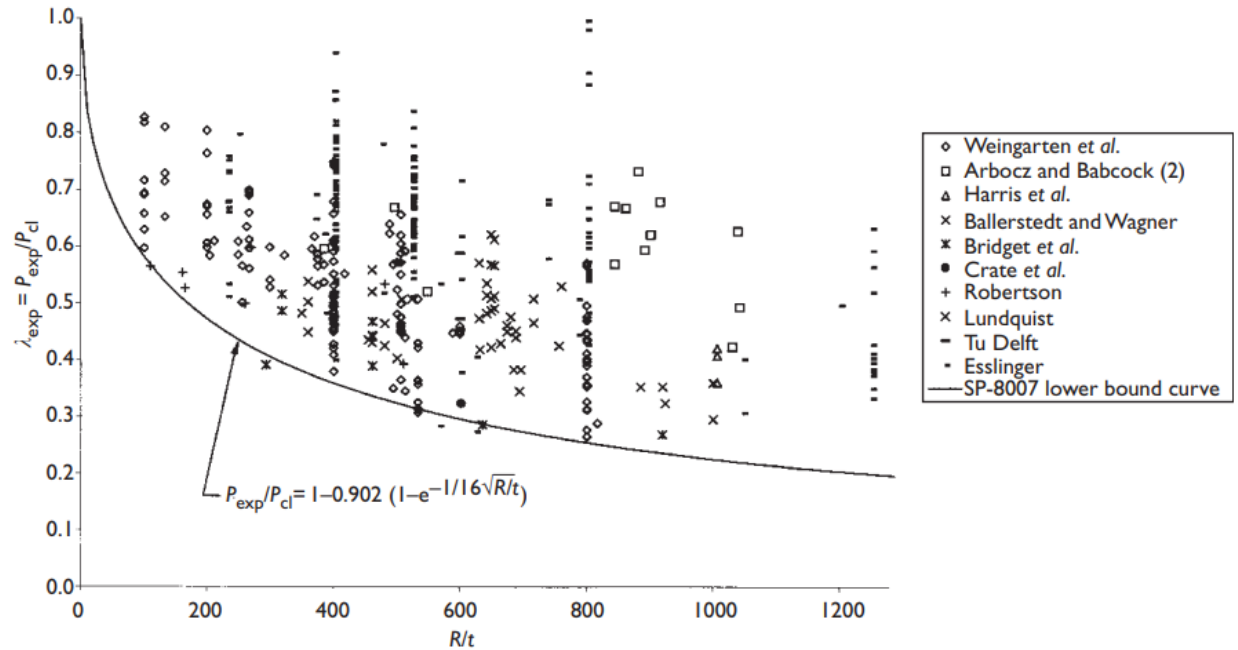


Fig. 1. Test data for isotropic shells subjected to axial compression [7]

Fig. 1 shows a considerable difference between buckling theory and related experimental evidence conducted at different places at different times. The KDFs are mostly between a range of 0.4 and 0.1 and, in a few cases, below the SP-8007 lower bound curve. Welds, material failure, plasticity, land failure, and poor boundary support all adequately impact the experimental results [11]. Despite great improvements in shell manufacturing and testing technique, the experimental result produced on cylindrical shell is 30% below the theoretical prediction [7]. Shape variations from the ideal cylindrical geometry termed geometric imperfections are a major cause of the huge disparity between buckling theory and experiment [12, 13]. The geometric imperfection was originally represented using buckling eigenmode expansion, and the resulting amplitudes were treated as a random variable [14].

Several numerical approaches have been developed to forecast lower-bound buckling loads due to imperfections properly. Schmidt and Winterstetter [15] categorized numerical modelling of imperfect shell structures into three approaches: "realistic," "worst," and "stimulating" imperfections. Huhne et al. [16] proposed one of the popular method called Single Perturbation Load Approach (SPLA) to predict the lower-bound buckling load due to imperfection. The dimple

produced by SPLA is regarded as a "worst" and "stimulating" imperfection, intensifying the pop-in of the initial defect [16-18]. Various limitations of the SPLA method have been discovered as the research continues. Wagner [9] found that the latter approach does not always provide a conservative KDF for a isotropic metallic cylindrical shell with a axisymmetric or ring buckling pattern in the pre-buckling stage. Hao et al. [19] discovered that the SPLA cannot encapsulate the influence of full-field real defect just by considering single dimple-shape imperfection. Additionally, compared to SPLA, the Multiple Perturbation Load Approach (MPLA) suggested by Arbelo et al. [20] is an improved and promising method for forecasting lower-bound limits. In MPLA, many perturbation loads are introduced into cylinders instead of a single perturbation load and the effect is determined by considering three factors: the number of perturbation loads, their amplitude and their location. Mahidan and Ifayefunmi [21] studied the imperfection sensitivity of axially compressed conical shells by introducing multiple imperfections, such as single and multiple load indentation, eigenmode imperfection, uneven axial length imperfection and crack imperfection.

Arbocz [22] presented a more realistic technique for the cylindrical shell that uses an actual measured geometric imperfection. A double Fourier series in the latter approach characterizes the geometric defects, and Fourier coefficients are the random variables of the probabilistic analysis. Double Fourier Series, as demonstrated by Arbocz and Abramovich [23], are ideally adapted to express genuine geometric defects. According to Arbocz [24], the KDFs estimated using real geometric faults correlates well with experimental data. The circumferential phase shift representation [17], the spectral representation [25] and the multimode approach [26] are alternative methodologies for the actual geometric representation.

Various probabilistic methods are used to investigate the effect of traditional and non-traditional imperfections [27-30]. Bolotin [31] introduced probabilistic methods to study shell buckling because the imperfection can be represented as random due to its shape and amplitude. The random nature of geometric imperfection is amenable to specific probabilistic distributions, and the probability of buckling can be quantified using probabilistic approaches [32]. Broggi and Schueller [33] and Broggi et al. [34] thoroughly discuss the probabilistic analysis of composite shells with geometric imperfections. The Probabilistic Perturbation Load Approach (PPLA) is proposed by Meurer et al. [18], which is completely independent of expensive geometric imperfection

measures. The latter approach constructs the traditional defects by using random imperfections. To describe traditional stochastic imperfection, evolutionary power spectra were used in combination with the spectral representation approach [25]. Schillo et al. [28] generated several initial geometric imperfections and calculated the associated buckling load using the Monte Carlo simulation method. Elishakoff et al. [35] proposed the semi-analytical first-order second moment (FOSM) when they discovered that the Monte Carlo simulation method could be time-consuming. Kreigesmann et al. [36] combined the Mahalanobis transformation with FOSM to reduce the computation time further up to a great extent. Arbocz and Hilburger [37] proposed an alternative probabilistic approach where only two imperfection modes represent geometric imperfection, and the associated amplitudes are characterized as the mean root square of the geometric imperfection signature. The geometric imperfection is not the only cause of reduction of buckling load [38], but also the irregular shell thickness [39] and deviation of the ideal loading positioning [40, 41].

Due to the advancement of technology, the effect of actual measured geometric imperfection on the buckling capacity of the cylindrical shell can be investigated extremely accurately [42, 43]. First, the structure must be built to study the effect of measured geometric imperfection. Later, the imperfections are quantified using optical measurement techniques [44], making the process time-consuming and expensive.

Lower-bound approaches should give the threshold for the buckling load equivalent to the buckling load capacity due to imperfections [45, 46]. Compared to probabilistic approaches, lower-bound methods eliminate the requirement for stochastic analysis, measurement and storage of imperfection data from several tests, saving time and money throughout the design process.

In addition to these model-based techniques, the regression analysis capacity of the artificial neural network (ANN) is used to predict the lower-bound buckling load capacity by utilizing supervised learning algorithms [47-49]. Waszczyszyn et al. [50] predict the buckling load capacity of the cylindrical shell under axial compression using the ANN approach. Furthermore, Zhang et al. [51] established Back-Propagation Neural Network (BPNN) to present measured imperfection patterns.

In addition to summarizing recent advancements in shell buckling analysis, this paper aims to propose a design example to determine the lower bound buckling capacity at the desired failure

probability value for isotropic cylindrical shells under axial compression load. The methodology used in this study leverages the Fourier series, where the Fourier coefficients are the stochastic variables gathered from the test data, to characterize the imperfect surfaces. The eigenvalue buckling for each cylindrical shell is computed using finite element analysis by generating random realizations of the geometric imperfections. Monte Carlo simulation generates random realizations of the imperfection using the data obtained from measurements. The buckling loads with imperfection are fitted using state-of-the-art Gumbel distribution and Average Conditional Exceedance Rate (ACER) function to predict the extreme values, i.e., the lower bound buckling capacity at the desired exceedance probability. The performance of the Gumbel distribution and ACER method is compared to predict the lower bound buckling value at the desired failure probability. The performance of the proposed approach is compared with NASA SP-8007 and other design-by-rule methods. Lastly, the conclusions and future work from this paper are presented.

2. Methodology

The use of a probabilistic-based technique in this paper has the benefit of dealing with problems involving traditional imperfection variables up to a great extent. As a result, the prediction for the lower bound buckling value at the desired probability of exceedance can be fully addressed. Fig. 2 is a schematic representation of the proposed approach, and the step-by-step guidance for applying the numerical procedure to obtain the lower bound value is given below

1. First, the imperfection Fourier coefficient is determined. This is done with the help of the actual measured data from the imperfection data bank.
2. Generation of the geometric imperfection for each cylindrical shell using the Fourier series. Then the random realization of surface imperfection are created using Monte Carlo simulation.
3. The finite element (FE) models of the cylindrical shells are generated for each surface imperfection set through the Monte Carlo simulation method.

4. Based on the imperfect shells, the FE mesh is generated, and the FE model is solved for eigenvalue buckling load in accordance with the applied loads and boundary conditions.
5. The procedure is repeated several times to obtain several eigenvalue buckling capacities for newly generated surface imperfection.
6. The values are fitted to a Gumbel distribution and ACER function. The associated lower-bound buckling load capacity is determined based on the failure probability chosen, and the performance of the Gumbel and ACER method is compared.

The following sections will describe these steps in great detail.

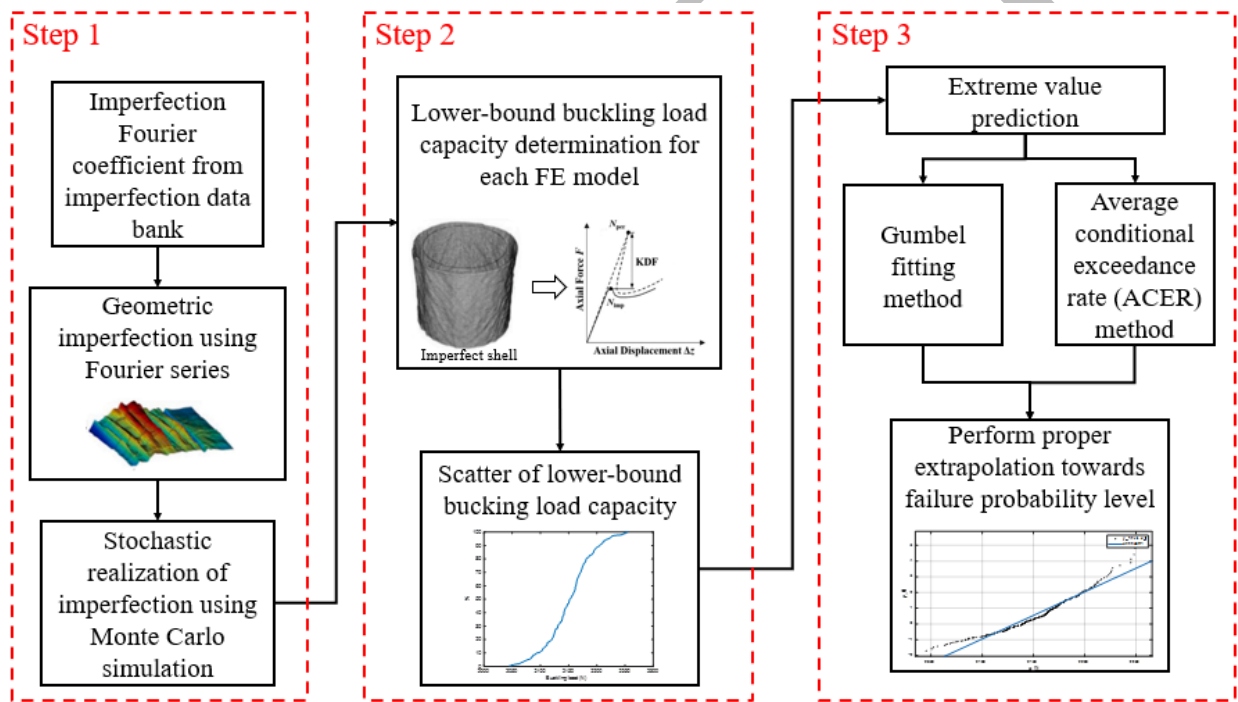


Fig. 2. Schematic overview of the probabilistic lower-bound design approach

3. Fourier series

The surface imperfections used in this paper are generated based on the TU Delft experimental testing campaign. The test results are summarized in the imperfection data bank [23]. This section will primarily describe measured geometric imperfection using the Fourier series. The documents by Dancy [52] are recommended for more information on the testing and test evolution of the buckling experiments [53].

The Fourier coefficients A_{kl} , B_{kl} , C_{kl} and D_{kl} of the half-wave cosine and sine methodology associated with the measured geometric imperfection are given in the imperfection data bank [23]. The authors decided to use the Fourier coefficient of the A shell and saved them along with the corresponding Matlab script to generate the surface plots of the imperfections.

The half-wave cosine and sine methodology is represented by Eq. (4) and Eq. (5). The latter Eqs are used to define the imperfect surface $W(x, y)$ of the cylindrical shells.

$$W(x, y) = t \sum_{k=0}^{n_1} \sum_{l=0}^{n_2} \cos \left(k\pi \frac{x}{L} \right) \left(A_{kl} \cos \left(\frac{ly}{R} \right) + B_{kl} \sin \left(\frac{ly}{R} \right) \right) \quad (4)$$

$$W(x, y) = t \sum_{k=0}^{n_1} \sum_{l=0}^{n_2} \sin \left(k\pi \frac{x}{L} \right) \left(C_{kl} \cos \left(\frac{ly}{R} \right) + D_{kl} \sin \left(\frac{ly}{R} \right) \right) \quad (5)$$

where L is the length of the cylinder, R is the radius of the cylinder, t is the wall thickness, l , k are the wave numbers, and x , y are the coordinates. The maximum number of waves included in the series is represented by n_1 and n_2 .

Fig. 3 illustrates the imperfection signature of the A-7 and A-12 shell and the numerical imperfection surface is compared with the one in the imperfection data bank [23]. The numerical results is very similar to the plots in the imperfection data bank. The imperfection signature given as a square sum (see, Eq. (6)) can be analyzed by plotting Fourier coefficients against the number of the axial and circumferential wave numbers l and k , see Fig. 4. Lower order modes dominate

the initial imperfection of the A-7 and B-1 shells as shown in Fig. 4. That is, as the circumferential wave number l increases, the amplitude of the Fourier coefficients based on the experimentally measured initial imperfection decay.

$$\xi = \sqrt{A_{kl}^2 + B_{kl}^2} \quad (6)$$

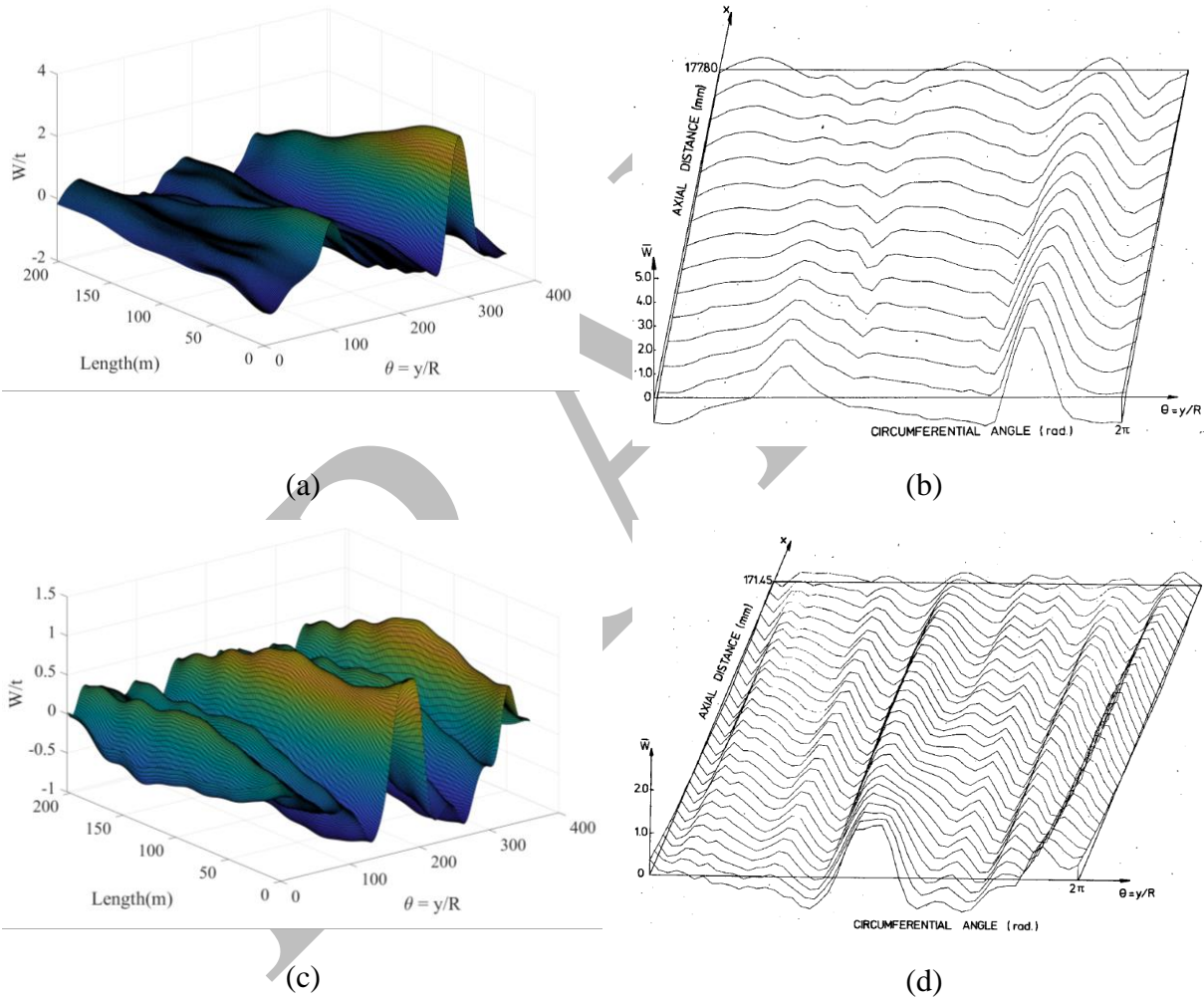


Fig. 3. Surface imperfection signature: A-7 shell - Simulated using Fourier series (a) and Imperfection data bank by Arbocz [23] (b); B-1 shell – Simulated using Fourier series (c) and Imperfection data bank by Arbocz [23] (d)

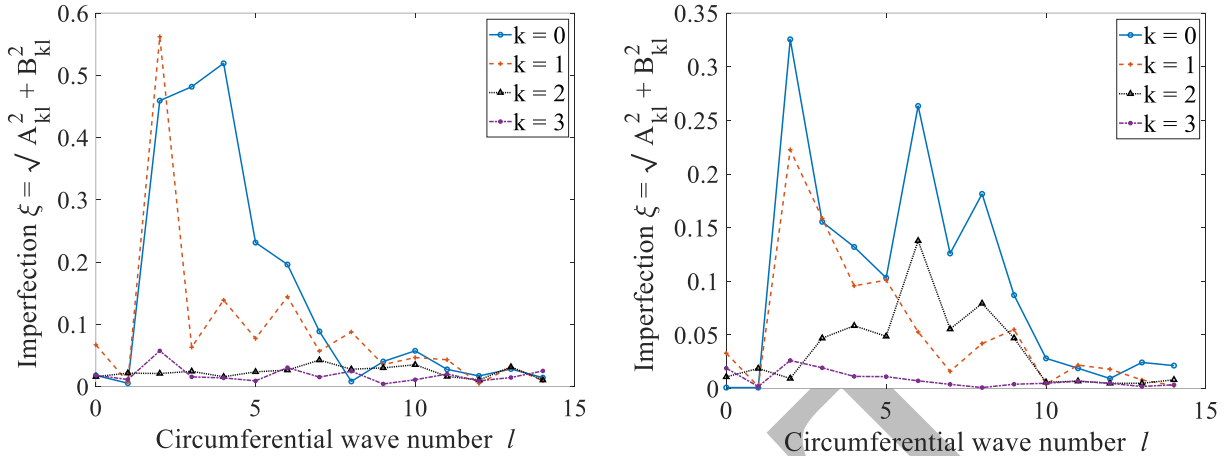


Fig. 4. Fourier coefficients against the number of the axial and circumferential wave numbers l and k for A-7 shell (left) and B-1 shell (right)

Initially, the coefficients are defined using an imperfection data bank [23], and then numerous stochastic realizations are determined using Monte Carlo simulation. This, in turn, produce many random realizations of the cylindrical shell structures.

4. Finite element (FE) modelling

However, introducing randomly generated geometric imperfection into each finite element (FE) model required a great computation time and effort to assess the lower-bound buckling capacity. Therefore, the authors have decided to use ANSYS Mechanical APDL 2020 R1 for the FE analysis since it allows batch processing by reading the '.inp file' input files and gives the results as '.csv' files. Matlab is used to read the output files for further post-processing.

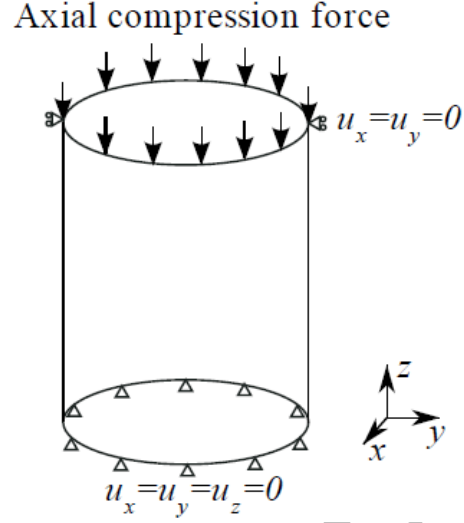


Fig. 5. Loading and boundary conditions on a different shell used in this paper

In this paper, two sets of material properties are used for the shell, see Table 1. Fig. 5 illustrates the boundary condition for the A-shell simulation. The bottom end is simply supported, i.e. translation moment of the nodes $u_x = u_y = u_z = 0$, while the rotational moments are set to be free. The top nodes are allowed to move in an axial direction, whereas the translation displacement u_x and u_y are fixed, i.e. $u_x = u_y = 0$. This ensures that the top edge remains straight during the collapse process. The boundary conditions used are the same as those used by Teng and Rotter [7], allowing the authors to compare the results. A total unit force is applied on the top nodes of the shell structure. Therefore, the compression force on each node can be calculated as follows:

$$p_A = \frac{1}{n_{top}} \quad (7)$$

where p_A is the axial compression load on each node at the top and n_{top} is total number of nodes at the top of the shell.

Table 1. Material properties of the cylindrical shells used in this study

Material properties	A-7 shell	B-1 shell
Young's modulus E [GPa]	104.11	106.5
Poisson ratio ν	0.3	0.3

A mesh size sensitivity study determines the best trade-off between result accuracy and computational cost. The results show that the 1-2 mm mesh size is adequate for the A-7 and B-1 shells. Fig. 6 illustrates the mesh size sensitivity study for the A-7 shell as a function of the lower-bound buckling load.

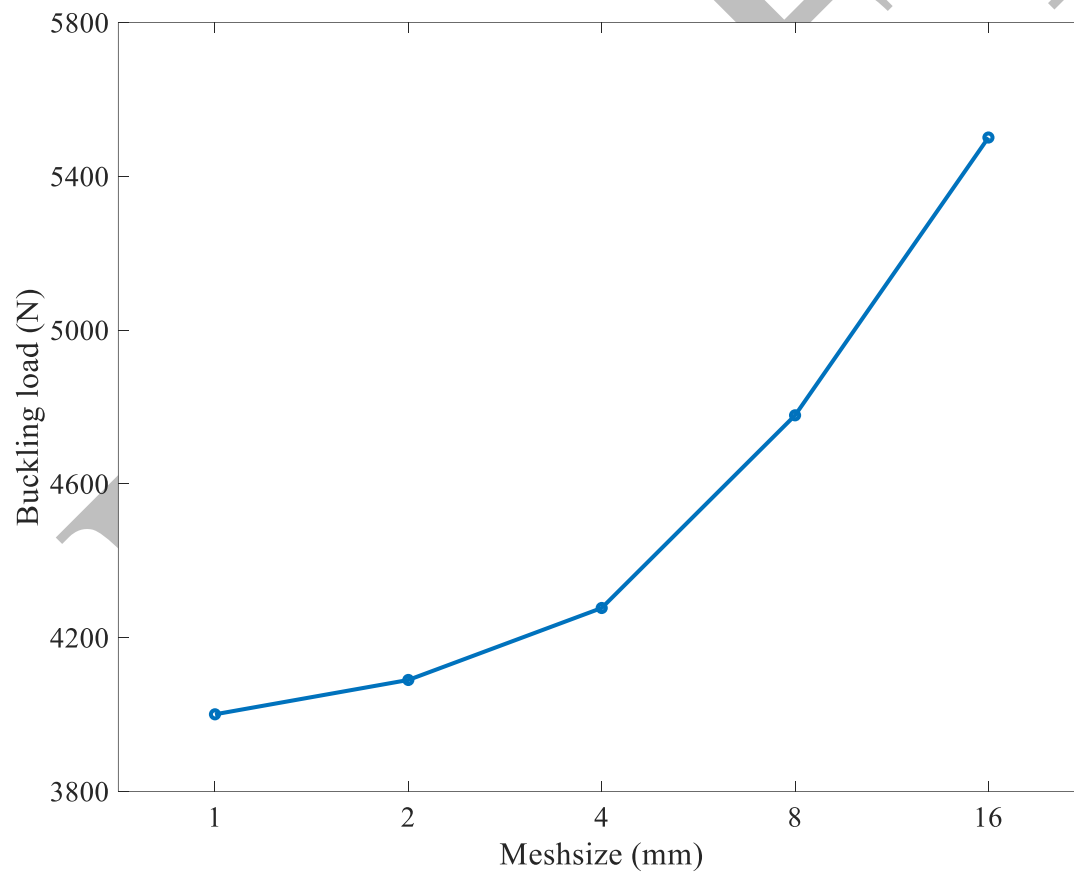


Fig. 6. Sensitivity study on mesh size on A-7 shell

5. Extreme value prediction

The extreme value is defined as the largest/smallest of the maximum/minimum value from the individual maximum/minimum values (i.e. the maximum/minimum from a series of discrete maxima/minima). The following equation presents the distribution of the smallest among n of a variable [54]:

$$Y_{ext} = \min(Y_{min1}, Y_{min2}, Y_{min3}, \dots, Y_{min n}) \quad (8)$$

where Y_{ext} is the smallest minimum value and $Y_{min i}$ is the individual minimum value. It is assumed that the individual minimum value $Y_{min i}$ are independent and identically distributed with cumulative distribution function (CDF) $F_{Y_{ext}}(y)$ [54]

$$F_{ext} = Prob(Y_{ext} \geq Y) = 1 - [1 - F_{Y_{min}}(y)]^n \quad (9)$$

Different methods are used to predict the extreme values at the desired exceedance probability. The state-of-the-art Gumbel fitting and Average Conditional Exceedance Rate (ACER) methods are the most well-proven. These methods have been successfully used to predict the marine and offshore structure's load effect analysis under the excitation of wind and wave loads. The authors want to utilize the two approaches mentioned above to predict the lower-bound buckling capacity at the desired failure probability.

5.1. Gumbel fitting method

Gumbel distribution is the most common type of extreme value distribution, also known as type I extreme value distribution.

The lower-bound buckling load capacity values obtained from various FE analyses are fitted to the extreme Gumbel distribution to determine the minimum lower-bound capacity for a given cylindrical shell at the desired exceedance probability. The generalized extreme value distribution

is represented by Eq. (10). It is the basis for evolving into various types of extreme value distributions.

$$F_x(x) = \exp \left\{ - \left(1 + \gamma \left(\frac{x - \mu}{\sigma} \right)^{\frac{-1}{\gamma}} \right) \right\} \quad (10)$$

where γ is the shape parameter, μ is the location parameter (shows the measure of location), σ is the scale parameter. When γ tends to 0, the distribution approximately fits the Gumbel distribution [55].

$$F_x(x) = \exp \left\{ - \exp \left\{ - \left(\frac{x - \mu}{\sigma} \right) \right\} \right\} \quad (11)$$

Eq. (11) can be written in logarithmic terms as given below:

$$-\ln \left(-\ln(F_x(x)) \right) = \frac{x}{\sigma} - \frac{\mu}{\sigma} \quad (12)$$

The Matlab inbuilt curve fitting tool is used to determine the location and scale parameter from the cumulative distribution probability (CDF) of the lower-bound buckling load data., i.e., a straight-line fitted by the original data on a probability paper.

5.2.Average Conditional Exceedance Rate (ACER) method

The Average Conditional Exceedance Rate (ACER) method, introduced by Naess and Gaidai [56], estimates the extreme value distribution by generating a sequence of non-parametric functions. The methodology applies to both stationary and non-stationary processes since it includes all global maxima peaks and the correlation between subsequent peaks in a sample series. Peak extraction is dependent on the type of data available. If the data comes from the narrow-banded

process, the peak data is extracted first, and only those data are used to analyze the conditional rates. On the other hand, if the data is already considered as the peak data (i.e., related to this work) or broad-band process, then extracting the peak is less significant.

Let $\{X_j: j = 1, 2, \dots, N\}$ be the realization of the lower-bound buckling values obtained through the Monte-Carlo simulation. n is the number of peak loads or the number of points contained in the data. This number is required when the target level is defined. The distribution function for the extreme values of the data can be written as

$$M_N = \min(X_1, X_2, X_3, \dots, X_N) \quad (13)$$

The extreme value distribution function or probability of occurrence (CDF) for the minimum values of the response η is established; see Eq. (14). It is assumed that X_N are independent and identically distributed with CDF function.

$$P(\eta) = \text{Prob}(X_j \geq \eta, X_1 \geq \eta, X_2 \geq \eta \dots \dots X_N \geq \eta) \quad (14)$$

The lower-bound buckling value realizations obtained from the FE analysis are not stationary data sets. The ACER method is applied to this non-stationary collection of data sets to assess the extreme values. The basic idea of this method is that a series of non-parametric functions based on ACER functions are established to represent the actual extreme value distribution, as shown in Eq. (8). The extreme value distribution using the ACER function can be written as [56]

$$P_k(\eta) = \exp(-(N - k + 1)\varepsilon_k(\eta)) \quad (15)$$

where ε_k is the empirical ACER function with the order k .

$$\varepsilon_k(\eta) = \frac{1}{N - k + 1} \sum_{j=k}^N a_{kj}(\eta) \quad (16)$$

The above equation can be assumed as an Ergodic process such that one single realization of the stochastic process is representative of the process. For each condition of the recorded value, ergodicity is used to estimate the short-term expected values by utilizing values of $a_{kj}(\eta)$ functions. Empirical probability distribution of $m = 1, \dots, M$ is an alternative method of depicting the long-term extreme value distribution in Eq. (15) at the given surface imperfection having probabilities p_m , such that $\sum_{m=1}^M p_m = 1$. This is followed by introducing the long-term ACER function of order k :

$$ACER_k(\eta) \equiv \sum_{m=1}^M \varepsilon_k(\eta, m) p_m \quad (17)$$

where $\varepsilon_k(\eta, m)$ is the same function as in Eq. (15), but it is limited to a specific realization with the number m . According to the long-term ACER function of order k , long-term extreme value distribution can be expressed as shown in [57-60]

$$p(\eta) \approx \exp(-N \cdot ACER_k(\eta)) \quad (18)$$

where $ACER_k$ is the long-term empirical ACER functions of order k , with $k \ll N$; N is the total number of data points used to estimate the ACER functions. Eq. (18) starts to become accurate as the order k of the ACER function increases [57-60]. The possibility of a data clustering effect can be noticed when we continue increasing the k level. Thus, the ACER method provides several advantages: 1) It improves the accuracy of extreme prediction associated with long return periods, and 2) it avoids the over-conservative design values in results.

An extrapolation approach is utilized to predict the extreme value distribution when η is very large. The tail of the ACER function is assumed as $\exp\{-(a\eta + b)^c + d\}$

$$\varepsilon \approx q \times \exp(-a(x - b)^c) \quad (19)$$

where a , b , c , and d are the constants that depend on the order k , and q fluctuates slowly in the tail area compared to the exponential function in Eq. (19). Therefore, it can be substituted by a suitable constant. The Levenberg Marquardt Least square technique can be used to calculate the constants a , b , c , and d . The ACER method, as demonstrated by Naess and Moan [59] and Chai et al. [61] gives quite accurate prediction for extreme values while saving substantial computing effort.

6. Case study

Table 2 lists all the cases that are investigated in this paper. The case study is based on Doup's A-7 and B-1 shell experiments. The goal of looking at Doup's A-7 and B-1 shells is to give a reference point for the probabilistic approach provided in this study. The main objective of this study is to compare the performance and efficiency of the suggested approach against the NASA SP-8007 and other design-by-rule methods utilized for sizing these pressure vessels. In this paper, the authors assumed that the cylinders are produced using a single seam weld at the 0° and 360° location. Furthermore, this may not be feasible for massive pressure vessels like submarines or space rockets, requiring more than one seam weld fabrication. The authors did not consider modelling multiple seam welds in this paper because the main objective of this research is to emphasize the efficiency of the suggested technique in decreasing safety factors. The authors will conduct future investigations with multiple seam welds to produce a more precise and realistic outcome for large-pressure vessels like submarines.

Table 2. Geometry data for the cylindrical shells

CASE NO.	GEOMETRY TYPE	DIMENSIONS			LOADING	NO. OF REALIZATIONS
		D (m)	L (m)	t (m)		
1	A-7 shell	0.2032	0.2032	1.14E-4	Axial force	200
2	B-1 shell	0.2032	0.1968	2.05E-4	Axial force	200

7. Results and discussions

The results and discussion corresponding to the abovementioned cases are presented in subsections 7.1 and 7.2.

7.1. Numerical results

Fig. 3 illustrates the original realization of the surface imperfection for the A-7 and B-1 shells. Fig. 7 represents the associated eigenvalue buckling shape for the imperfect surface. The surface imperfections discussed in this study are in the order of the wall thickness, i.e., the surface can deviate about ± 2 and 1 for A-7 and B-1 shells, respectively. On-site measurements can be used to calibrate the actual surface variation. Clearly, a greater variance in the imperfection will result in a lower computed eigenvalue buckling load. The eigenvalue buckling shape (see Fig. 7) lacks any well-defined deformation pattern. This means that the shape seems to be relatively localized. However, the eigenvalue buckling shapes will differ greatly from those observed for the perfect or ideal surface geometries. The eigenvalue buckling load of a perfect thin-wall cylinder is low for the first mode, which also represents global collapse mode. Furthermore, a significant factor of safety is associated with the calculated eigenvalue buckling for the perfect geometrical shells.

However, due to imperfections, this paper considers the first eigenvalue buckling shape as a local mode for the chosen shells. One advantage the proposed approach provides is that it tends to have a more significant eigenvalue buckling load. Therefore, the lower-bound buckling value can be predicted effectively with a lower safety factor since the actual imperfection is considered. The next section presents the lower bound buckling capacity at the desired exceedance probability to lower the safety factor further.

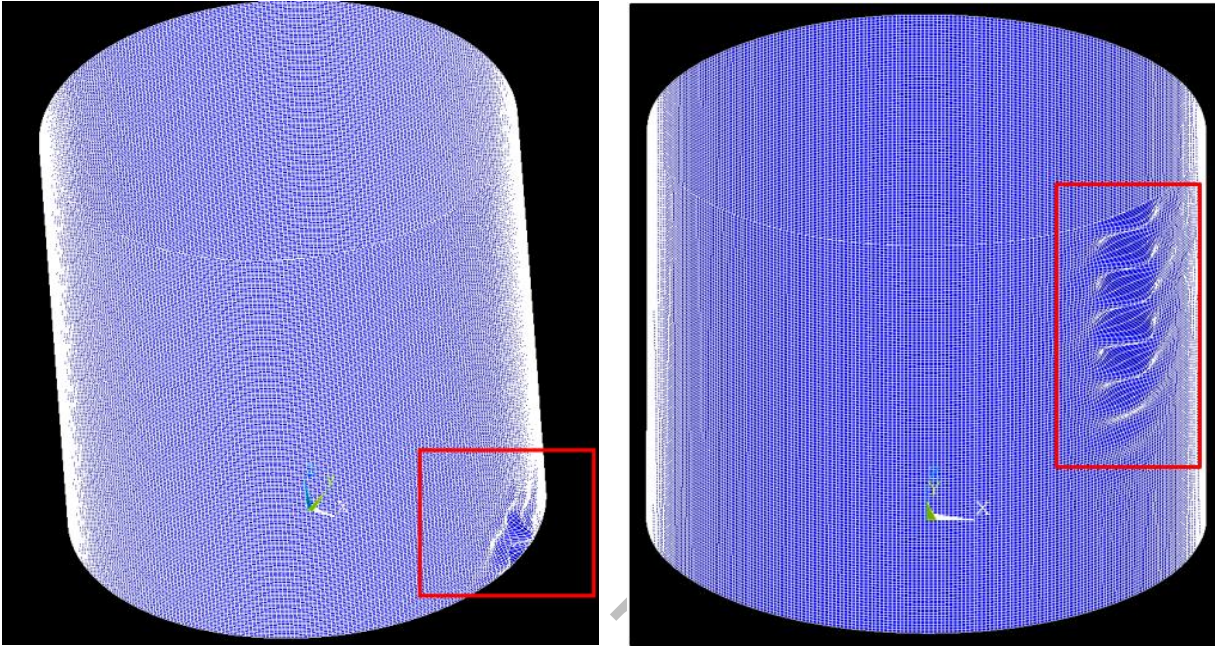
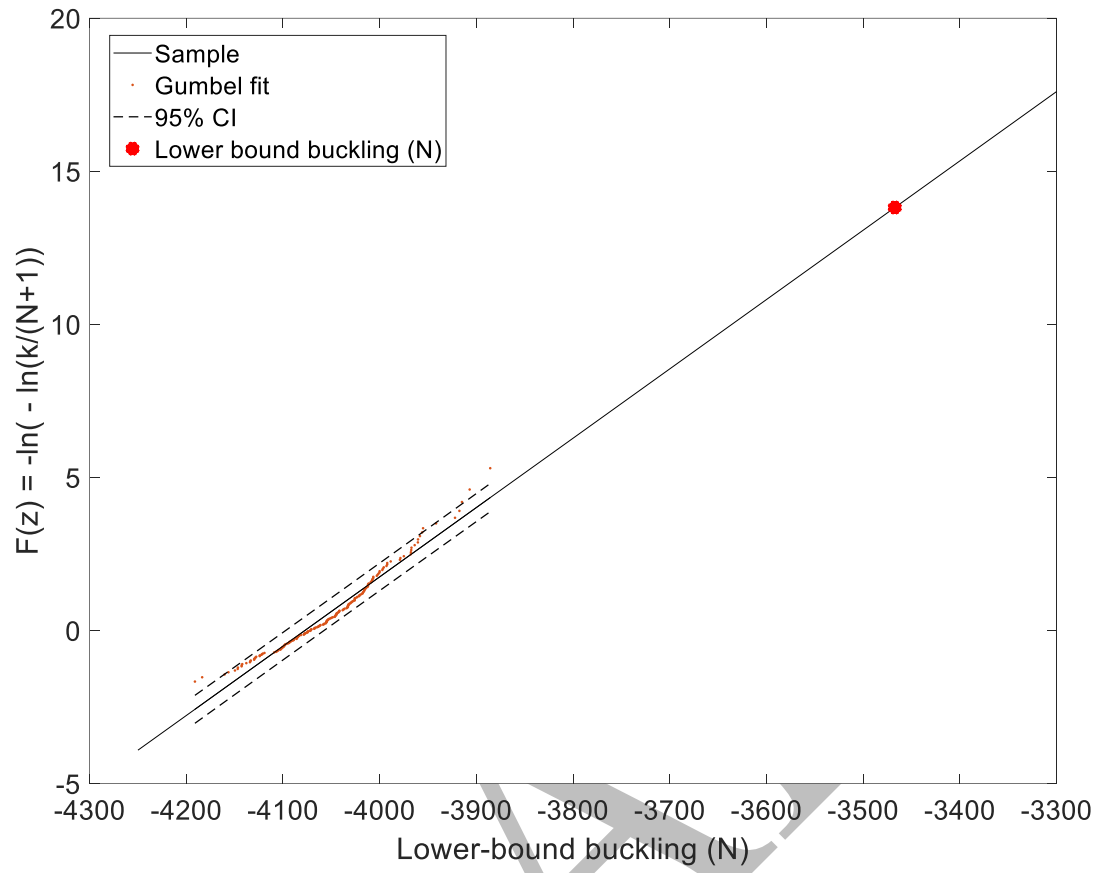


Fig. 7. Eigenvalue buckling shape associated with the surface imperfection (Fig. 3) for A-7 shell (left) and B-1 shell (right).

7.2. Gumbel fitting method vs ACER method

Fig. 8. illustrated the lower-bound buckling load capacities obtained using 200 different surface imperfections for the A-7 shell and B-1 shell fitted to a Gumbel distribution. The measured data shows an upward-curving trend which indicates the Gumbel distribution was not a good fit for random surface representation for A-7 and B-1 shells; the R^2 values are 0.9347 and 0.9195, respectively.



(a)

DRAFT

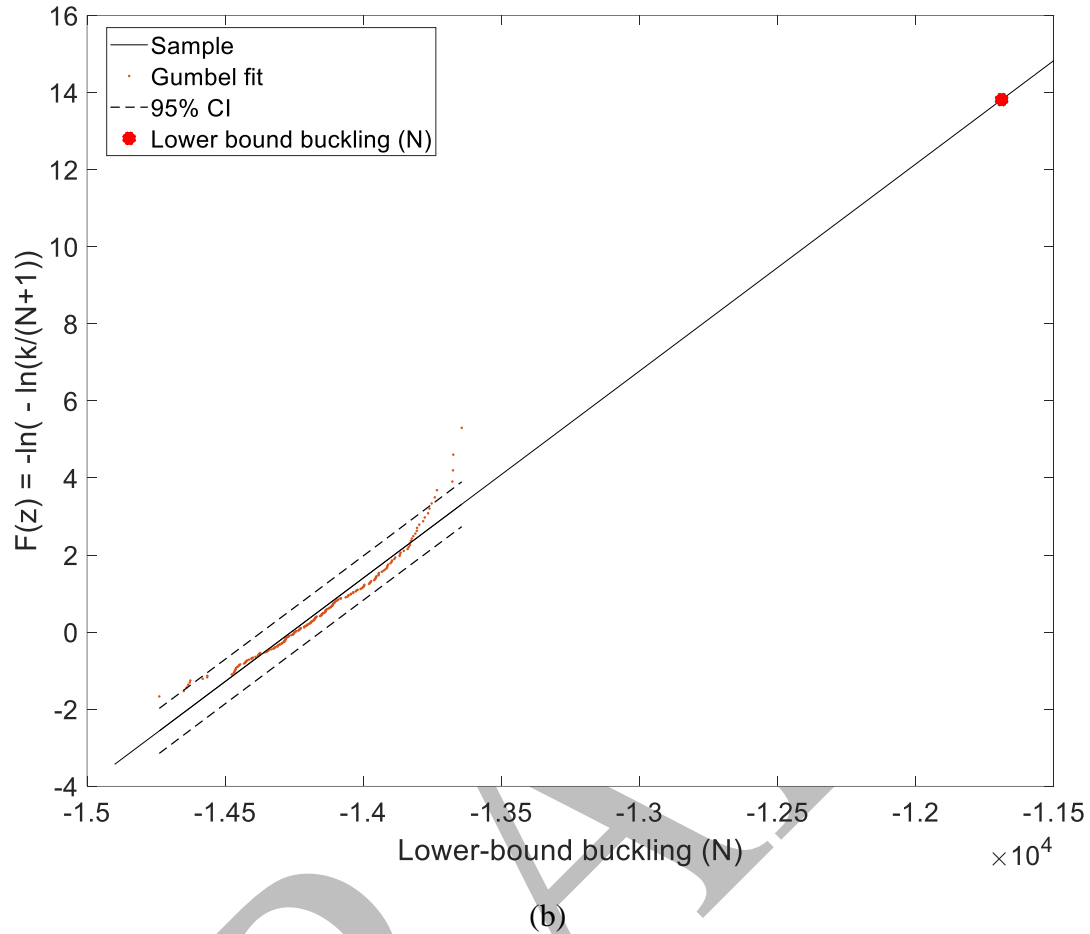
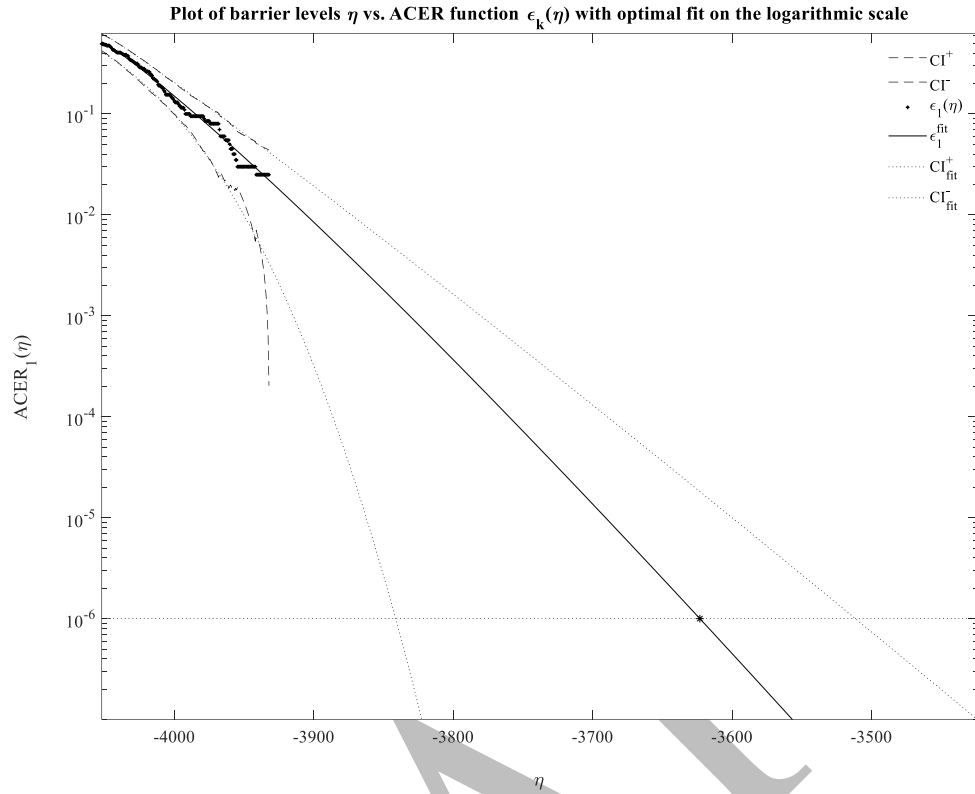
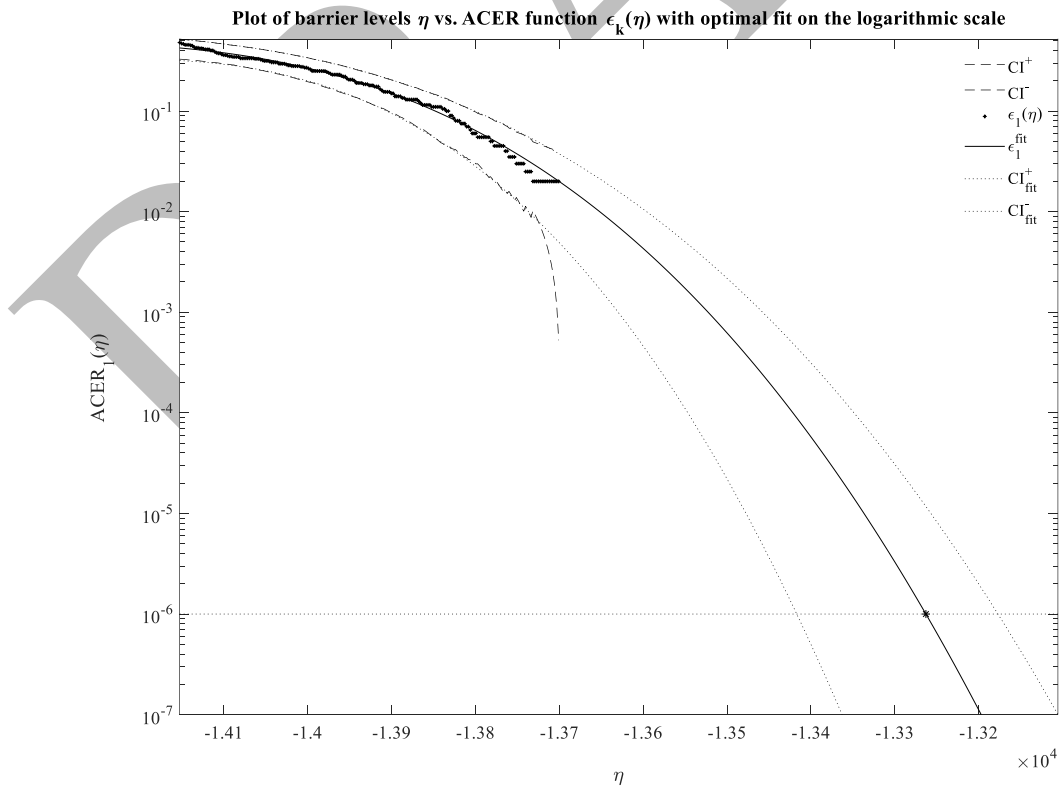


Fig. 8. Gumbel fitting for the A-7 shell (a) and B-1 shell (b) and the lower-bound buckling value (red dot) at the desired exceedance probability of 10^{-6}

The performance of the Gumbel fitting is tested by selecting another empirical fitting approach, such as the ACER method, see Fig. 9. It can be seen that the lower-bound value does not differ much as compared to the Gumbel fitting for the A-7 shell, but there is a significant difference for B-1 shell. To the author's surprise, the 95 % confidence interval obtained from the ACER method is wider than the 95 % confidence interval obtained from the Gumbel fitting method. The large interval size of ACER indicates that the lower-bound buckling value obtained through ACER is less accurate than the Gumbel distribution for the A-7 and B-1 shells. This means that ACER will overpredict the lower-bound buckling load. Future studies should look at selecting a more appropriate distribution.



(a)



(b)

Fig. 9. ACER fitting for the A-7 shell (a) and B-1 shell (b) and the lower-bound buckling value (red dot) at the desired exceedance probability of 10^{-6}

7.3.Lower-bound buckling capacities

The lower-bound buckling capacities are estimated using the Gumbel fitting and ACER methods at an exceedance probability of 10^{-6} . The numerical results are compared to Arbocz [23] and other designs by rule methods like ASME BPVC VIII-2 and DNV, see Table 3.

Table 3. Lower-bound buckling capacities using probabilistic method, Arbocz and other design by rules method.

Shells	Gumbel fitting method	ACER method	Arbocz [23]	ASME BPVC VIII-2	DNV
A-7 shell	3467.22 N	3623.14 N	3036.4 N	1062.1 N	975.92 N
B-1 shell	11689.42 N	13262.94 N	11326.0 N	4162.4 N	4098.0 N

The lower-bound buckling capacities for the A-7 shell calculated using the Gumbel fitting and ACER methods are 14.2% and 19.32% higher than the experimental value presented by Arbocz [23]. For the B-1 shell, the values for same are 3.20% and 17.10% higher than the experimental buckling load capacity [23]. Despite showing an upward curing trend, the Gumbel fitting approach provides better results than ACER. The difference in the experimental and numerical results can be due to the FE analysis conducted in more ideal conditions. But for experimental the boundary conditions and ambient conditions are not very ideal. The similar difference in experimental and numerical results is noticed in the work performed by Wagner et al. [30]. The proposed methodology demonstrates robustness in all analyzed scenarios while providing buckling design loads capacity exceeding the Arbocz [23], NASA SP-8007 and design-by-rules methods by reducing uncertainties, see Fig. 10 . It is observed that utilizing the current approach results in less conservative and more economical design loads than the design-by-rules methods. The significant increase in the buckling load capacity can be attributed to the use of a smaller, more specific sample set that better represents the local population. This leads to a more optimized lower-bound curve.

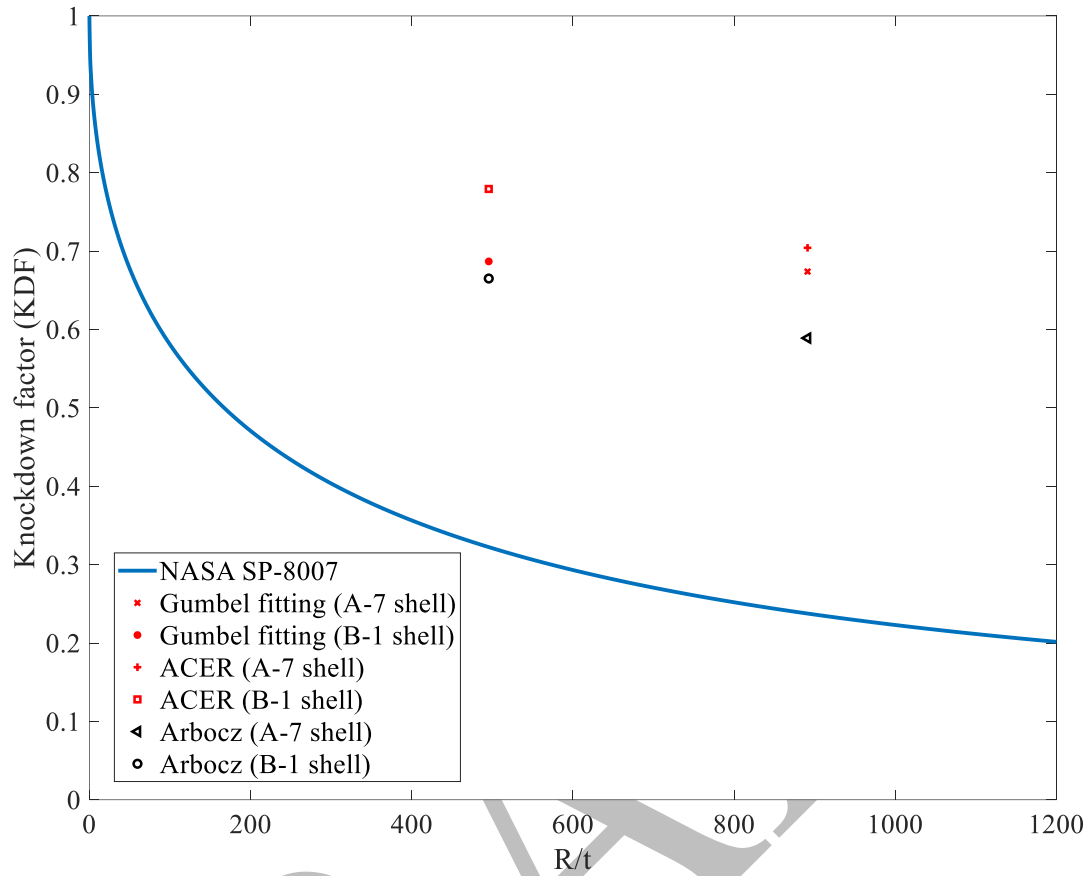


Fig. 10. Comparison of knockdown factor using different methods

8. Conclusion

This article proposes a probabilistic approach to predict the lower-bound buckling loads of thin wall cylinders subjected to axially compression loads. A probabilistic analysis with wall thickness surface imperfection was demonstrated using the Fourier series. The Fourier coefficients are the stochastic variables gathered from the imperfection data bank to characterize many realizations of the imperfect surfaces. This random realization of the imperfect surface is done using Monte Carlo Simulation. The eigenvalue buckling load for each imperfect cylindrical shell realization is computed using finite element analyses. The buckling loads with imperfection are fitted using state-of-the-art Gumbel distribution and Average Conditional Exceedance Rate (ACER) function to predict the extreme values, i.e., the lower bound buckling capacity at the desired exceedance probability. The following main conclusion is made from this article:

- 1) Gumbel fitting shows an upward trend indicating it was not an ideal fit for random surface representation for A-7 and B-1 shells. The 95 % confidence interval obtained from the ACER method is wider than the 95 % confidence interval obtained from the Gumbel fitting method indicating ACER is less accurate than the Gumbel distribution for the A-7 and B-1 shells. This means that ACER will overpredict the lower-bound buckling load.
- 2) The lower-bound buckling capacities for the A-7 shell calculated using the Gumbel fitting and ACER methods are 14.2% and 19.32% higher than the experimental value presented by Arbocz [23]. For the B-1 shell, the values for same are 3.20% and 17.10% higher than the experimental buckling load capacity [23]. The proposed methodology delivers always higher KDFs than the experimental value, NASA SP-8007, ASME BPVC VIII-2 and DNV. Hence, it can be regards as an improved method for predicting lower-bound buckling load capacity.

However, the Gumbel and ACER fitting methods do not accurately and precisely fit the values. Future studies should look at selecting a more appropriate distribution.

Reference

- [1] Chen, Z., Yang, L., Cao, G., and Guo, W., 2012, "Buckling of the axially compressed cylindrical shells with arbitrary axisymmetric thickness variation," *Thin-Walled Structures*, **60**, pp. 38-45. DOI: <https://doi.org/10.1016/j.tws.2012.07.015>
- [2] Fan, H., Chen, Z., Cheng, J., Huang, S., Feng, W., and Liu, L., 2016, "Analytical research on dynamic buckling of thin cylindrical shells with thickness variation under axial pressure," *Thin-Walled Structures*, **101**, pp. 213-221. DOI: <https://doi.org/10.1016/j.tws.2016.01.009>
- [3] Jiao, P., Chen, Z., Xu, F., Tang, X., and Su, W., 2018, "Effects of ringed stiffener on the buckling behavior of cylindrical shells with cutout under axial compression: Experimental and numerical investigation," *Thin-Walled Structures*, **123**, pp. 232-243. DOI: <https://doi.org/10.1016/j.tws.2017.11.013>
- [4] Wagner, H. N. R., Hühne, C., and Niemann, S., 2017, "Robust knockdown factors for the design of axially loaded cylindrical and conical composite shells – Development and Validation," *Composite Structures*, **173**, pp. 281-303. DOI: <https://doi.org/10.1016/j.compstruct.2017.02.031>
- [5] Wang, B., Zhu, S., Hao, P., Bi, X., Du, K., Chen, B., Ma, X., and Chao, Y. J., 2018, "Buckling of quasi-perfect cylindrical shell under axial compression: A combined experimental and numerical investigation," *International Journal of Solids and Structures*, **130-131**, pp. 232-247. DOI: <https://doi.org/10.1016/j.ijsolstr.2017.09.029>
- [6] Rotter, J., and Schmidt, H., "Stability of steel shells: European design recommendations," *Proc. European Convention for Constructional Steelwork, Brussels, Belgium*
- [7] Teng, J.-G., and Rotter, J. M., 2006, *Buckling of thin metal shells*, CRC Press.
- [8] Tian, K., Wang, B., Hao, P., and Waas, A. M., 2018, "A high-fidelity approximate model for determining lower-bound buckling loads for stiffened shells," *International Journal of Solids and Structures*, **148-149**, pp. 14-23. DOI: <https://doi.org/10.1016/j.ijsolstr.2017.10.034>
- [9] Wagner, H. N. R., Hühne, C., Niemann, S., and Khakimova, R., 2017, "Robust design criterion for axially loaded cylindrical shells - Simulation and Validation," *Thin-Walled Structures*, **115**, pp. 154-162. DOI: <https://doi.org/10.1016/j.tws.2016.12.017>
- [10] Peterson, J., 1968, *Buckling of thin-walled circular cylinders*, NASA.
- [11] Schmidt, H., 1989, "Dickwandige Kreiszylinderschalen aus Stahl unter Axialdruckbelastung," *Der Stahlbau*, **58(5)**, pp. 143-148
- [12] Hilburger, M. W., Nemeth, M. P., and Starnes Jr, J. H., 2006, "Shell buckling design criteria based on manufacturing imperfection signatures," *AIAA journal*, **44(3)**, pp. 654-663
- [13] Koiter, W. T., 1967, *On the stability of elastic equilibrium*, National Aeronautics and Space Administration.
- [14] Bolotin, V. V., "Statistical aspects in the theory of structural stability," *Proc. Proceedings of an International Conference Held at Northwestern University*, Pergamon, pp. 67-81. DOI: <https://doi.org/10.1016/B978-1-4831-9821-7.50009-0>
- [15] Winterstetter, T. A., and Schmidt, H., 2002, "Stability of circular cylindrical steel shells under combined loading," *Thin-Walled Structures*, **40(10)**, pp. 893-910. DOI: [https://doi.org/10.1016/S0263-8231\(02\)00006-X](https://doi.org/10.1016/S0263-8231(02)00006-X)
- [16] Hühne, C., Rolfes, R., Breitbach, E., and Teßmer, J., 2008, "Robust design of composite cylindrical shells under axial compression — Simulation and validation," *Thin-Walled Structures*, **46(7)**, pp. 947-962. DOI: <https://doi.org/10.1016/j.tws.2008.01.043>
- [17] Kriegesmann, B., Rolfes, R., Hühne, C., Teßmer, J., and Arbocz, J., "Probabilistic design of axially compressed composite cylinders with geometric and loading imperfections," *Proc.*

- International Journal of Structural Stability and Dynamics*, pp. 623-644. DOI: 10.1142/S0219455410003658
- [18] Meurer, A., Kriegesmann, B., Dannert, M., and Rolfes, R., 2016, "Probabilistic perturbation load approach for designing axially compressed cylindrical shells," *Thin-Walled Structures*, **107**, pp. 648-656. DOI: <https://doi.org/10.1016/j.tws.2016.07.021>
- [19] Hao, P., Wang, B., Du, K., Li, G., Tian, K., Sun, Y., and Ma, Y., 2016, "Imperfection-insensitive design of stiffened conical shells based on equivalent multiple perturbation load approach," *Composite Structures*, **136**, pp. 405-413. DOI: <https://doi.org/10.1016/j.compstruct.2015.10.022>
- [20] Arbelo, M. A., Castro, S. G., Kalnins, K., Ozolins, O., Khakimova, R., and Degenhardt, R., "Experimental characterization of buckling load on imperfect cylindrical shells using the multiple perturbation load approach," *Proc. Proceedings of the 13th European Conference on Spacecraft Structures, Materials and Environmental Testing*
- [21] Mahidan, F. M., and Ifayefunmi, O., 2021, "The imperfection sensitivity of axially compressed steel conical shells – Lower bound curve," *Thin-Walled Structures*, **159**, p. 107323. DOI: <https://doi.org/10.1016/j.tws.2020.107323>
- [22] Arbocz, J., "The imperfection data bank, a mean to obtain realistic buckling loads," *Proc. Buckling of Shells: Proceedings of a State-of-the-Art Colloquium, Universität Stuttgart, Germany, May 6–7, 1982*, Springer, pp. 535-567
- [23] Arbocz, J., and Abramovich, H., 1979, "The initial imperfection data bank at the Delft University of Technology: Part I," Delft University of Technology, Department of Aerospace Engineering, Report LR-290
- [24] Arbocz, J., and Babcock, C. D., "Prediction of Buckling Loads Based on Experimentally Measured Initial Imperfections," *Proc. Buckling of Structures*, Springer Berlin Heidelberg, pp. 291-311
- [25] Kepple, J., Herath, M. T., Pearce, G., Gangadhara Prusty, B., Thomson, R., and Degenhardt, R., 2015, "Stochastic analysis of imperfection sensitive unstiffened composite cylinders using realistic imperfection models," *Composite Structures*, **126**, pp. 159-173. DOI: <https://doi.org/10.1016/j.compstruct.2015.02.063>
- [26] Arbocz, J., and Starnes Jr, J. H., 2002, "Future directions and challenges in shell stability analysis," *Thin-Walled Structures*, **40**(9), pp. 729-754. DOI: [https://doi.org/10.1016/S0263-8231\(02\)00024-1](https://doi.org/10.1016/S0263-8231(02)00024-1)
- [27] Bisagni, C., and Alfano, M., "Probabilistic buckling analysis of sandwich composite cylindrical shells based on measured imperfections," *Proc. 58th AIAA/ASCE/AHS/ASC Structures, Structural Dynamics, and Materials Conference*, p. 0886
- [28] Schillo, C., Kriegesmann, B., and Krause, D., 2017, "Reliability based calibration of safety factors for unstiffened cylindrical composite shells," *Composite Structures*, **168**, pp. 798-812. DOI: <https://doi.org/10.1016/j.compstruct.2017.02.082>
- [29] Wagner, H. N. R., and Hühne, C., 2018, "Robust knockdown factors for the design of cylindrical shells under axial compression: potentials, practical application and reliability analysis," *International Journal of Mechanical Sciences*, **135**, pp. 410-430. DOI: <https://doi.org/10.1016/j.ijmecsci.2017.11.020>
- [30] Wagner, H. N. R., Hühne, C., and Elishakoff, I., 2020, "Probabilistic and deterministic lower-bound design benchmarks for cylindrical shells under axial compression," *Thin-Walled Structures*, **146**, p. 106451. DOI: <https://doi.org/10.1016/j.tws.2019.106451>

- [31] Bolotin, V., 1962, "Statistical methods in the nonlinear theory of elastic shells," *Izvestiya Akademii Nauk SSSR*, pp. 1-16
- [32] Elishakoff, I., 2012, "Probabilistic resolution of the twentieth century conundrum in elastic stability," *Thin-Walled Structures*, **59**, pp. 35-57. DOI: <https://doi.org/10.1016/j.tws.2012.04.002>
- [33] Broggi, M., and Schuëller, G. I., 2011, "Efficient modeling of imperfections for buckling analysis of composite cylindrical shells," *Engineering Structures*, **33**(5), pp. 1796-1806. DOI: <https://doi.org/10.1016/j.engstruct.2011.02.019>
- [34] Broggi, M., Calvi, A., and Schuëller, G. I., 2011, "Reliability assessment of axially compressed composite cylindrical shells with random imperfections," *International Journal of Structural Stability and Dynamics*, **11**(2), pp. 215-236. DOI: 10.1142/S0219455411004063
- [35] Elishakoff, I., Manen, S. v., Vermeulen, P. G., and Arbocz, J., 1987, "First-order second-moment analysis of the buckling of shells with random imperfections," *AIAA Journal*, **25**(8), pp. 1113-1117. DOI: 10.2514/3.9751
- [36] Kriegesmann, B., Möhle, M., and Rolfes, R., 2014, "Sample size dependent probabilistic design of axially compressed cylindrical shells," *Thin-Walled Structures*, **74**, pp. 222-231. DOI: <https://doi.org/10.1016/j.tws.2013.10.003>
- [37] Arbocz, J., and Hilburger, M. W., 2005, "Toward a Probabilistic Preliminary Design Criterion for Buckling Critical Composite Shells," *AIAA Journal*, **43**(8), pp. 1823-1827. DOI: 10.2514/1.11368
- [38] Hühne, C., Zimmermann, R., Rolfes, R., and Geier, B., "Sensitivities to geometrical and loading imperfections on buckling of composite cylindrical shells," *Proc. CD: Proceedings European Conference on Spacecraft Structures, Materials and Mechanical Testing, 11.-13. Dezember 2002, Toulouse*, pp. 1-12
- [39] Schillo, C., Röstermundt, D., and Krause, D., 2015, "Experimental and numerical study on the influence of imperfections on the buckling load of unstiffened CFRP shells," *Composite Structures*, **131**, pp. 128-138. DOI: <https://doi.org/10.1016/j.compstruct.2015.04.032>
- [40] Hühne, C., Zimmermann, R., Rolfes, R., and Geier, B., "Loading imperfections—experiments and Computations'," *Proc. Euromech colloquium*, pp. 2-5
- [41] Verduyn, W., and Elishakoff, I., 1982, "A testing machine for statistical analysis of small imperfect shells: Part I," Delft University of Technology, Department of Aerospace Engineering, Report LR-357
- [42] Hilburger, M. W., "On the development of shell buckling knockdown factors for stiffened metallic launch vehicle cylinders," *Proc. 2018 AIAA/ASCE/AHS/ASC structures, structural dynamics, and materials conference*, p. 1990
- [43] Wang, B., Du, K., Hao, P., Tian, K., Chao, Y. J., Jiang, L., Xu, S., and Zhang, X., 2019, "Experimental validation of cylindrical shells under axial compression for improved knockdown factors," *International Journal of Solids and Structures*, **164**, pp. 37-51. DOI: <https://doi.org/10.1016/j.ijsolstr.2019.01.001>
- [44] Schultz, M. R., Sleight, D. W., Gardner, N. W., Rudd, M. T., Hilburger, M. W., Palm, T., and Oldfield, N. J., "Test and analysis of a buckling-critical large-scale sandwich composite cylinder," *Proc. 2018 AIAA/ASCE/AHS/ASC Structures, Structural Dynamics, and Materials Conference*, p. 1693
- [45] Wagner, H. N. R., Hühne, C., and Niemann, S., 2018, "Robust knockdown factors for the design of spherical shells under external pressure: Development and validation," *International Journal of Mechanical Sciences*, **141**, pp. 58-77. DOI: <https://doi.org/10.1016/j.ijmecsci.2018.03.029>

- [46] Wagner, H. N. R., Hühne, C., Zhang, J., Tang, W., and Khakimova, R., 2019, "Geometric imperfection and lower-bound analysis of spherical shells under external pressure," *Thin-Walled Structures*, **143**, p. 106195. DOI: <https://doi.org/10.1016/j.tws.2019.106195>
- [47] Abambres, M., and Lantsoght, E., 2018, "Neural network-based formula for shear capacity prediction of one-way slabs under concentrated loads," *Neural network-based formula for shear capacity prediction of one-way slabs under concentrated loads*, pp. 1-33
- [48] Koide, R. M., Ferreira, A. P. C. S., and Luersen, M. A., 2015, "Laminated Composites Buckling Analysis Using Lamination Parameters, Neural Networks and Support Vector Regression," *Latin American Journal of Solids and Structures*, **12**
- [49] Tahir, Z. u. R., and Mandal, P., 2017, "Artificial neural network prediction of buckling load of thin cylindrical shells under axial compression," *Engineering Structures*, **152**, pp. 843-855. DOI: <https://doi.org/10.1016/j.engstruct.2017.09.016>
- [50] Waszczyszyn, Z., and Bartczak, M., 2002, "Neural prediction of buckling loads of cylindrical shells with geometrical imperfections," *International Journal of Non-Linear Mechanics*, **37**(4), pp. 763-775. DOI: [https://doi.org/10.1016/S0020-7462\(01\)00111-1](https://doi.org/10.1016/S0020-7462(01)00111-1)
- [51] Zhang, D., Chen, Z., Li, Y., Jiao, P., Ma, H., Ge, P., and Gu, Y., 2020, "Lower-bound axial buckling load prediction for isotropic cylindrical shells using probabilistic random perturbation load approach," *Thin-Walled Structures*, **155**, p. 106925. DOI: <https://doi.org/10.1016/j.tws.2020.106925>
- [52] Dancy, R., and Jacobs, D., 1988, "The initial imperfection data bank at the Delft University of Technology: Part II," Delft University of Technology, Faculty of Aerospace Engineering, Report LR-559
- [53] De Vries, J., "Research on the Yoshimura buckling pattern of small cylindrical thin walled shells," *Proc. Spacecraft Structures, Materials and Mechanical Testing 2005*
- [54] Haver, S., 2017, "Metocean modelling and prediction of extremes," Lecture notes in TMR4195-Design of Offshore Structures. Department of Marine Technology, Norwegian University of Science and Technology
- [55] Peeringa, J., 2009, Comparison of extreme load extrapolations using measured and calculated loads of a MW wind turbine, Petten: ECN.
- [56] Naess, A., and Gaidai, O., 2009, "Estimation of extreme values from sampled time series," *Structural Safety*, **31**(4), pp. 325-334. DOI: <https://doi.org/10.1016/j.strusafe.2008.06.021>
- [57] Naess, A., and Gaidai, O., 2008, "Monte Carlo Methods for Estimating the Extreme Response of Dynamical Systems," *Journal of Engineering Mechanics*, **134**(8), pp. 628-636. DOI: 10.1061/(ASCE)0733-9399(2008)134:8(628)
- [58] Naess, A., Gaidai, O., and Batsevych, O., 2010, "Prediction of Extreme Response Statistics of Narrow-Band Random Vibrations," *Journal of Engineering Mechanics*, **136**(3), pp. 290-298. DOI: 10.1061/(ASCE)0733-9399(2010)136:3(290)
- [59] Naess, A., and Moan, T., 2013, *Stochastic dynamics of marine structures*, Cambridge University Press.
- [60] Naess, A., Stansberg, C. T., Gaidai, O., and Baarholm, R. J., "Statistics of Extreme Events in Airgap Measurements," *Proc. ASME 2008 27th International Conference on Offshore Mechanics and Arctic Engineering*, pp. 733-742. DOI: 10.1115/omae2008-57754
- [61] Chai, W., Naess, A., Leira, B. J., and Bulian, G., 2016, "Efficient Monte Carlo simulation and Grim effective wave model for predicting the extreme response of a vessel rolling in random head seas," *Ocean Engineering*, **123**, pp. 191-203. DOI: <https://doi.org/10.1016/j.oceaneng.2016.07.025>